Development of absorbing materials for perovskite solar cells

Graduate School of Life Science

and System Engineering

Kyushu Insitute of Technology

Dissertation for the Degree of Doctor of Philosophy

Chunfeng Lan

February 2017

Supervisor

Professor Tingli Ma

Abstract

Recently, halide perovskite solar cells have attracted much attention due to their high power conversion efficiency (*PCE*) and low cost. Their efficiency has been sharply improved from 3.8% to 22.1% in the last six years, making them as the promising next generation solar cells. However, the halide perovskite solar cells are facing several serious problems, such as request of further improvement efficiency and the lead pollution. These problems hinder the future commercialization of halide perovskite solar cells. How to solve these problems is still a challenge. The efficiency of perovskite solar cells is strongly affected by the quality of perovskite films, such as the crystallization and coverage, while the lead pollution is attributed to the halide perovskite absorbing materials. Therefore, this thesis mainly focuses on the morphology control of $CH_3NH_3PbI_3$ to fabricate high-quality perovskite films with good crystallization and full coverage to improve the efficiency. We also design and synthesize new lead-free absorbing materials to avoid the lead pollution.

In Chapter 1, the background of solar energy and photovoltaic technologies has been introduced. Furthermore, the recent challenges for the halide perovskite solar cells and the purpose of this thesis have been described.

In Chapter 2, the experimental procedures, including general preparation and characterization of perovskite materials and electrodes, as well as devices used in this thesis have been summarized.

In Chapter 3, a new method of concentration gradient controlled growth has been developed to prepare high-quality $CH_3NH_3PbI_3$ perovskite films under ambient conditions. The two-step reactions were used with the concentration gradient of CH_3NH_3I (MAI) solutions, yielding the perovskite films with different crystallization and surface morphologies. In details, the first-step reaction between a low concentration MAI solution and the PbI_2 films resulted in the formation of large-scale perovskite grains, and in the second-step reaction with a high concentration MAI solution we achieved a full coverage of the perovskite films. The large grain sizes of ca. 1.5 μm in the $CH_3NH_3PbI_3$ perovskite films were obtained using the concentration gradient method, which means that the grain boundaries can be reduced. Meanwhile, spectral absorption in the short- wavelength region was enhanced in the concentration-gradient controlled perovskite films due to light scattering, which is considered to benefit the power conversion of solar cells. The

perovskite solar cells fabricated using the concentration gradient controlled method showed higher photovoltaic performance than that by the traditional single solution method.

In Chapter 4, the Pb-free composites of bismuth triiodide (BiI_3) and layered perovskite $(CH_3NH_3)_3Bi_2I_9$ (MBI) have been prepared by a simple solution method for thin film solar cells. It was found that the introduction of MBI significantly enhanced the crystallization and coverage of BiI_3, meanwhile there was a multi-absorption phenomenon in the composite films. In addition, the band bending occurred at the BiI_3-MBI interfaces, accompanying with the tuned energy levels in the composite films. The band bending was considered to benefit the efficient injection of excited electrons from absorbing layers into the electron transport layers. When 10-20% of MBI were used, the short circuit current density (J_{sc}) and open-circuit voltage (V_{oc}) were improved in the composite solar cells. An enhancement of 65% of the *PCE* was achieved in the $(BiI_3)_{0.8}(MBI)_{0.2}$ solar cells due to the multi-effects of the composite active layers.

In Chapter 5, the Pb-free double perovskites La_2NiMnO_6 have been studied for potential application on solar cells. The rhombohedral and the monoclinic La_2NiMnO_6 were respectively formed under different conditions. The monoclinic La_2NiMnO_6 had an experimental bandgap (E_g) of 1.4 eV and valence band (VB) of -5.8 eV. Whereas, the rhombohedral La_2NiMnO_6 had an experimental E_g of 1.2 eV and VB of -5.7 eV. Both of them are suitable as visible light absorbers. Furthermore, the density function theory calculation confirmed that the theoretical bandgap of the monoclinic La_2NiMnO_6 was larger than that of the rhombohedral La_2NiMnO_6, which was mainly attributed to the *B*-site distortion. Simultaneously, the top of the VB of La_2NiMnO_6 mainly come from the interaction of Ni 3*d* orbitals and O 2*p* orbitals, whereas the bottom of the conduction band primarily come from the hybridization between Mn 3*d* and O 2*p* orbitals. The results of experimental and theoretical studies indicated that the monoclinic double perovskite La_2NiMnO_6 is a better candidate as absorbing material than the rhombohedral La_2NiMnO_6 for solar cells.

Finally, general conclusions and future prospects have been presented. The investigations of Pb-based perovskites and Pb-free perovskites solar cells are still facing big challenges. The further studies including architectures designing of devices, recycling of Pb-based perovskites and development of new Pb-free perovskites with high performance are needed.

Contents

Chapter 1. Introduction

1.1 Solar energy

With the development of the world economy, the energy consumption of human activities in the world has been sharply increasing. Human collectively consumes the equivalent of a steady 13 trillion watts of power today, most of which are the fossil fuels. It is expected that the energy consumption will reach 30 trillion watts in 2050 [1-2]. Compared with other energy resources, the fossil fuels (including coal, natural gas, and petrol) do show many merits, such as a very high energy density and flexibility in transportation and storage capacity [2]. They have been widely used in in the past century. Nowadays the coal, gas and oil have matched 75% of the world energy demand [3].

The usage of fossil energy promoted the industrialization and did bring us lots of convenience. However, it also showed some serious side effects to human beings. One serious problem is the environmental pollution and ecological crisis, such as the acid rain, photochemical smog, PM2.5 pollution, global warming and climate change [4-6]. The huge consumption of fossil fuel emitted large amount of CO_2, toxic SO_2, NO_x and inorganic particles in the past decades. The over-emissions of the CO_2 and SO_2 *et al.* have not only changed the chemical content of the air, but also threaten the human health in the areas with a large population density. For example, in 1940s and 1950s Los Angeles in the United States once suffered from the photochemical smog and resulted in many deaths [5]. Nowadays Beijing of China in winter are suffering from the PM2.5 pollution due to the excess combustion of fossil fuels [4]. Another serious problem is that the fossil fuels are non-renewable and their reserves could not sustain such a continuous large consumption. As we know, the fossil coal, natural gas and petrol are produced when plant and animal matter decays within the earth-crust, and this process takes millions of years to form usable fuels. Therefore, fossil fuels are not renewable in the short term. As the increasing energy demand, the development of alternative clean energy resources, such as wind power, hydro-power, solar energy, biomass power and nuclear power, is very necessary to meet the future society [6].

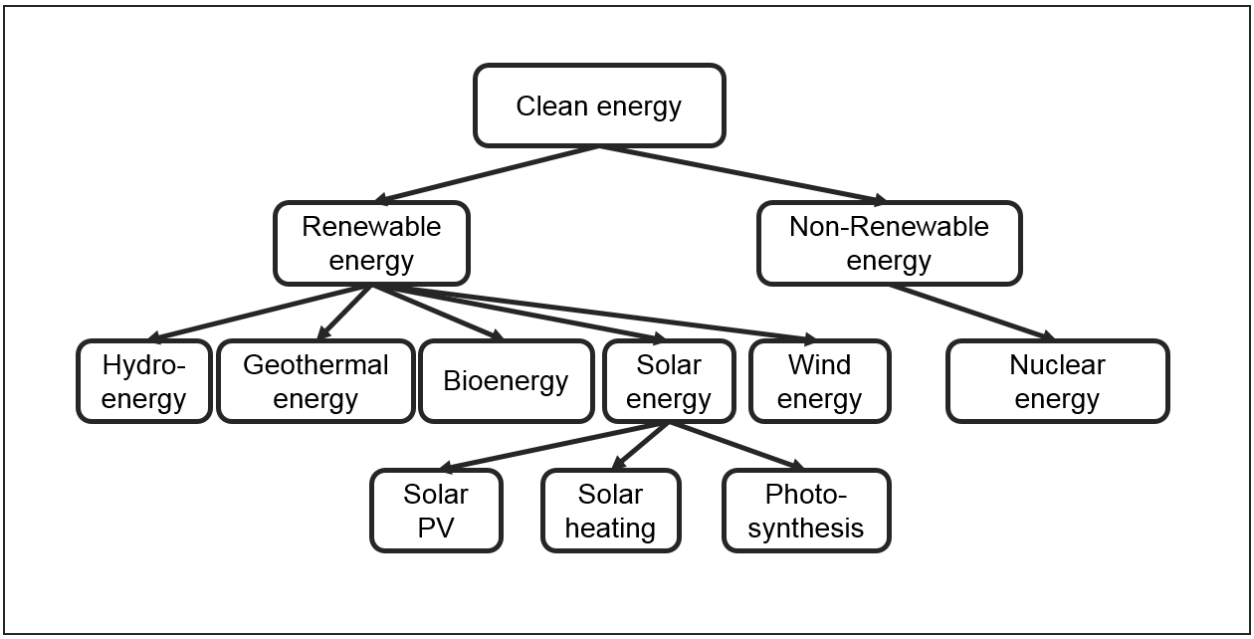

Fig. 1. Different types of renewable energies.

Generally speaking, as shown in Fig. 1, the available clean energy sources today can be sorted into two parts, renewable energy and non-renewable energy. Both of them show different merits and disadvantages. The major non-renewable clean energy is the nuclear energy. Even the nuclear energy exhibited the merits of high-energy density and non-emission, it is still facing the catastrophic threat of the nuclear leakage, for example, tens of thousands of peoples losing their houses in 1986 Chernobyl disaster of the nuclear plant in Ukraine [7], and in 2011 the accident of Fukushima nuclear plant caused by the earthquake resulted in huge environmental radical pollution [8]. Regarding the renewable energy, the wind power seems to be instable supply because it is strongly affected by the weather conditions. The hydropower is limited by geography locations because huge amount of water resource is necessary to drive the hydropower plant. The biomass power is complicated to use and with low energy density as well as the potential secondary pollution. Therefore, none of them listed above are suitable for our future energy. In addition, most of the renewable energy resources are indirectly formed from the solar energy, such as photosynthesis and heat. Consequently, the direct utilization of the solar energy seems to be the best choice for the future energy.

The solar energy demonstrates many more advantages than those discussed above. First, it comes from the sun and it is unlimited. The solar energy from the sun will not be changed in the

future thousands of years. Second, it is very abundant. The total solar energy illuminated on the earth is 50 billion Watts, making it the largest exploitable resource among the renewable energy resources. It can provide more energy in 1 hour to the earth than all of the energy consumed by humans in an entire year [9]. Third, the solar energy will not give obvious threating to our ecological systems because it can directly covert the solar energy into the electric power or heat without emissions. Therefore, the utilization of the solar energy will be the most promising method to overcome the energy crisis and the environmental pollution. As shown in Table 1, the solar energy is going to get more share in the energy market [10].

Table 1 World renewable energy use by type [10].

	2010	2020	2035
Electricity generation (TWh)	4206	6999	11342
Bioenergy	331	696	1,487
Hydro	3431	4513	5,677
Wind	342	1272	2,681
Geothermal	68	131	315
Solar PV	32	332	846
Concentrating solar power	2	50	278
Marine	1	5	57
Share of total generation	20%	25%	31%
Heat demand (Mtoe)	337	447	604
Industry	207	263	324
Buildings and agriculture	131	184	280
Share of total production	10%	12%	14%
Biofuels (mboe/d)	1.3	2.4	4.5
Road transport	1.3	2.4	4.4
Aviation	-	-	0.1
Share of total transport	2%	4%	6%

1.2 Photovoltaic technology

Many kinds of methods have been developed on the utilization of the solar energy, such as the light-to-heating conversion and the light-to-electricity conversion. In consideration of that the electric power is the most commonly used energy in our daily life and factories are supported by the electric power, the most acceptable way to utilize the solar energy must be the light-to-electric power conversion by using solar cells. Solar cells can directly convert the sun light into the electric power with the photovoltaic effect of semiconductors. They are very environmental-friendly without any gas emissions during generating electricity. However, the energy density of solar illumination is relative low (the standard irradiance AM1.5G = 1kW/m^2), which raises the cost of utilization and restraints the large-scale practical application of solar cells. Consequently, it is very necessary to improve the photovoltaic output of solar cells and reduce the cost.

1.2.1 History of photovoltaic technology

The photovoltaic effect was first discovered by Alexandre Edmond Becquerel in 1839. When the photovoltaic materials are exposed under the illumination, the photo-energy can be transferred into the electric power by solar cells, showing electric voltage or current output in the external circuit [11]. In 1954 the silicon solar cells were invented based on the P-N junction in the Bell Lab [12]. And in 1956 these silicon solar cells were merged into the PV module with output of megawatts, making them commercially available. Nowadays the commercialized silicon solar cells reached a power conversion efficiency up to 18% and were very common in our daily life. However, these solar cells were based on the monocrystalline or polycrystalline silicon materials. The preparation of these materials experiences high-temperature procedures, consumes huge amount of energy during the fabrication and create the secondary pollution. In addition, the silicon is an indirect bandgap semiconductor with a low absorption coefficient of 10^4 cm^{-1} magnitude [13]. As a result, the theoretical thickness of the silicon films should be higher than 100 μm for an effective absorption in silicon solar cells [14]. In this case, so far the cost of silicon solar cells is not comparable to other clean energy resources. Therefore, many kinds of new alternative solar cells aiming at the high power conversion efficiency and the low cost to process have been a research hotspot in the recent decades.

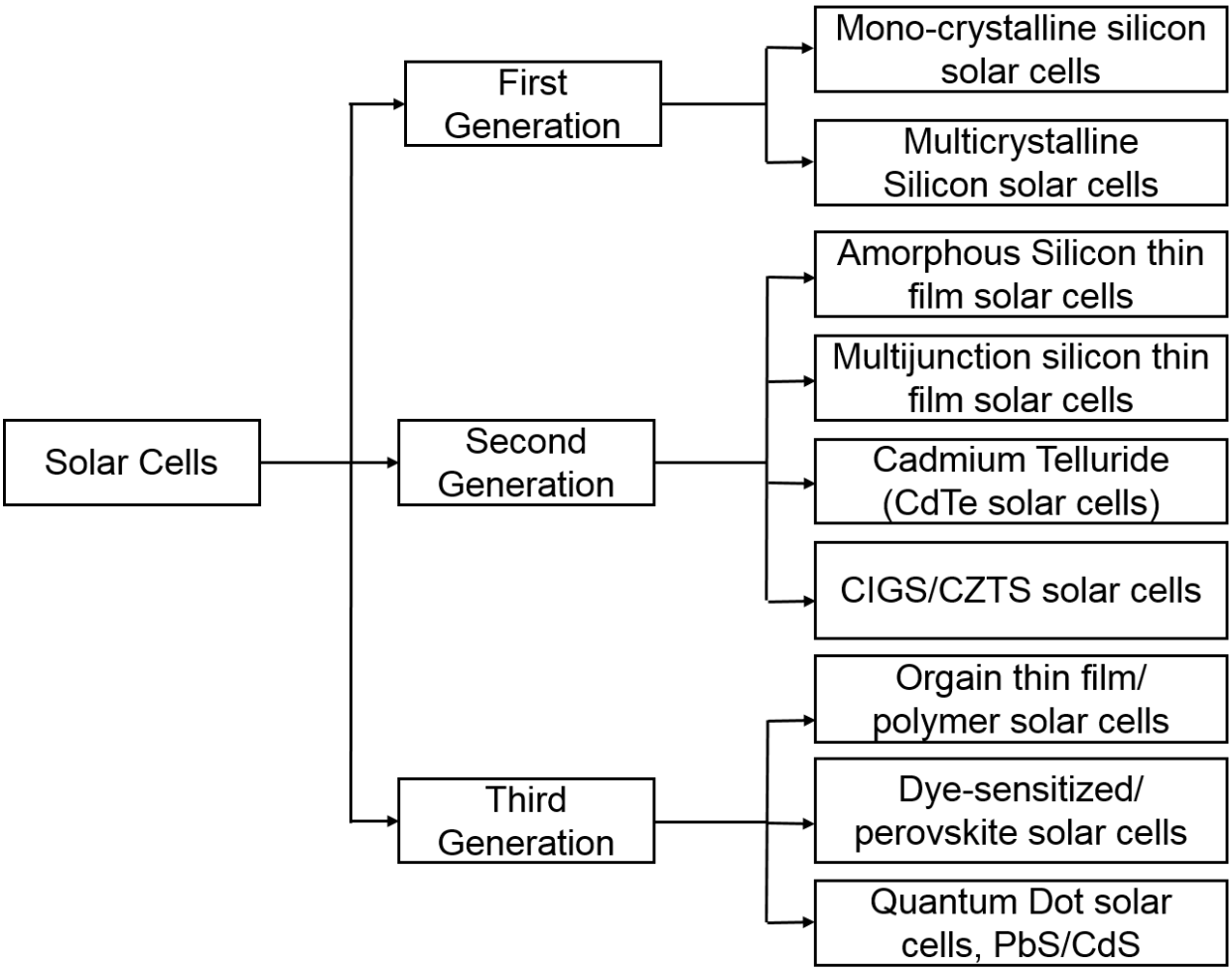

Fig. 2. Classification of various solar cell technology.

Many new kinds of solar cells have been developed in the recent decades. As shown in Fig. 2, depending on the manufacturing process and technologies, these solar cells are sorted as three generations. Their certified photovoltaic performance under the global AM1.5 spectrum (1000 W/m^2) at 25 °C are summarized in Table 2 [15]. The first generation solar cells are silicon solar cells, including polycrystalline silicon solar cells and monocrystalline silicon solar cells. They show the high power conversion efficiency (reaching 20.8% and 25.6%, respectively), high stability and commercial-available. However, the cost of the first generation solar cells is very high. The second generation solar cells are thin film solar cells, such as copper indium gallium selenide (CIGS) solar cells, copper zinc tin sulfide (CZTS) solar cells, gallium arsenide solar cells, amorphous silicon solar cells *et al.* Regarding the amorphous silicon solar cells, even their cost is lower than polycrystalline or monocrystalline silicon solar cells, their power conversion

efficiency is limited by the physical maximum and not so comparable to the first generation solar cells. Regarding the CIGS solar cells, their power conversion efficiency is comparable to silicon solar cells, but the resources of raw materials are not so abundant for large-scale commercialization. Gallium arsenide solar cells show higher power conversion efficiency than silicon solar cells, but with the much higher cost to process. The third generation solar cells include organic thin film/polymer solar cells, dye-sensitized solar cells/perovskite solar cells and quantum dot solar cells. Regarding the organic/ polymer and the dye-sensitized solar cells, they are low cost to process but the power conversion efficiency is low due to the narrow absorption region of the dyes, as well as the stability is not as comparable as silicon solar cells. Regarding the quantum dot solar cells and polymer solar cells, even though they are low cost and flexible, it is too hard to improve the power conversion efficiency to higher. Luckily, the perovskite solar cells developed recently are showing many advantages. As shown in Fig. 3, they have reached a high power conversion efficiency in short five years, with low cost and abundant raw materials to process. The perovskite solar cells are expected to be the next generation solar cells.

Table 2. Confirmed terrestrial cells and submodule efficiencies measured under the global AM1.5 spectrum (1000 W/m^2) at 25 °C [15].

Classification	Efficiency (%)	Area (cm^2)	V_{oc} (V)	J_{sc} (mA/cm^2)	Fill factor (%)	Test center (date)
Silicon						
Si (crystalline)	25.6 ± 0.5	143.7	0.740	41.8	82.7	AIST (2/14)
Si (multicrystalline)	20.8 ± 0.6	243.9	0.6626	39.03	80.3	FhG-ISE (11/14)
Si (thin transfer submodule)	21.2 ± 0.4	239.7	0.687	38.50	80.3	NREL (4/14)
Si (thin film minimodule)	10.5 ± 0.3	94.0	0.492	29.7	72.1	FhG-ISE (8/07)
III-V cells						
GaAs (thin film)	28.8 ± 0.9	0.9927	1.122	29.68	86.5	NREL (5/12)
GaAs (multicrystalline)	18.4 ± 0.5	4.011	0.994	23.2	79.7	NREL (11/95)

InP (crystalline)	22.1 ± 0.7	4.02	0.878	29.5	85.4	NREL (4/90)
Thin film chalcogenide						
CIGS (cell)	20.5 ± 0.6	0.9882	0.752	35.3	77.2	NREL (3/14)
CIGS (minimodule)	18.7 ± 0.6	15.892	0.701f	35.29	75.6	FhG-ISE (9/13)
CdTe (cell)	21.0 ± 0.4	1.0623	0.8759	30.25	79.4	Newport (8/14)
Amorphous/ microcrystalline Si						
Si (amorphous)	10.2 ± 0.3	1.001	0.896	16.36	69.8	AIST (7/14)
Si (microcrystalline)	11.4 ± 0.3l	1.046	0.535	29.07	73.1	AIST (7/14)
Dye sensitised						
Dye	11.9 ± 0.4	1.005	0.744	22.47	71.2	AIST (9/12)
Dye (minimodule)	10.0 ± 0.4	24.19	0.718	20.46	67.7	AIST (6/14)
Dye (submodule)	8.8 ± 0.3	398.8	0.697	18.42	68.7	AIST (9/12)
Organic						
Organic thin-film	11.0 ± 0.3	0.993	0.793	19.40	71.4	AIST (9/14)
Organic (minimodule)	9.5 ± 0.3	25.05	0.789	17.01	70.9	AIST (8/14)
Multijunction devices						
InGaP/GaAs/InGaAs	37.9 ± 1.2	1.047	3.065	14.27	86.7	AIST (2/13)
a-Si/nc-Si/nc-Si (thin-film)	13.4 ± 0.4	1.006	1.963	9.52	71.9	NREL (7/12)
a-Si/nc-Si (thin-film cell)	12.7 ± 0.4	1.000	1.342	13.45	70.2	AIST (10/14)

FhG-ISE represents Fraunhofer Institut für Solare Energiesysteme of Germany; AIST represents Japanese National Institute of Advanced Industrial Science and Technology. NREL represents National Renewable Energy Laboratory of the USA.

1.2.2 Perovskite materials and solar cells

The organic-inorganic hybrid perovskite solar cells have attracted much attention due to the low cost and high efficiency. In 2009 the halide $CH_3NH_3PbI_3$ perovskite was first applied into the solar cells by Miyazaka *et al.* as the dye, but they only exhibited an efficiency of 3.8% [16]. In addition, the solar cells were fabricated using the liquid hole transport materials, very unstable and quickly failed in a short time. In 2012 the solid state hole transport materials were introduced to fabricate the perovskite solar cells by Gratzel *et al*. These perovskite solar cells exceeded a power conversion efficiency of 9% as well as the improved stability [17]. From that on the perovskite solar cells have experienced a fast development. As shown in Fig. 3, by 2015 their power conversion efficiency has reached 20% [18,19]. Their development is much faster than the other solar cells. Beside the high efficiency, they also have showed other advantages, particularly the reduced cost. Perovskite solar cells can be processed via the room-temperature chemical solution method, which sharply reduced the processing cost, making them highly promising for the next generation solar cells.

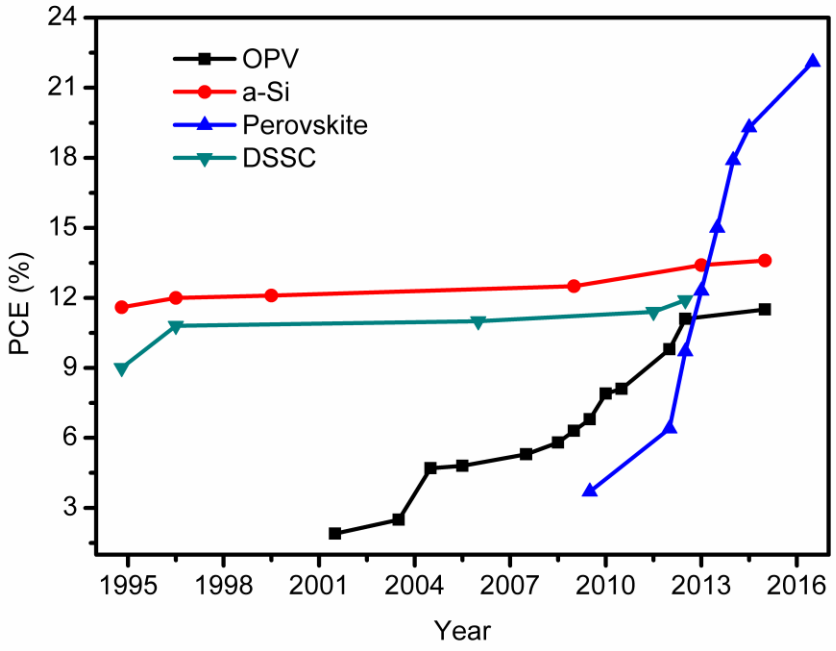

Fig. 3. Power conversion efficiency of different kind solar cells in the past twenty years [20].

1.2.3 Crystal structure of perovskite materials

Perovskites started from oxides materials. Natural mineral $CaTiO_3$ was first discovered by Russian scientist in 1839, and its crystal structure was named as perovskite. At the beginning perovskite materials were mainly referred as ABO_3 structured oxide materials, such as $CaTiO_3$, $BaTiO_3$, $PbTi_xZr_{1-x}O_3$, and $LaNiO_3$ [21]. Their typical structures were illustrated as Fig. 4. In these ABO_3 compounds, the *'A'* atom sits at cube corner positions (0, 0, 0), the *'B'* atom sits at body center position (1/2, 1/2, 1/2) and oxygen atoms sit at face-centered positions (1/2, 1/2, 0). Six O^{2-} cations form an octahedron structure and *'B'* ion locates at the center of the octahedron structure. The *'A'* atom located at the center of space formed by the octahedron.

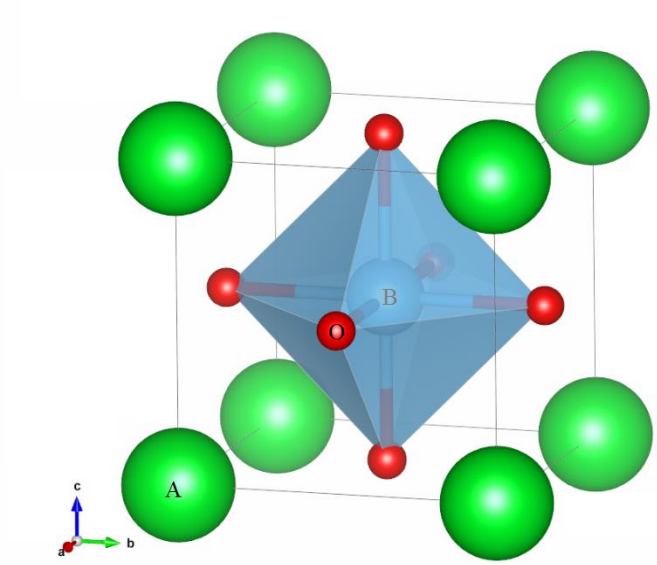

Fig. 4. Typical crystal structure of ABO_3 perovskite.

The structure stability of perovskite materials strongly depended on the parameter of the tolerance factor (t), which is determined by the radius of the atoms [22]. The tolerance factor is described by the radius of the A, B, O^{2-} ions as following equations.

$$t = \frac{R_A + R_O}{(R_B + R_O)\sqrt{2}} \quad (1)$$

where R_A is the radius of A ion, R_B is the radius of B ion, and R_O is the radius of O^{2-}. When the tolerance factor is approaching to 1.0, the crystal structure of perovskite is more likely cubic with

the space group of Pm3m. When it is a bit far away from 1.0, the crystal structure of ABO_3 would change correspondingly. For example, at room temperature $SrTiO_3$ is with *t* of 1.009 and the space group of Pm3m, and $CaTiO_3$ is with *t* of 0.973 and the space group of Pbnm. For the typical stable perovskite materials, such as $BiFeO_3$, $SrTiO_3$, $SrRuO_3$, $LaNiO_3$, $BaTiO_3$, $PbTiO_3$ and $PbTiO_3$, their tolerance factors were ranged from 0.78-1.05 [23].

According to the tolerance factor, the halide organic-inorganic perovskites can also be formed stably, where the *'A'* site is the organic ion, the *'B'* site is metal ion, and the 'O' atom is replaced by the halide cation X^- (I^-, Br^- and Cl^-). The R_{A+}, R_{B2+}, R_{I-} of the halide perovskite $CH_3NH_3PbI_3$ are 2.37, 1.33, 2.06 Å, respectively. Correspondingly, its tolerance factor was calculated as 0.924, which make it structural-stable formed [23].

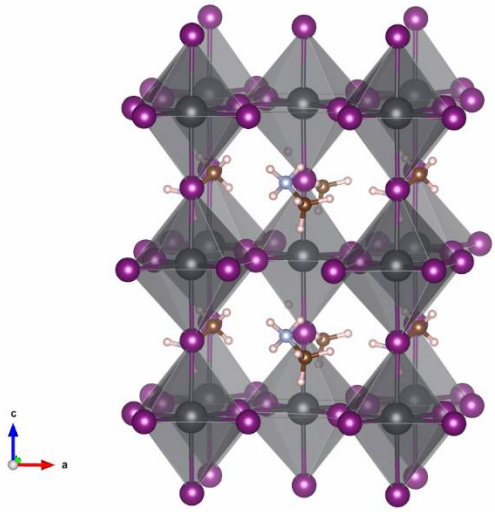

Fig. 4. Typical crystal structure of $CH_3NH_3PbI_3$ perovskite.

Apart from the ABO_3 and ABX_3 structured perovskites, some other perovskite structures were also developed, such as layered perovskites, double perovskites $AA'BB'O_6$ or $AA'BB'X_6$, triple perovskites [24-28]. Layered perovskites varied with each other based on the chemical makeup and they can be defined as following. 1) Aurivillius phase layered perovskite materials, in which the intruding layer is composed of an alkali metal (M) every n ABO_3 layers, with the chemical formula of $[Bi_2O_2]^-A_{(n-1)}B_2O_7$ [24]; 2) Dion-Jacobson phase, in which the intruding layer is composed of an alkali metal (M) every n ABO_3 layers, giving the overall formula as $M_1^+A_{(n-1)}B_nO_{(3n+1)}$ [25]; 3) Ruddlesden-Popper phase, in which the intruding layer occurs between n (n = 1 or 2) layers of the ABO_3 or ABX_3 lattices, with the formula of

$(BA)_2(MA)_{n-1}Pb_nI_{3n+1}$ [26]; 4) The double perovskites $AA'BB'O_6$ or $AA'BB'X_6$ and triple perovskites are derived from single perovskites with the *'A'* site or *'B'* site atoms half-replaced by the second/third atoms, such as La_2NiMnO_6, Bi_2FeCrO_6, $Cs_2BiNaBr_6$, $Cs_2BiNaCl_6$, $La_3Ba_3Ca_xCu_{6+x}O_y$ ($0 \leq x \leq 3$) and $Ba_3ZnRu_{2-x}Ir_xO_9$ (x= 0,1,2) [27,28]. The tolerance factor of double perovskites can be calculated from the average radius of the each site, e.g., for the double perovskite Bi_2FeCrO_6, the tolerance factor was evaluated as following.

$$t = \frac{R_{Bi} + R_O}{(R_{Beffective} + R_O)\sqrt{2}} \quad (2)$$

$$R_{Beffective} = (R_{Cr3+} + R_{Fe3+})/2 \quad (3)$$

1.2.4 Properties of perovskite materials

The structures of perovskite materials vary with each other, resulting in abundant physical properties. Particularly, their structures will change with the environmental fields, such as electric field, mechanical force, temperature and irradiance *et al*. accordingly, they exhibit the piezoelectric and ferroelectric properties, magnetic properties, pyroelectric properties, and electro-elastic properties, insulating properties, semiconductivity and superconductivities *et al*. The abundant physical properties make perovskite materials widely used in our daily life and industries. For example, PZT series of perovskites have been widely used as high-performance sensors, different kinds of energy converters, detectors, superconductors, insulators, electrodes and semiconductors [27]. The formation of double/triple perovskites leads to more abundant physical properties. Due to the spin orbital coupling and hybridization, some of double/triple perovskite materials processed lower indirect bandgaps than single perovskites, various optical properties, catalytic properties and magnetic properties [29]. The complex structures also resulted in the formation of oxygen vacancy and high ion mobility, making them excellent cathodes for fuel cells or superconductors [28].

The bandgap of perovskite is one of the key factors affecting their application on solar cells. Most of the ABO_3 perovskite oxides, such as $SrTiO_3$ and PZT53/47, have a band gap higher than 3.0 eV. $BiFeO_3$ was reported with the bandgap of 1.9-2.7 eV, but it is still too high for the visible light absorption. Even though doping can reduce the bandgap of perovskite oxides, e.g. Fe-doped $SrFe_xTi_{1-x}O_{3-\beta}$, it simultaneously introduces many defects which can perform as trapping centers

and seriously do harm to photovoltaic performance of solar cells. Therefore, most of the ABO_3 perovskite reported are not suitable as the absorbing materials for solar cells. Instead, most of them are used as insulating sensors *et al.* Particularly, the valence states of single ABO_3 perovskites are very low, which bring some more problems for energy level matching in solar cells.

Luckily, the organic-inorganic halide perovskites ABX_3 are amazing semiconductor materials developed recently. As show in Table 3, they have lower bandgaps than ABO_3 oxide perovskites. Especially, the $CH_3NH_3PbI_3$ perovskites are direct bandgap semiconductors showing an excellent absorption in the visible light region. Their bandgap is 1.5 eV and their absorption coefficient reaches 10^5 cm^{-1} in the visible light region.

Table 3. Theoretical bandgaps and experimental bandgaps of perovskite materials [22-28].

Perovskites	Theoretical bandgap (eV)	Experimental bandgap (V)
$BiFeO_3$	1.9-2.7	1.9-2.7
$PbTiO_3$	2.87	3.2
$SrTiO_3$	3.57	3.75
γ-$CsSnI_3$	1.3±0.1	1.3
$CH_3NH_3PbI_3$	1.3-1.61	1.50-1.61
$CH_3NH_3PbBr_3$	2.3	2.32
$CH_3NH_3PbI_{3-x}Cl_x$	-	1.55-1.64
$HC(NH_2)_2PbI_3$	1.47	1.47

1.2.5 Preparation of perovskite materials

Perovskite materials are a large family, consequently there are many kinds of methods to prepare perovskite materials. Regarding the perovskite oxides, most of them need a high temperature sintering procedure to synthesize, but the low temperature solution method is not available. Detailed methods to prepare ABO_3 perovskite materials include sol-gel method, sintering methods, chemical vapor deposition and physical vapor deposition *et al*. In a long time the low-temperature sintering is one important research topic on perovskites oxides to reduce the cost because the high temperature processing consumes a lot of energy. Moreover, most of the

perovskite oxide solar cells were processed through high temperature, *e.g.* $BiFeO_3$ Schottky solar cells were fabricated at a temperature of 550 centigrade and different atmosphere, which consumed much energy. These procedures also brought in some other problems, including the formation of defects due to the inhomogeneity of films, which worsen the photovoltaic performance of oxide perovskite solar cells.

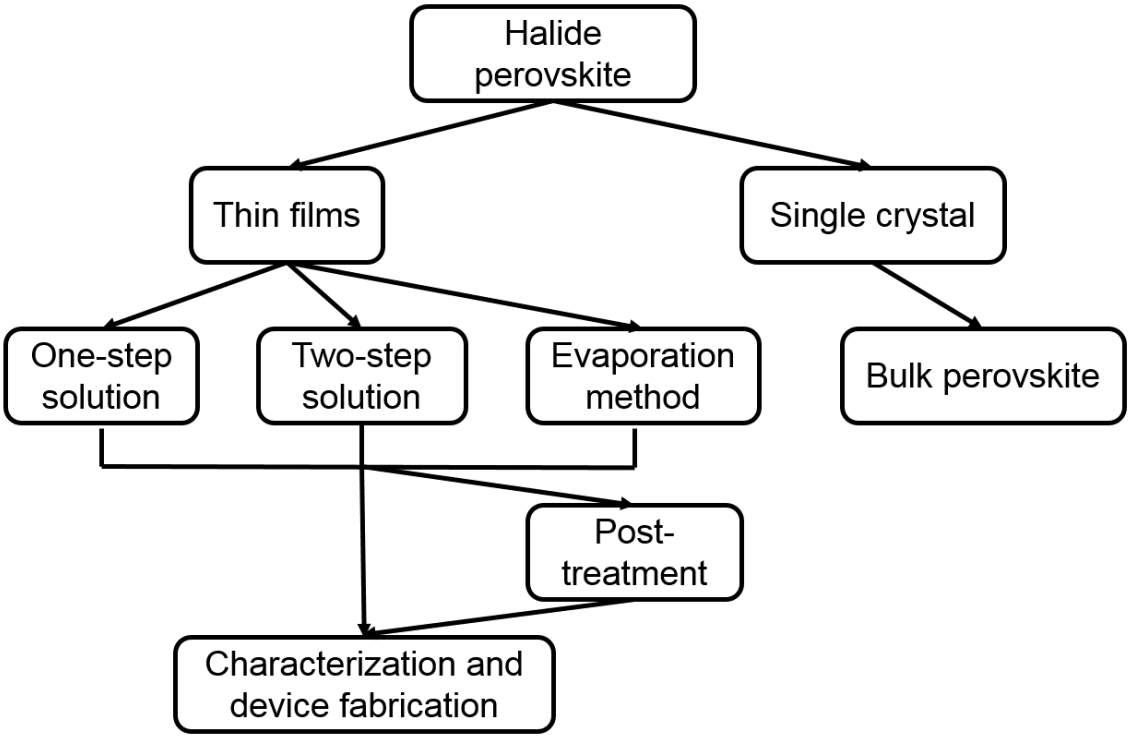

Fig. 5. Typical procedure to prepare $CH_3NH_3PbI_3$ perovskite.

Interestingly, the ABX_3 and other halide-based perovskites were reported as low temperature solution-processable. Fig. 5 showed the main methods to prepare halide perovskite materials. Huang *et al.* prepared the $CH_3NH_3PbI_3$ singe crystal by a solution method. In this method the stoichiometric ratio of $Pb(CH_3COOH)_2 \cdot 3H_2O$ and CH_3NH_3I were dissolved into the aqueous HI solution, and then heated and stirred. After that the temperature was lowered down to grow a black tetragonal single perovskite $CH_3NH_3PbI_3$ with the size of 10 mm × 10 mm × 8 mm. This $CH_3NH_3PbI_3$ single crystal showed excellent electric and optical properties. As shown in Fig. 6, Hui-Seon Kim *et al.* developed a one-step method by dissolving stoichiometric PbI_2 and CH_3NH_3I into the γ-butyrolactone solutions and spin coated it [17]. Nam-Gyu Park *et al.*

developed a two-step method to prepare perovskite thin films via spin coating [29]. The main procedures of this method are illustrated in Fig. 7, at the beginning the PbI_2 films was deposited on the mesoporous TiO_2 layers, and then the CH_3NH_3I solution was loaded to react with PbI_2 films and spin coated to form perovskite layers.

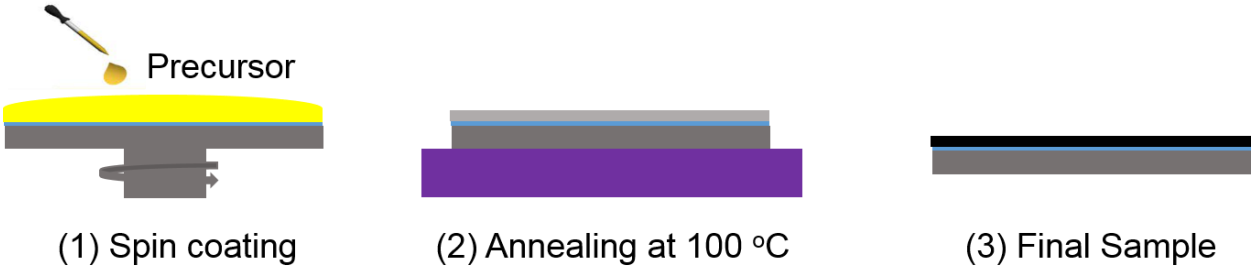

Fig. 6. Typical procedures of one-step preparation of $CH_3NH_3PbI_3$ perovskite.

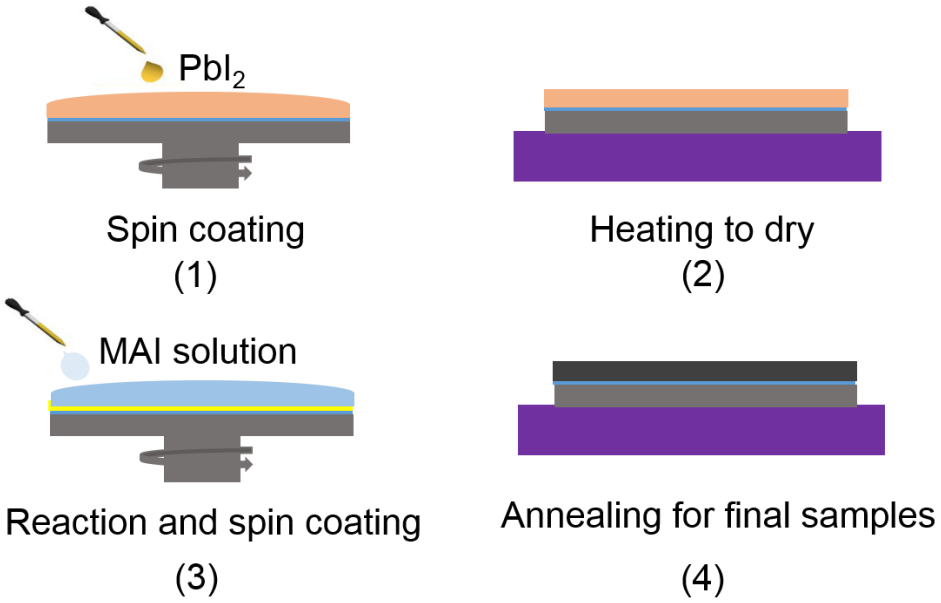

Fig. 7. Typical procedures of two-step preparation of $CH_3NH_3PbI_3$ perovskite.

1.2.6 Architectures of perovskite solar cells

Depending on the architectures, there are two kinds of perovskite solar cells, the mesoporous structured perovskite solar cells and the planar structured solar cell [17,18]. The normal architecture of mesoporous structured perovskite solar cells can been seen in Fig. 8. In this structure the FTO glass was performed as the transparent electrode. It was coated by the electron

selective layers (also named as the compact layer or blocking layer), such as the dense TiO_2 layer, ZnO layer and SnO_2 layer *et al.* [17,18,30,31], the electron selective layers can block the hole into the FTO, but let the electron transport to the FTO. In this case, the charge mobility and the coverage of the electron selective layer are very important for the high-performance perovskite solar cells. After the formation of the electron selective layer, mesoporous TiO_2 was coated on the dense TiO_2 layer to load perovskite layers and for a better charge transportation. Snaith *et al.* also used the meso-Al_2O_3 as scaffold to fabricate the devices, they showed better stability than that with TiO_2 [32]. The perovskite layers were prepared on the mesoporous TiO_2 layers as the dyes by two-step solution method or sequential deposition method *et al*. And then the hole transport layers, such as the lithium and cobalt doped Spiro, P3HT and CuSCN, were spin coated on the perovskite layer to transport holes [17,18,33,34]. Finally, the metal electrode, such as gold, silver and aluminum was deposited to make devices. Another structure for the mesoporous structured perovskite solar cell is the inverted mesoporous structure. In this structure, the device was processed from the hole transport layer. ITO glass was performed as the transparent electrode, and the hole transport (PEDOT:PSS or NiO_x) layer was coated on it, and then the perovskite layer, electron transport layer (PCBM and TiO_2 *et al.*), and metal electrodes were processed step by step [35]. Some compact layer-free perovskite solar cells and HTM-free perovskite solar cells have also been developed, but so far their performances are not so comparable to the devices mentioned above. Expect for the metal electrode, carbon was also introduce to assemble perovskite solar cells, and they performed well as excellent hole transport materials and electrode. E.g., Han *et al.* applied the carbon paste on the perovskite films as the hole absorbing layer and electrode, reaching high-performance stable perovskite solar cells with a structure of FTO/CL-TiO_2/meso-TiO_2/ZrO_2 &perovskites/carbon electrode [36].

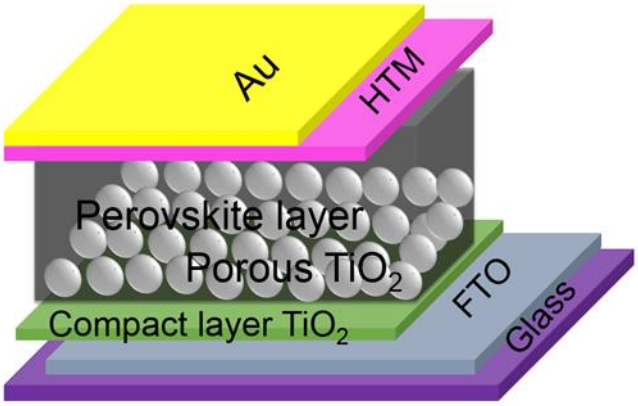

Fig. 8. Typical normal structure of $CH_3NH_3PbI_3$ perovskite solar cells.

The typical architecture of the planar structured perovskite solar cells was illustrated in Fig. 9. This kind of solar cells were normally processed by the one-step method, where $PbCl_2$& CH_3NH_3I mixture solutions were spin coated on the compact layer and annealed. They are easier to fabricate than mesoporous structured perovskite solar cells, but usually show larger hysteresis during the *I-V* characterization [37].

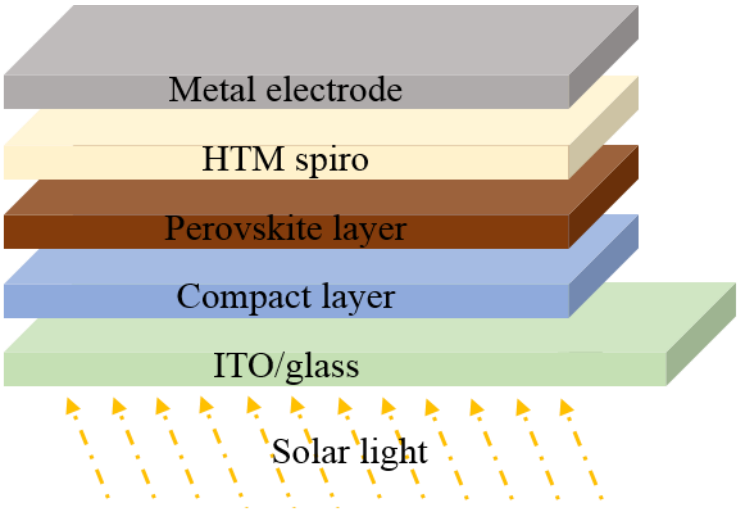

Fig. 9. Typical structure of planar halide perovskite solar cells.

1.2.7 Energy diagram and working principles of perovskite solar cells

The perovskite solar cells were more likely to be solid state dye-sensitized solar cells. Its

working principle was evaluated from the dye-sensitized solar cells. With the energy diagram shown in Fig. 10, the working principle of the perovskite solar cells can be described as following. When the incident light was applied, the photons were absorbed and generated the electron-hole pairs. The photon-excited electrons were moved to the conduction band, while the holes were excited to the valence band. Because the conduction band of the perovskite layer was higher than that of the electron selective layers (such as TiO_2, ZnO) [17,38], the photon-excited electron can diffuse into the compact layer. At the same time, the photon-excited hole was absorbed by the hole transport layer. According to the energy diagram, the physical maximum of the open-circuit voltage (V_{oc}) was mainly determined by the difference between the conduction band of electron selective layer and the valence band of the hole transport layer. However, sometimes the mechanism seems to be more complicated. For instance, the conduction band of SnO_2 was -4.5 eV, but the V_{oc} of the device was up to 1.1 V, which was much higher than that expected [39]. Therefore, someone argued that it is more likely V_{oc} can be determined by the conduction band of the perovskite layer. Unfortunately, so far there were no strong evidences to support this idea.

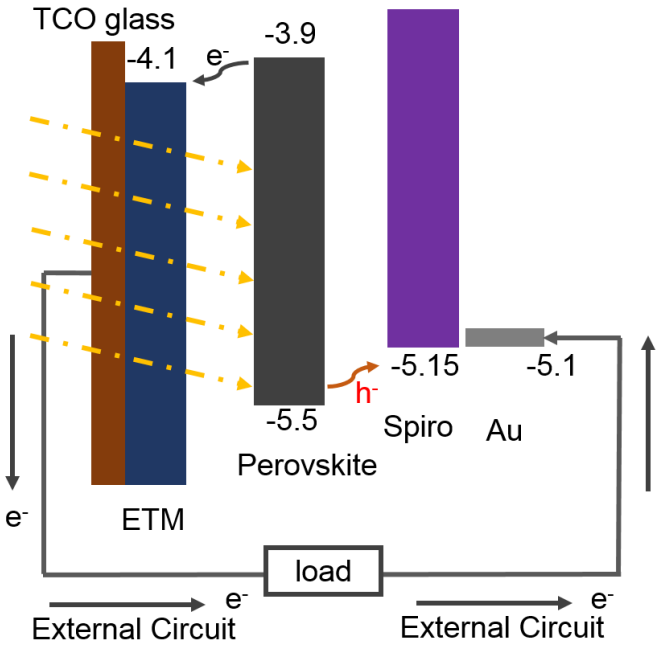

Fig. 10. Energy level diagram and working principle of typical halide perovskite solar cells.

The mechanism for the high-performance of perovskite solar cells is very complicated. From the aspect of the absorbing layer, it can be explained as following. First, the $CH_3NH_3PbI_3$ perovskite materials are direct band gap semiconductors with a bandgap of ca. 1.5 eV. They have the high absorption (absorption coefficient up to 10^5 cm^{-1}) in the visible light region (the visible region processed 45% energy of the solar irradiance). Second, the perovskite materials show small weight of effective electron mass and hole mass, a long effective charge carrier distribution length. This can reduce the recombination of the photon-excited electron-hole pairs and benefit their separation. Accordingly, the monochromatic incident photon-to-electron conversion efficiency can reach 85% [29]. Third, there are multi-excitation phenomenon in the perovskite layers of the solar cells, which favored the improvement of power conversion [37]. Forth, as shown in Fig. 10, the energy level of each part matches well with each other. Therefore, with proper architectures, the perovskite solar cells are expected to comparable with GaAs solar cells [37].

However, there are still many challenges for perovskite solar cells. First, the halide perovskite solar cells are facing the problems of hysteresis and stability. This is believed to strongly depend on the quality of the perovskite films, such as crystallization, grain size, coverage and interfaces. Well crystallization, large grain and full coverage are considered to benefit the high-performance perovskite solar cells. Second, the halide perovskite solar cells are facing the problem of the lead pollution because the perovskite layer consists of some lead element. The lead pollution is a serious problem which can result in the disaster of the ecological system. To overcome this problem, the development of lead-free or lead-less absorbing materials is basically necessary.

1.2.8 Lead-free perovskite materials and solar cells

Lead pollution is a serious problem that might result in the damage of nervous system. As for perovskite solar cells, how to dealing the lead pollution is a big challenge. Before the development of lead-halide perovskite solar cells, the oxide perovskite solar cells has been studied, such as PZT solar cells, $BiFeO_3$ solar cells [38-41]. $BiFeO_3$ has a smaller tolerance factor than PZT, with a typical structure of *R-3* and the band gap from 2.1-2.7 eV. With $BiFeO_3$ as absorbing layer, $BiFeO_3$ oxide solar cells were mainly processed as Schottky Solar cells with the structure of $SrRuO_3$/ $BiFeO_3$/ITO or ITO/TiO_2/$BiFeO_3$/Au. However, the $BiFeO_3$ solar cells

exhibited a very low efficiency seldom higher than 1%, mainly due to the large band gap and the low absorbing coefficient. Apart from $BiFeO_3$, Bi_2FeCrO_6 double perovskites have been investigated for the solar cells. The theoretical calculation indicated that the introduction of Cr into the $BiFeO_3$ can sharply affect the optical properties and electronic structures. Nechache *et al.* have applied the pulsed laser deposition to grow the Bi_2FeCrO_6 double perovskite films and fabricated the solar devices with the structures of Nb-doped $SrTiO_3$ substrate/$SrRuO_3$/ Bi_2FeCrO_6 /ITO and Nb-doped $SrTiO_3$ substrate/ Bi_2FeCrO_6/ITO. By controlling the deposition speed and atmosphere, they tuned the band gap and absorption of the Bi_2FeCrO_6 perovskites, and reached a power conversion efficiency (*PCE)* of 8.1% in small size solar cells [42]. So far the *PCE* of 8.1% is the highest record reported in the lead-free oxide perovskite solar cells. However, the preparation of Bi_2FeCrO_6 is very sensitive to the processing environment, and they have only been prepared by the Pulsed laser deposition method with the serious controlled environment. So far it is difficult to prepare Bi_2FeCrO_6 double perovskites from low-cost ways.

Regarding the halide perovskite solar cells, due to the limitation of tolerance factor, the *A* site atom can only be CH_3NH_3, $(NH_2)_2CH$, Cs *et al*. Due to the limitation of the chemical balance, the *B* site atom can be Sn, Mg, Sr, Ca et al. The lead-free Sn-based single perovskites do exhibit a proper band gap and good absorbing properties. Unfortunately, Sn^{2+} ions are easy to be oxidized and very unstable in the environment with oxygen. Particularly, the Sn-based single perovskite materials possessed a high carrier concentration, which sharply reduce the effective carrier diffusion length [43]. Regarding the Mg, Sr and Ca *et al.* based halide single perovskites, the theoretical calculation indicated that there would not enough spin orbital coupling between *B*-site atoms and *X* atoms [44]. In this case their band gaps are too high and no enough effective photon-excitation would occur under illumination. So far there are no proper single halide perovskite materials reported with excellent optical properties expect the Pb and Sn based perovskites. Double perovskite Cs_2SnI_6 showed a proper band gap and the excellent spectral absorption. However, there is a crystal structure defect at the *B*-site. This internal defects can perform as the trapping centers and sharply affected the effective electron-hole excitation and extraction properties. So far there was not high efficient Cs_2SnI_6 based solar cells reported [45].

The bismuth/ antimony halide multiple perovskites might be potential lead-free candidates. Bismuth halide perovskites, such as $(CH_3NH_3)_3Bi_2I_9$, $Cs_3Bi_2I_9$, $(CH_3NH_3)_3Bi_2I_{9-x}Cl_x$ are layer-structured materials with the hexagonal crystal structure. They can be easily prepared by the

chemical solution method. Erik M. J. Johansson *et al.* used these perovskites to fabricate the solar devices with the structure of FTO/CL-TiO_2/m-TiO_2&Bismuth perovskite/Spiro/Au [46]. They reached a power conversion efficiency of 1.07%, but so far it is too hard to improve higher. As shown in Table 4, most of the bismuth and antimony halide perovskites have the band gap higher than 2.0 eV, which is too large for the effective visible spectral absorption [47-49].

Table 4. Summarization of the lead-free materials and their physical properties [43-50].

Substances	Carrier concentration (cm^{-3})	Band gap (eV)	With Pb (Y/N)	Stable (Y/N)	Absorption efficient (cm^{-1})	Valence band (eV)	Conduction band (eV)
$(CH_3NH_3)_3Bi_2I_9$	10^{16}	2.1	N	Y	low	-6.0	-3.9
$CsSnI_3$	10^{19}	1.3	N	N	high	-	-
SnF_2-doped $CsSnI_3$	10^{17}	-	N	N	-	-	-
$CH_3NH_3PbI_3$	10^9	1.5	Y	N	10^5	-5.4	-3.9
$BiFeO_3$	-	2.1-2.5	N	Y	low	-6.1	-3.8/-4.0

(N represents Not, Y represents Yes.)

1.3 Challenges and Research topic

As discussed above, the halide perovskite solar cells are becoming the promising next generation solar cells. However, they are still facing many challenges. First, higher power conversion efficiency is necessary to make it more comparable to commercialized silicon solar cells. Second, the perovskite solar cells should be stable and hysteresis-less. Third, lead-pollution problem should be resolved to make the devices commercial applicable.

Among these challenges list above, the absorbing layer played the key role on the performance of the solar cells. In order to promote the further development of perovskite solar cells, in this thesis I tried to investigate them by studying perovskite absorbing layers. First, the crystallization, surface morphology and grain size are key points affecting the performance of perovskite solar cells. Therefore, first, the high-quality halide perovskite absorbing layers were prepared via the controlled growth of thin films for higher performance perovskite solar cells in

this thesis. Second, lead-free materials were studied as the absorbing layers. The surface morphology modification effect was investigated on the photovoltaic performance of lead-free halide materials for perovskite solar cells. And the lead-free stable oxide double perovskite materials were also explored for potential application on solar cells.

Reference

[1] R.F. Service, Is it time to shoot for the sun? Science 2005, **309** (5734), 548-551.

[2] J. Potočnik, Renewable energy sources and the realities of setting an energy agenda, Science 2007, **315** (5813), 810-811.

[3] U.S. Energy Information Administration, International Energy Outlook 2016, Chapter 5: Electricity.

[4] Chen Cao, Wenjun Jiang, Buying Wang, Jianhuo Fang, Jidong Lang, Geng Tian, Jingkun Jiang, and Ting F. Zhu, Inhalable microorganisms in Beijing's PM2.5 and PM10 pollutants during a severe dmog event, Environ. Sci. Technol. 2014, **48** (3), 1499-1507.

[5] G.C. Tiao, G.E.P. Box, W.J. Hamming, Analysis of Los Angeles photochemical smog data: A statistical overview, J. Air Pollut. Control Assoc. 1975, **25** (3), 260-268.

[6] A. Brown, S. Müller, Z. Dobrotkova, Renewable energy: Markets and prospects by technology, IEA information paper. 2011.

[7] United States Nuclear Regutory Commission Report. http://www.nrc.gov/reading-rm/doc-collections/fact-sheets/chernobyl-bg.html.

[8] P.Y. Lipscy, K.E. Kushida, T. Incerti, The Fukushima disaster and Japan's nuclear plant vulnerability in comparative perspective, Environ. Sci. Technol. 2013, **47** (12), 6082-6088.

[9] Nathan S. Lewis and Daniel G. Nocera, Powering the planet: Chemical challenges in solar energy utilization, PNAS 2006, **103** (43), 15729-15735.

[10] T.O. Saetre, O.M. Midtgård, G.H. Yordanov, A new analytical solar cell *I-V* curve model, Renew. Energy 2011, **36** (8), 2171-2176.

[11] Palz, Wolfgang, Power for the world - The emergence of electricity from the sun, Belgium: Pan Stanford Publishing. 2010, 6.

[12] D.M. Chapin, C.S. Fuller, G.L. Pearson, A new silicon p‐n junction photocell for converting solar radiation into electrical power, J. Appl. Phys. 1954, **25**, 676-677.

[13] Han Wang, Xianglei Liu, Zhuomin M. Zhang, Absorption coefficients of crystalline silicon at wavelengths from 500 nm to 1000 nm, International Journal of Thermophysics 2013, **34** (2), 213-225.

[14] Tom Tiedje, Eli Yablonovitch, George D. Cody and Bonnie G. Brooks, Limiting efficiency of silicon solar cells, IEEE Transactions on Electron Devices 1984, **31** (5), 711-716.

[15] Martin A. Green, Keith Emery, Yoshihiro Hishikawa, Wilhelm Warta and Ewan D. Dunlop,

Solar cell efficiency tables (Version 45), Prog. Photovolt: Res. Appl. 2015, **23**, 1-9.

[16] A. Kojima, K. Teshima, Y. Shirai, T. Miyasaka, Organometal halide perovskites as visible-light sensitizers for photovoltaic cells, J. Am. Chem. Soc. 2009, **131**, 6050-6051.

[17] Hui-Seon Kim, Chang-Ryul Lee, Jeong-Hyeok Im, Ki-Beom Lee, Thomas Moehl, Arianna Marchioro, Soo-Jin Moon, Robin Humphry-Baker, Jun-Ho Yum, Jacques E. Moser, Michael Grätzel & Nam-Gyu Park, Lead iodide perovskite sensitized all-solid-state Submicron Thin Film Mesoscopic Solar Cell with Efficiency Exceeding 9%, Scientific Reports, 2012, **2**, 591-597.

[18] Mingzhen Liu, Michael B. Johnston & Henry J. Snaith, Efficient planar heterojunction perovskite solar cells by vapour deposition, Nature 2013, **501**, 395-398.

[19] Dianyi Liu, Timothy L. Kelly, Perovskite solar cells with a planar heterojunction structure prepared using room-temperature solution processing techniques, Nature Photonics 2014, **8**, 133-138.

[20] National Renewable Energy Laboratory USA, Best research-cell efficiencies. http://www.nrel.gov/pv/assets/images/efficiency_chart.jpg.

[21] A. S. Bhalla, R. Guo, R. Roy, The perovskite structure - a review of its role in ceramic science and technology, Mat. Res. Innovat. 2000, **4**, 3-26.

[22] V.M. Goldschmidt, Die Gesetze der Krystallochemie, Naturwissenschaften, 1926, **14**, 477-485.

[23] Wan-Jian Yin, Tingting Shi, and Yanfa Yan, Unique properties of halide perovskites as possible origins of the superior solar cell performance, Adv. Mater. 2014, **26**, 4653-4658.

[24] Kurt R. Kendall, Carlos Navas, Julie K. Thomas *et al.*, Recent developments in oxide ion conductors: Aurivillius phases, Chem. Mater. 1996, **8** (3), 642-649.

[25] Mirabbos Hojamberdiev *et al.,* New Dion-Jacobson phase three-layer perovskite $CsBa_2Ta_3O_{10}$ and its conversion to nitrided $Ba_2Ta_3O_{10}$ nanosheets via a nitridation-protonation - intercalation-exfoliation route for water splitting, Cryst. Growth Des. 2016, **16** (4), 2302-2308.

[26] Hsinhan Tsai *et al*., High-efficiency two-dimensional Ruddlesden-Popper perovskite solar cells, Nature 2016, 536, 312-316.

[27] Christopher N. Munnings *et al.*, Structure, stability and electrical properties of the $La_{(2-x)}Sr_xMnO_{4\pm\delta}$ solid solution series, Solid State Ion. 2006, **177** (19-25), 1849-1853.

[28] H. Asano, J. Hayakawa and M. Matsui, Preparation and properties of triple perovskite $La_{3-3x}Ca_{1+3x}Mn_3O_{10}La_{3-3x}Ca_{1+3x}Mn_3O_{10}$ ferromagnetic thin films, Appl. Phys. Lett. 1997, **71**,

844.

[29] Jeong-Hyeok Im, In-Hyuk Jang, Norman Pellet, Michael Grätzel, Nam-Gyu Park, Growth of $CH_3NH_3PbI_3$ cuboids with controlled size for high-efficiency perovskite solar cells, Nat. Nanotechnol. 2014, **11** (9), 927-932.

[30] Dae-Yong Son, Jeong-Hyeok Im, Hui-Seon Kim, Nam-Gyu Park, 11% efficient perovskite solar cell based on ZnO nanorods: An effective charge collection system, J. Phys. Chem. C 2014, **118** (30), 16567-16573.

[31] Qingshun Dong, Yantao Shi *et al*., Insight into perovskite solar cells based on SnO_2 compact electron-selective layer, J. Phys. Chem. C 2015, **119** (19), 10212-10217.

[32] Michael M. Lee, Joël Teuscher, Tsutomu Miyasaka, Takurou N. Murakami, Henry J. Snaith, Efficient hybrid solar cells based on meso-superstructured organometal halide perovskites, Science, 2012, **338** (6107), 643-647.

[33] Senyun Ye, Weihai Sun *et al.*, CuSCN-based inverted planar perovskite solar cell with an average *PCE* of 15.6%, Nano Lett. 2015, **15** (6), 3723-3728.

[34] Jian Liu, Yongzhen Wu *et al*., A dopant-free hole-transporting material for efficient and stable perovskite solar cells, Energy Environ. Sci. 2014, **7**, 2963-2967.

[35] Jingbi You, Ziruo Hong *et al.*, Low-temperature solution-processed perovskite solar cells with high efficiency and flexibility, ACS Nano 2014, **8** (2), 1674-1680.

[36] Anyi Mei, Xiong Li, Hongwei Han, A hole-conductor-free, fully printable mesoscopic perovskite solar cell with high stability, Science, 2014, **345** (6194), 295-298.

[37] L.M. Pazos-Outón, M. Szumilo, R. Lamboll, J.M. Richter, M.C. Quesada, M.A. Jalebi, H.J. Beeson, M. Vrućinić, M. Alsari, H.J. Snaith, B. Ehrler, Photon recycling in lead iodide perovskite solar cells, Science 2016, **351** (6280), 1430-1433.

[38] Eran Edri, Saar Kirmayer, Sabyasachi Mukhopadhyay, Konstantin Gartsman, Gary Hodes, David Cahen, Elucidating the charge carrier separation and working mechanism of $CH_3NH_3PbI_{3-x}Cl_x$ perovskite solar cells, Nature Comm. 2014, **5**, 3461.

[39] Peng Gao, Michael Grätzel, Mohammad K Nazeeruddin, Organohalide lead perovskites for photovoltaic applications, Energy Environ. Sci. 2014, **7**, 2448-2463.

[40] Qi Jiang, Liuqi Zhang, Haolin Wang, Xiaolei Yang, Junhua Meng, Heng Liu, Zhigang Yin, Jinliang Wu, Xingwang Zhang & Jingbi You, Enhanced electron extraction using SnO_2 for high-efficiency planar-structure $HC(NH_2)_2PbI_3$-based perovskite solar cells, Nature Energy, 2016, **2**,

16177.

[41] Soumyo Chatterjee, Abhijit Bera, and Amlan J. Pal, p-i-n Heterojunctions with $BiFeO_3$ Perovskite nanoparticles and p- and n-type oxides: Photovoltaic properties, ACS Appl. Mater. Interfaces 2014, **6** (22), 20479-20486.

[42] Meng Qin, Kui Yao and Yung C. Liang, High efficient photovoltaics in nanoscaled ferroelectric thin films, Appl. Phys. Lett. 2008, **93**, 122904.

[43] R. Nechache, C. Harnagea *et al.*, Bandgap tuning of multiferroic oxide solar cells, Nature Photonics 2015, 9, 61-67.

[44] Zhuo Chen, Jian J. Wang, Schottky solar cells based on $CsSnI_3$ thin-films, Appl. Phys. Lett. 2012, 101, 093901.

[45] BAI Xiao-Gong, SHI Yan-Tao, WANG Kai, et al., Synthesis of $CH_3NH_3Sr_xPb_{(1-x)}I_3$ with less Pb content and its application in all-solid thin film solar cells. Acta Phys. Chim. Sin. 2015, **31** (2), 285-290.

[46] Zewen Xiao, Yuanyuan Zhou, Intrinsic defects in a photovoltaic perovskite variant Cs_2SnI_6, Phys. Chem. Chem. Phys. 2015, 17, 18900-18903.

[47] Byung-Wook Park, Bertrand Philippe, Bismuth based hybrid perovskites $A_3Bi_2I_9$ (*A*: Methylammonium or cesium) for solar cell application, Adv. Mater. 2015, **27**, 6806-6813.

[48] David B. Mitzi, Organic-inorganic perovskites containing trivalent metal halide layers: The templating influence of the organic cation layer, Inorg. Chem. 2000, **39** (26), 6107-6113.

[49] Ling-yi Huang and Walter R. L. Lambrecht, Electronic band structure, phonons, and exciton binding energies of halide perovskites $CsSnCl_3$, $CsSnBr_3$, and $CsSnI_3$, Phys. Rev. B 2013, **88**, 165203.

[50] Mulmudi Hemant Kumar, Sabba Dharani et al., Lead-free halide perovskite solar cells with high photocurrents realized through vacancy modulation, Adv. Mater. 2014, **26**, 7122-7127.

Chapter 2. Experimental section for sample preparation, device fabrication and measurement

The thesis was involved with the synthesis of materials from different methods, the fabrication of solar devices and the measurement of materials' optical properties, photovoltaic performance of the solar cells. Here the instruments and the methods used in the experiments are introduced as following.

2.1 Preparation of materials and fabrication of devices

2.1.1 Raw materials

All the chemicals were purchased from commercial available sources. The preparation of oxide materials was processed from high temperature furnace. The annealing were processed at tube furnace at different atmosphere.

Table 1 Reagents used in the experiments in this thesis.

	Reagent	Purity	Company
1	Zinc powder	99.99%	Sigma-aldrich
2	Hydrochloric acid	36.5%	Wako Pure Chemical Industries
3	Tetrabutyl titanate	AR	Sigma-aldrich
4	Meso-TiO_2	18NRD paste	Dyesol
5	FTO glass	glass	Opvtech
6	Ethanol	Super Dehydrated	Wako Pure Chemical Industries
7	PbI_2	98%	Tokyo Chemical Industry Co., LTD.
8	CH_3NH_3I	99%	Dyesol Co., LTD.
9	Chlorobenzene	99.9%	Sigma-aldrich
10	LiTFSI	99.99%	Macklin Co., LTD.

11	Spiro-MeOTAD	99.7%	Macklin Co., LTD.
12	4-tert-butylpyridine	AR	Sigma-aldrich
13	PEDOT:PSS	99%	Sigma-aldrich
14	Ag	99.999%	Alfa Aesar
15	Lanthanum acetate	99.9%	Alfa Aesar
16	Nickel acetate	98.0%	Wako Pure Chemical Industries
17	Manganese Acetate	99.0%	Wako Pure Chemical Industries
18	BiI_3	99.99%	Sigma-aldrich
19	2-Propanol	Super Dehydrated	Wako Pure Chemical Industries
20	N, N-dimethylformamide	Super Dehydrated	Sigma-aldrich
21	acetone	99%	Wako Pure Chemical Industries
22	Acetonitrile	Super Dehydrated	Wako Pure Chemical Industries
23	Acetic acid	99.7%	Wako Pure Chemical Industries
24	Ethylene glycol	99.5%	Wako Pure Chemical Industries
25	Titanium (IV) Tetrabutoxide monomer	95.0%	Wako Pure Chemical Industries
26	2,2'-Iminodiethanol	98.0%	Wako Pure Chemical Industries

2.1.2 Preparation of compact TiO_2 precursor and mesoporous TiO_2 layer

The compact layer was processed from the sol-gel method assisting with the spin coater [1]. First, 68 ml of titanium (IV) tetrabutoxide, 16.5 ml of 2,2'-iminodiethanol and 210 ml of super dehydrated ethanol were mixed and stirred for 1 hour for use, labeled as the solution A. Second,

3.6 ml of deionized water and 100 ml of super dehydrated ethanol was mixed together to form the solution B. Third, the solution B was slowly added into the solution accompanying with strong mixing. After that, the solution was stored and annealed in the refrigerator for 24 hour. For the preparation of compact TiO_2 layer, the annealed precursor was mixed with the super hydrated ethanol (volume ratio = 1:1), filtered using PTFE syringe filters (0.22 μm). 0.15 ml of the filtered solution was dropped on the substrates and spin coated at 3000 rpm for 30 seconds. And then the substrates were sintered at the muffle furnace at 450 ^oC for 0.5 hour, with a heating rate of 7 ^oC/min to form the TiO_2 compact layer.

The meso-TiO_2 layer was processed via spin coating method. First, the meso-TiO_2 paste was mixed with the super hydrated ethanol (weight ratio = 1:3.5). Second, the mixture was milled with beads for 4 hours to obtain a homogenous suspension. Third, 0.2 ml of the suspension was loaded at the substrates and spin coated at 5000 rpm for 30 seconds. After that, the substrates were sintered at the muffle furnace at 500 ^oC for 0.5 hour, with a heating rate of 8 ^oC/min to form the mesoporous TiO_2 layer.

Table 2. Instruments used in the experiments in this thesis.

Series	Apparatus	MODEL	Company
1	Muffle Furnace	FO300	Yamato Scientific Co., Ltd., Japan
2	Spin coater	SC-150	Oshigane Co., Ltd., Japan
3	Hot plate	C-MAG HS7	IKA Co., Ltd., Germany
4	Ohmmeter	FULL-TECH FT-101	FULL-TECH Co., Ltd., Japan
5	Digital meter	Keithley 2400	Teltronix, INC. Co., Ltd., USA
6	Solar simulator	CEP-2000	Bunkou Keiki Co., Ltd., Japan
7	Standard solar cell	BS-520BK	Bunkou Keiki Co., Ltd., Japan
8	Standard solar cell	BS-500BK	Bunkoukeiki Co., Ltd., Japan
9	Energy dispersive X-ray spectrometry	Genesis XM2	EDAX Co., Ltd., Japan
10	X-ray diffractometer	Rigaku	Rigaku Co., Ltd, Japan
11	Scanning electron microscope	JCM-6000	JEOL Co., Ltd, Japan

12	UV-visible spectrometer	V-670	JASSCO Co. Ltd., USA
13	ionization energy measuring device	KV205-HK	Bunkoukeiki Co., Ltd, Japan
14	X-ray photoelectron spectroscopy	AXIS-HS	KRATOS Co., Ltd., Japan
15	Tube Furnace	ARF-30KC	ASAHI RIKA Co., Ltd., Japan
16	Field emission-scanning electron microscope	S5200	Hitachi Co., Ltd., Japan

2.1.3 General Procedure of perovskite oxide materials synthesis

The preparation of La_2NiMnO_6 is referred to Pechini method [2]. The Stoichiometric precursors were mixed in citric acid/ ethylene glycol solution. And the solutions were stirred at 120 ^oC to form a dry gel. After that, the gel was pyrolized at 400 ^oC for 5 hours to form homogenous oxide powders. And then the powders were synthesized or annealed at different temperatures or atmospheres. The general procedure of preparation is illustrated in Fig. 1.

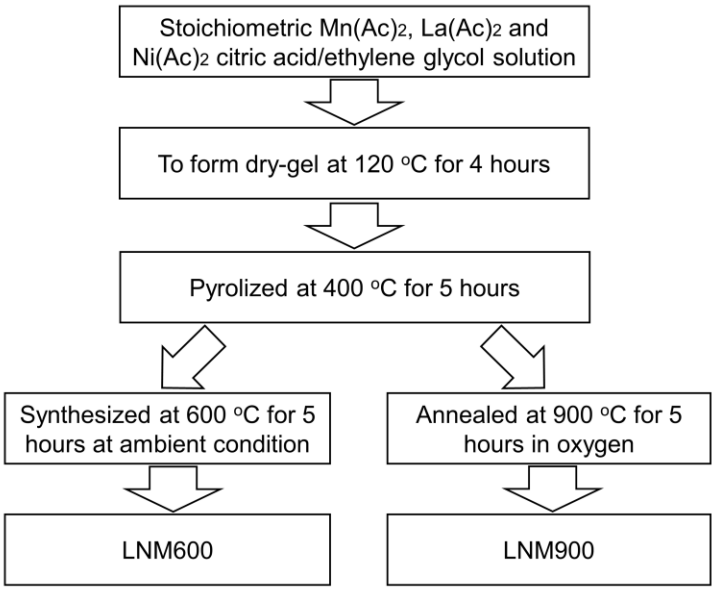

Fig. 1. Schematic of the general procedure to synthesize La_2NiMnO_6.

2.2 Characterization

2.2.1 UV-vis Spectroscopy

The UV-vis spectroscopy was performed by the spectrometer (V-670, JASSCO) using the deuterium light source and tungsten light source to investigate the optical properties of the materials. Regarding the thin films for measurement, the spectral were applied from the wavelength from 300 to 800 nm by the absorbance and the transmittance. The band gap of thin films was determined by the absorbance using Tauc Plot as following [3].

$$\alpha h\gamma = \beta(h\gamma - E_g)^n \quad (1)$$

where the α is the absorption coefficient, $h\gamma$ is the photon energy and E_g is the band gap. When the materials measured are indirect band gap semiconductors, n is equal to ½. When the materials measured are direct band gap semiconductors, n is equal to 2. Transmittance can be defined as the ration of the transmitted intensity to the input light intensity, which is related the optical performance, coverage and thickness. Reflectance is defined as the logarithm of the transmittance. Regarding the measurement of the perovskite oxide powders, the spectrometer was integrated with an integrator by using reflectance.

$$\text{Transmittance} = I_t/I_o \quad (3)$$

$$\text{Absorbance} = \log[1/ I_t/I_o] \quad (4)$$

where the I_t is the intensity of transmittance light, I_o is the intensity of output light. According the Beer Lambert's law [4],

Absorbance (A) = absorption coefficient (α) * path length (L)* sample concentration (c).

2.2.2 Photovoltaic performance measurement

The photovoltaic performance of the solar cells was mainly evaluated by the *I-V* curves measured by the solar simulator. As shown in Fig. 2, the *I-V* curves measurement of solar cells includes the voltage of open circuit (V_{oc}), Current of Short Circuit (J_{sc}), Fill Factor (*FF*), Power Conversion Efficiency (*PCE*). I_{max} and V_{max} represent the current and the voltage at maximum output, respectively. The *FF* and *PCE* can be defined as the following.

$$FF = \frac{Imax \times Vmax}{Jsc \times Voc} \quad (5)$$

$$PCE = \frac{Jsc \times Voc \times FF}{Pin} \quad (6)$$

where Pin is the power of incident light. Generally speaking, the standard AM1.5G incident light is used for measurement. The power of the AM1.5G incident light is 100 mW/cm^2, and its energy distribution in visible light region is shown in Fig. 3. For all the devices measurement, the scanning speed for all the samples was 0.01V/s. The forward scanning from 0 to 1 V and the backward scanning from 1 to 0 V have been applied to evaluate the hysteresis phenomenon of the solar devices.

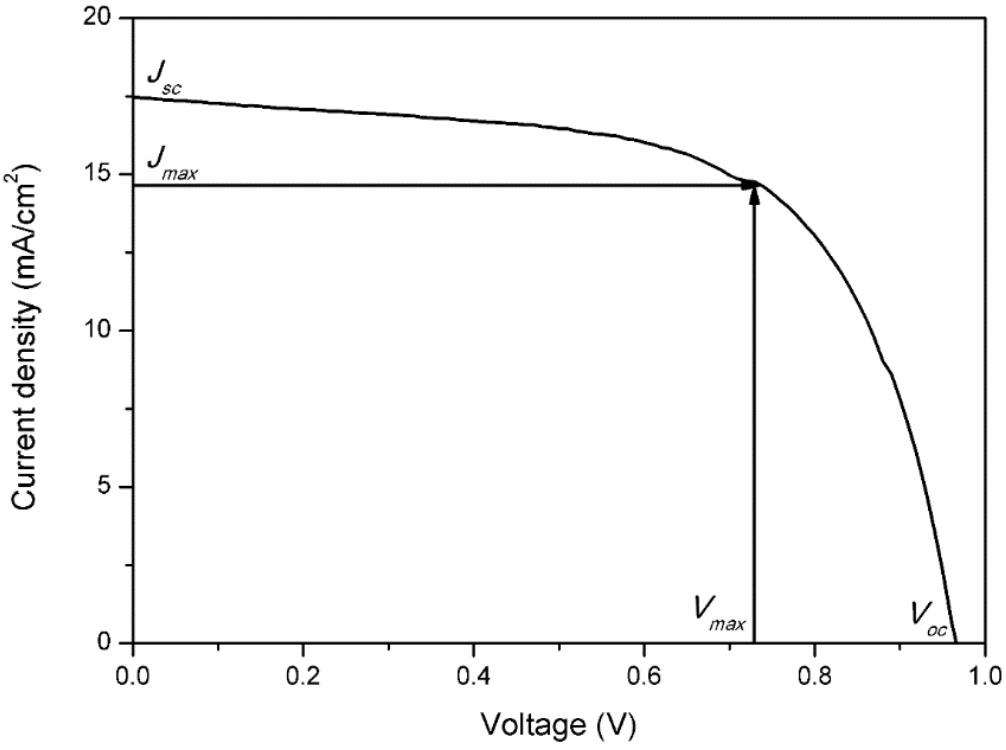

Fig. 2. a typical *I-V* curve of the solar cells.

The dark current is useful to determine the leakage current in solar cells. It was measured to evaluate the photovoltaic performance of solar cells in dark box without light illumination.

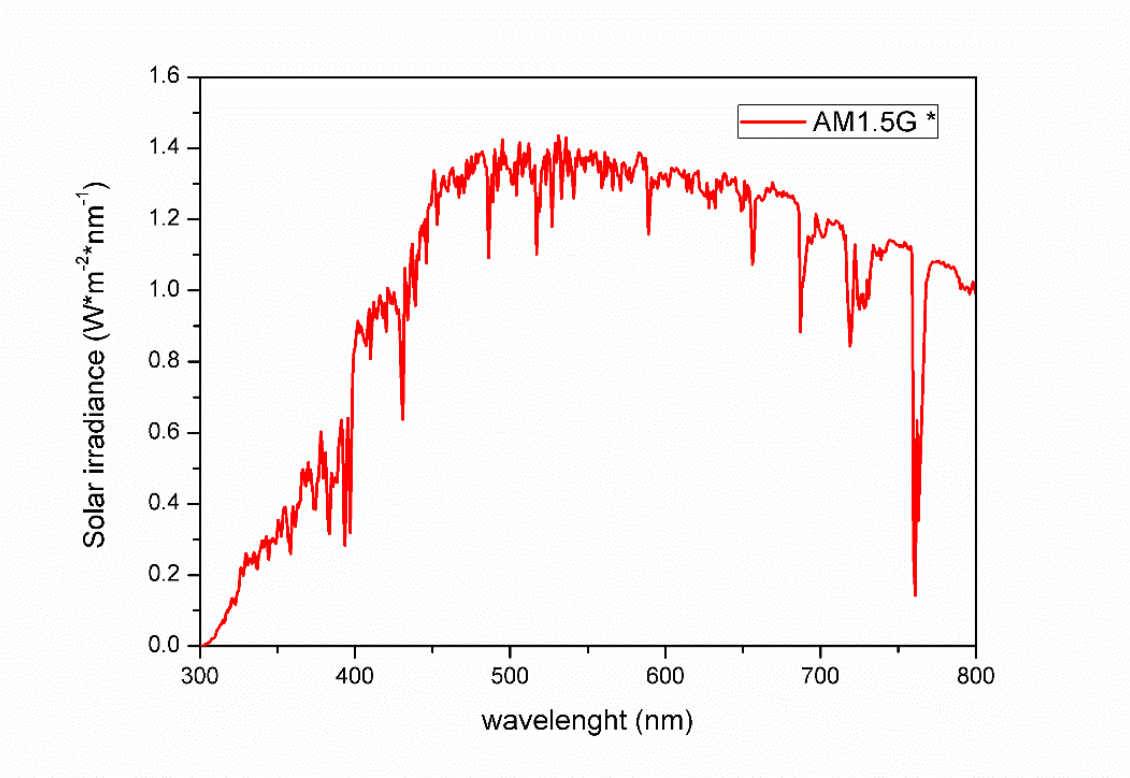

Fig. 3. Energy distribution of the standard AM1.5G light [5].

Reference

[1] Huawei Zhou, Yantao Shi, Qingshun Dong, Hong Zhang, Yujin Xing, Kai Wang, Yi Du, and Tingli Ma, Hole-conductor-free, metal-electrode-free $TiO_2/CH_3NH_3PbI_3$ heterojunction solar cells based on a low-temperature carbon electrode. J. Phys. Chem. Lett. 2014, **5**, 3241−3246.

[2] R.I. Dass, J.Q. Yan, and J.B. Goodenough, Oxygen stoichiometry, ferromagnetism, and transport properties of $La_{2-x}NiMnO_{6+\delta}$, Phys. Rev. B 2003, **68**, 64415.

[3] J. Tauc, R. Grigorovici, A. Vancu, Optical properties and electronic structure of amorphous germanium, Phys. Stat. Sol. B 1966, **15**, 627-637.

[4] Houghton, J.T. The Physics of Atmospheres 2nd ed. 2002, Chapter 2.

[5] NREL chart, http://rredc.nrel.gov/solar/spectra/am1.5/.

Chapter 3. Concentration gradient controlled growth of large-grain $CH_3NH_3PbI_3$ films and enhanced photovoltaic performance of solar cells in ambient conditions

3.1 Introduction

In the past six years, halide perovskite solar cells have attracted much attention. They showed the power conversion efficiency (*PCE*) rapidly improved from 3.8% to 22.1%, making them a great potential for commercial applications [1-4]. It was reported that the performance of the perovskite solar cells, e.g. the hysteresis, stability and power conversion efficiency, was strongly affected by the quality of the perovskite films [4-10]. During the fabrication of the halide perovskite solar cells, the grain size, grain boundary and film coverage strongly affected the quality of perovskite films. For instance, the large grain size and fewer grain boundaries reduced the recombination centers as well as series resistances of devices, which benefited the separation of photo-excited electron-hole pairs [6-9]. Meanwhile, a full coverage of the perovskite films reduced the leakage currents and improved the stability of the devices [10,11]. Therefore, the preparation of the high-quality perovskite films with large grains and a full coverage is an important topic.

Previous reports indicated that during the formation of perovskite films between PbI_2 films and CH_3NH_3I (MAI) solutions, the concentration of MAI solutions deeply influenced the microstructures of the perovskite films [6,12,13]. High concentration CH_3NH_3I solutions created a large amount of nucleation centers but the small grains of nano-scales. Whereas, low concentration CH_3NH_3I solutions benefited the growth up of the large perovskite grains but worse coverage. Therefore, it was too difficult to balance the MAI concentrations for high-performance perovskite solar cells. In this case, we tried to develop a new method to prepare high-quality perovskite films. According to the theory of crystal nucleation and growth, a method of two-step concentration gradient controlled reactions were invented to control the growth of perovskite films in high humidity conditions. The high-quality $CH_3NH_3PbI_3$ perovskite films with large grains and full coverage have been achieved, and enhanced photovoltaic performance

was observed in the corresponding perovskite solar cells.

3.2 Experimental

3.2.1 Preparation of $CH_3NH_3PbI_3$ perovskite films

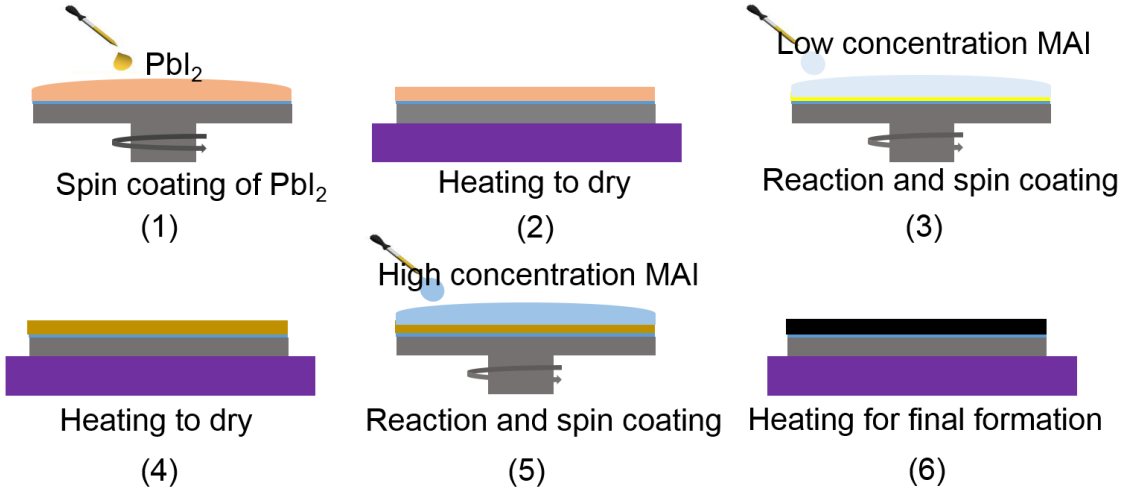

Fig. 1. Schematic illustration of the procedures for the formation of perovskite film via the two-step concentration gradient growth.

462 mg of PbI_2 was dissolved in 1 mL of N, N-dimethylformamide, heated at 70 °C and filtered using PTFE syringe filters (0.22 μm) before further processed. MAI was dissolved in the dehydrated isopropanol solvent (6, 10, 20, 30 mg/ml). Fig. 1 showed the detailed preparing procedures via the two-step concentration gradient controlled reactions. First, 0.2 ml of the PbI_2 solution was dropped on 2.5 cm × 2.5 cm regular glass substrates covered with mesoporous TiO_2, and spin coated at a speed of 3000 rpm for 5 seconds and 6000 rpm for 5 seconds. Second, the PbI_2 films were annealed at 100 °C for 10 minutes under ambient conditions. Third, 0.5 ml of the MAI solution (6 mg/ml) was dropped on the PbI_2 films and loaded respectively for different times (10, 20, 40, 60 seconds) for the first-step growth of the perovskite films, and then spin coated at 3000 rpm for 20 seconds for drying. Forth, the films were heated at 100 °C for 10 minutes for drying. Fifth, 0.5 ml of the high concentration MAI solutions (10, 20, 30 mg/ml) were dropped respectively on the films and loaded for 50 seconds, spin coated for drying at 3000

rpm for 20 seconds for the second-step growth of $CH_3NH_3PbI_3$ films. Finally, the films were annealed at 100 ^oC for 10 minutes. To make a comparison, the perovskite films of xm-60s (x = 6, 7, 8, 10, 20, 30) were also prepared from the traditional single solution method. The detailed procedures are shown in Fig. 2. The detailed parameters of the experiments are shown in Table 1, Table 2 and Table 3. All the processes were carried out at the ambient conditions with the humidity of ca. 60%.

Table 1. Parameters for the MAI concentrations effect on the one-step growth of perovskite films (xm-60s).

Label	Solution (mg/ml)	Loading time (second)
6m-60s	6	60
7m-60s	7	60
8m-60s	8	60
10m-60s	10	60
20m-60s	20	60
30m-60s	30	60

Table 2. Parameters for the MAI concentration effect on the concentration gradient controlled growth of perovskite films (6m-60s-xm-50s).

Label	Solution1 (mg/ml)	Loading time (second)	Solution2 (mg/ml)	Loading time (second)
6m-60s	6	60	-	-
6m-60s-10m-50s	6	60	10	50
6m-60s-20m-50s	6	60	20	50
6m-60s-30m-50s	6	60	30	50

Table 3. Parameters for the MAI loading time effect on the concentration gradient controlled growth of perovskite films (6m-xs-30m-50s).

Label	Solution1 (mg/ml)	Loading time (second)	Solution2 (mg/ml)	Loading time (second)
6m-60s	6	60	-	-
6m-10s-30m-50s	6	10	30	50

6m-20s-30m-50s	6	20	30	50
6m-30s-30m-50s	6	30	30	50
6m-60s-30m-50s	6	60	30	50

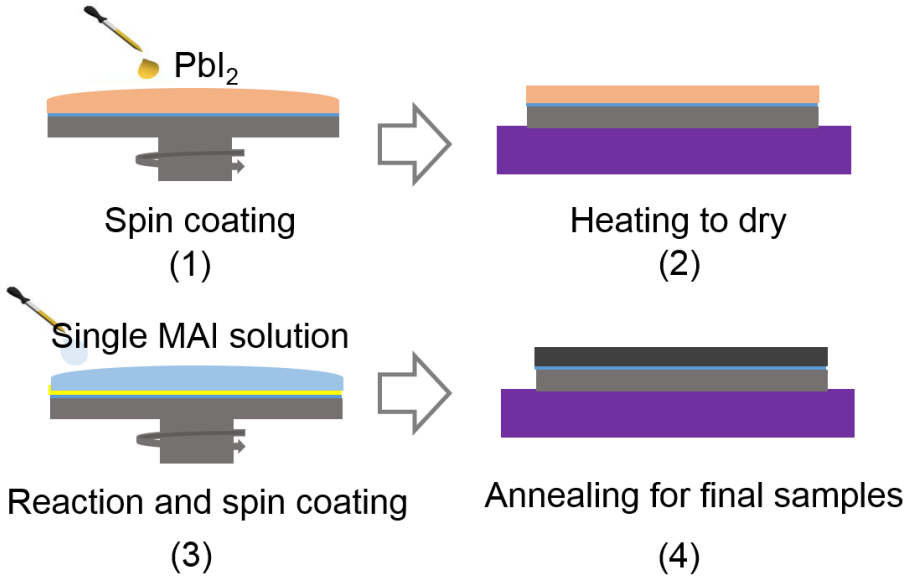

Fig. 2. Schematic illustration of the procedures for the formation of perovskite film via the traditional single solution growth

3.2.2 Fabrication of devices

The perovskite solar cells were fabricated in an architecture of FTO/compact-TiO_2/mesoprous-TiO_2+absorber /HTM/Au. FTO glass substrates were etched with 2 M HCl and zinc powder, washed with IPA, acetone and clean water, and dried for use. And then the FTO substrates were treated by the ultraviolet light-induced ozone. A TiO_2 precursor was prepared as reported in Ref. [19]. It was dropped on the FTO glass, spin coated at 3000 rpm for 30 seconds, and then sintered at 450 ^oC for 1 hour to form a compact TiO_2 layer. The mesoporous TiO_2 gel was spin coated on the compact TiO_2 layer at 5000 rpm for 30 seconds, and then sintered at 500 ^oC for 30 minutes. When the substrates were cooled down, the perovskite films were prepared on them as described above. 72.3 mg of spiro-OMeTAD, 28.8 μL of 4-tert-butylpyridine, 20 μL of a stock solution of 300 $mg \cdot mL^{-1}$ cobalt TFSI acetonitrile solution and 17.5 μL of 520 $mg \cdot mL^{-1}$ lithium bis-(trifluoromethyl sulphonyl) imide in acetonitrile were dissolved in 1 mL of chlorobenzene as the hole transport material, and then spin coated on the perovskite layers at

3000 rpm for 30 seconds. Finally, 30 nm of gold was evaporated on the samples to form an electrode. The whole processes of the fabrication were carried out in ambient conditions with the humidity of ca. 75%.

3.2.3 Characterization

The X-ray diffracting patterns were recorded from 10 ° to 40 ° at a scanning speed of 0.01 °/s using a X-ray diffractometer (XRD, RINT2100, Rigaku) with Cu *Kα* radiation (λ = 1. 54056 Å). The microstructures and surface morphologies of the perovskite films were determined be the scanning electron microscope (SEM, JCM-6000, JEOL). The cross-section images of the perovskite films were measured by the field-emission scanning electron microscope (FE-SEM, S5200, Hitachi). The optical properties of the perovskite films were characterized using a UV-Vis-NIR spectrophotometer (V-670, JASSCO) by the spectral absorption and transmittance from 300-800 nm.

The *I-V* characteristics of the perovskite solar devices were measured by a solar simulator (CEP-2000, Bunko Keiki). It was interfaced with a xenon lamp (Bunko Keiki BSOX150LC) at 100 mW/cm^2 under AM 1.5G conditions. In order to avoid discrepancy between the calibrated diode and the measured devices, an amorphous Si photodetector (Bunko Keiki BS-520 S/N 353) was used to fix the power of the light exposure from the solar simulator. A 0.12 cm^2 black metal mask was used to control the cell area for the measurement of the photovoltaic performance of the devices.

3.3 Results and discussion

3.3.1 Single solution growth of $CH_3NH_3PbI_3$ films

First, the perovskite films were prepared from the one-step reaction method. Fig. 3 showed the XRD patterns of the samples prepared via one-step reaction from different MAI solutions (6, 7, 8, 10, 20, 30 mg/ml) for 60 seconds. It can be clearly seen that there were some peaks of the PbI_2 residue, demonstrating the incomplete reaction in all of the as-prepared samples. Fig. 4 showed the SEM images of the surface morphologies of the samples. The sample prepared from 6 mg/ml solution showed the largest grain size up to 1.5 μm. However, the films haven't been well covered. As the concentration of the MAI solutions increased, the grain sizes of perovskite

films decreased as well as the improved coverage. Particularly, when the MAI concentration was higher than 10 mg/ml, the perovskite films became nano-scaled with huge amount of grain boundaries. As mentioned above, none of these films were qualified enough for high performance solar cells.

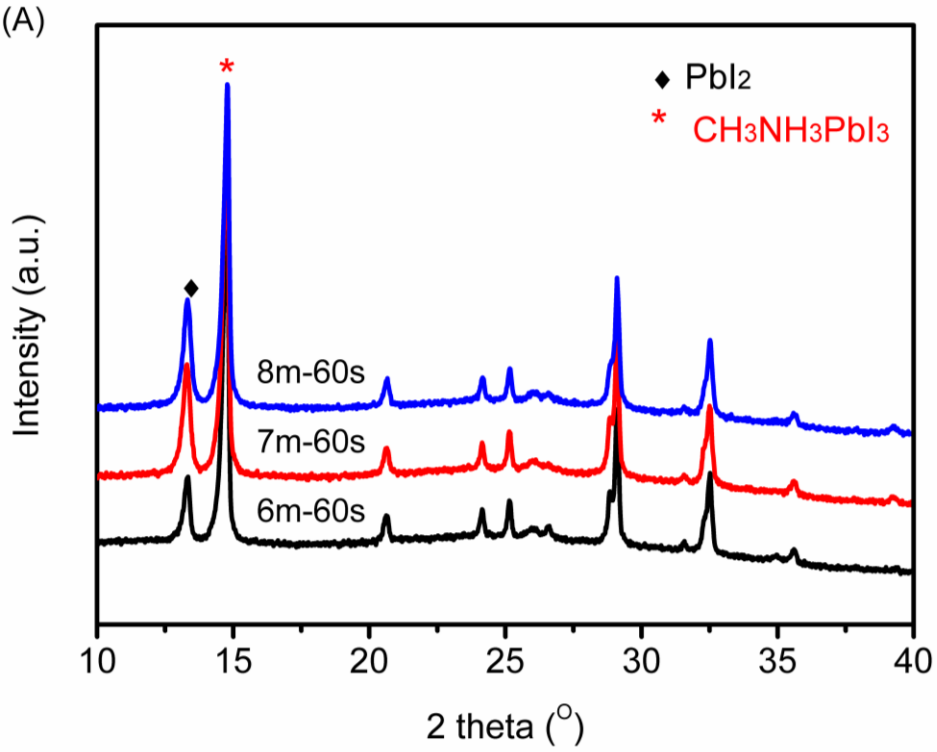

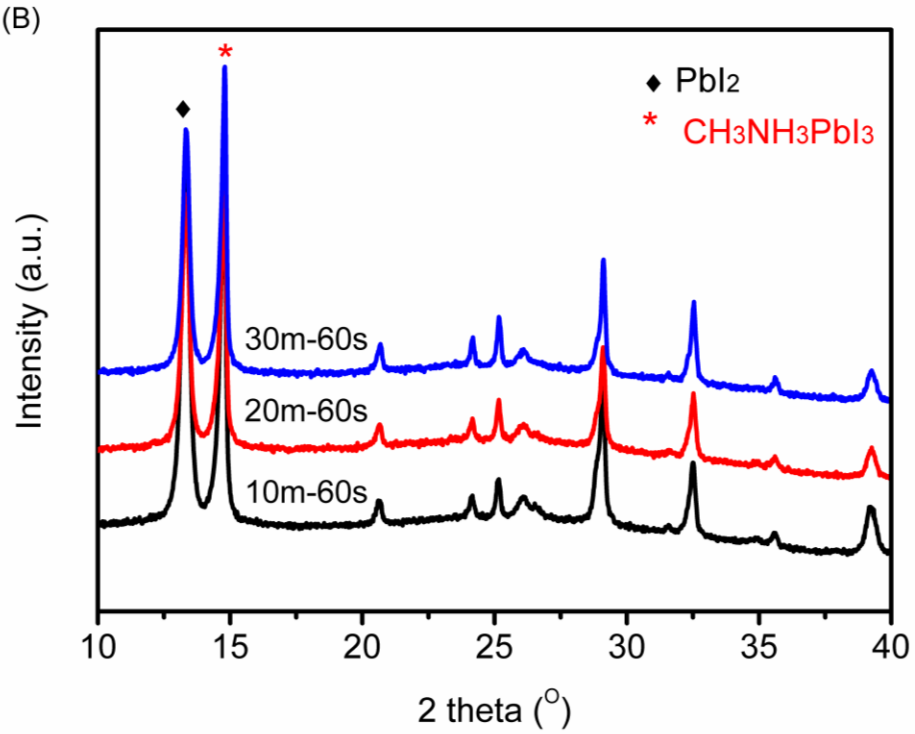

Fig. 3. XRD patterns of the samples of xm-60s. (A) x = 6, 7, 8. (B) x = 10, 20, 30).

The formation of perovskite films was very sensitive to the concentration of the MAI solutions. During the formation of the perovskite films, because the lower concentration MAI solutions created less interfacial free energy between the solid and the solution, only a few nucleation centers could occur at the PbI_2 films [12,13]. After that, they performed as the perovskite seeds and grown up to the bigger grains. However, the other parts of the PbI_2 films could not nucleate due to the low interfacial free energy. Particularly, as the reaction went on, the concentration of the MAI solution decreased, which made the PbI_2 residue more difficult to nucleate. Therefore, for the samples prepared from the low centration MAI solutions, the PbI_2 residue mainly existed at the spaces between the perovskite grains. In the contrary, as the MAI concentration increased, the interfacial free energy increased, more and more perovskite seeds formed immediately at the surface of the PbI_2 films when the MAI solutions were loaded [6]. These seeds competed with each other and suppressed the growth up of the grains, resulting in smaller grain sizes to 200-300 nm. The small grains created dense perovskite films on the surface, simultaneously prohibiting the further reaction between the PbI_2 films and the MAI solutions [12]. Accordingly, the PbI_2 residue remained under the perovskites films in these

samples via the high concentration MAI solutions.

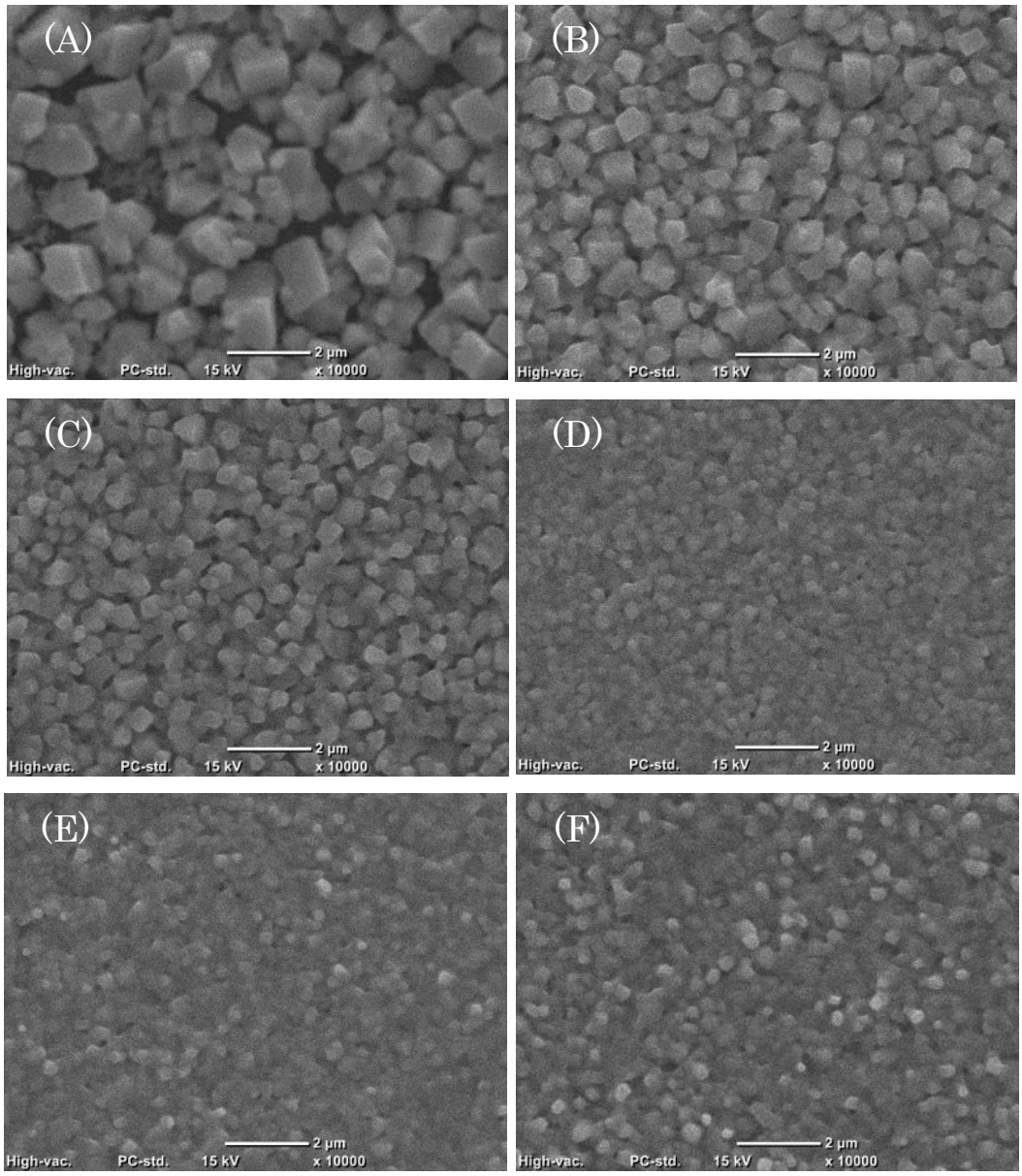

Fig. 4. SEM images of the surface morphology of the samples of xm-60s. (A) x = 6. (B) x = 7. (C) x = 8. (D) x = 10. (E) x = 20. (F) x = 30.

3.3.2 Concentration gradient controlled Growth of $CH_3NH_3PbI_3$ films

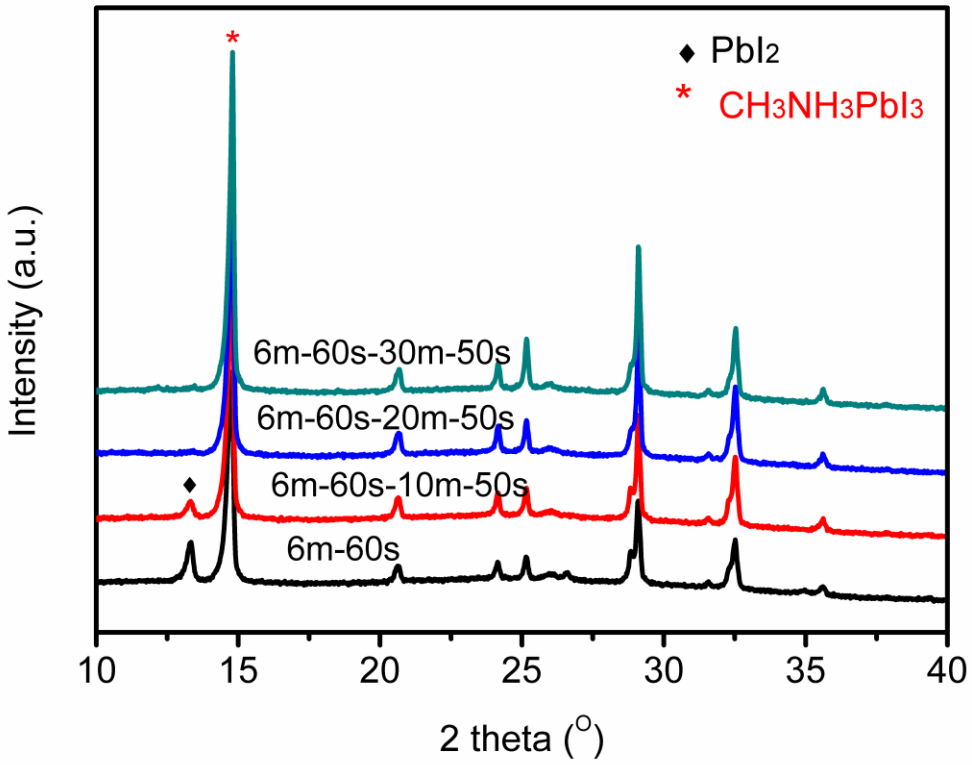

Fig. 5. Comparison of the XRD patterns of the samples of 6m-60s-xm-50s (x = 0, 10, 20, 30).

In order to overcome the disadvantages of the traditional single solution method, a method of two-step MAI concentration gradient controlled reactions was developed to prepare $CH_3NH_3PbI_3$ perovskite films. Based on the experimental results above, the low concentration MAI solution (6 mg/ml) was used to grow large grains at the first-step reaction. More detailed parameters can be seen in Table 2. First, the PbI_2 films were reacted with the 6 mg/ml MAI solution for 60 seconds, and then they were treated by the higher concentration MAI solutions (10, 20, 30 mg/ml) for 50 seconds to investigate the concentration effect. Fig. 5 showed the XRD patterns of the samples. Huge amount of PbI_2 residue still existed in the sample of 6m-60s. However, after the treatment of the higher concentration MAI solution (10 mg/ml), the peaks of PbI_2 residue were weakened. And as the concentration of the MAI solutions increased, the peaks of the PbI_2 residue disappeared. The samples of 6m-60s-20m-50s and 6m-60s-30m-50s were well crystalized with the $CH_3NH_3PbI_3$ perovskites with little PbI_2 residue.

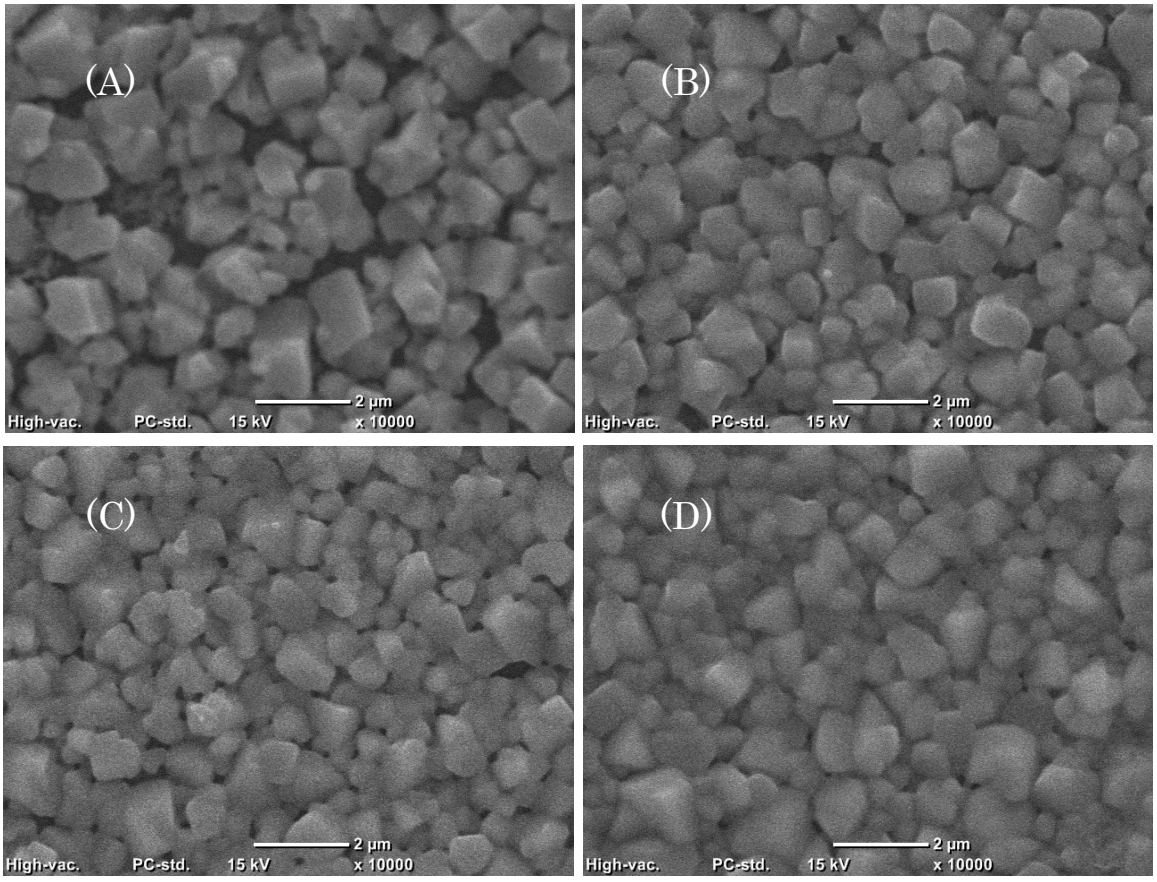

Fig. 6. SEM images of the surface morphology of the samples of 6m-60s-xm-50s. (A) x = 0. (B) x = 10. (C) x = 20. (D) x = 30.

The SEM images of the surface morphologies of the films were shown in Fig. 6. A gradual change of the surface morphologies of the films occurred as the increase of the MAI concentrations. The sample of 6m-60s showed large perovskite grains with many spaces between them. However, as the concentration of the MAI solutions increased at the second-step reaction, the spaces between the grains were gradually narrowed and reduced as well as the coverage of the perovskite films was improved. Particularly, the sample of 6m-60s-30m-50 showed a full perovskite coverage on the substrates, with the grain size up to 1.4 µm. It is reported that the oxygen at TiO_2-perovskite interfaces attributed to the degradation of $CH_3NH_3PbI_3$ perovskite films [11]. Therefore, the improved coverage could favor the prevention of TiO_2-perovskite interfaces from oxygen and improve the stability of perovskite films.

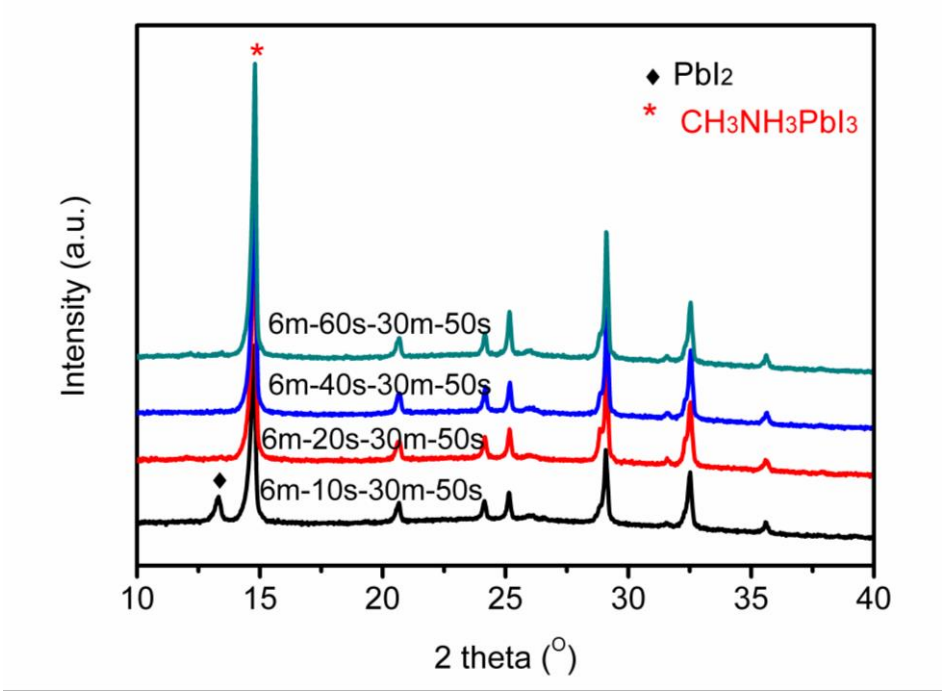

Fig. 7. Comparison of the XRD patterns of the samples of 6m-xs-30m-50s (x = 10, 20, 40, 60).

Second, the MAI loading time effect in the first-step reaction on the perovskite formation was investigated. As shown in Table 3, the PbI_2 films were treated by 6 mg/ml MAI solutions for different seconds, and then they were treated by 30 mg/ml MAI solutions for 50 seconds. Fig. 7 showed the XRD patterns of the as-prepared samples. It revealed that, expect the sample 6m-10s-30m-50s, all the other samples were well crystalized with little PbI_2 residue. The SEM images of the surface morphologies of the samples were showed in Fig. 8. The sample 6m-10s-30m-50s mainly consisted of the dispersed nano-grains with some big particles. As the loading time increased at the first-step reaction, the grain size of the perovskite films sharply increased to 1.5 μm, as well as a full coverage on the surfaces.

The detailed statistic information of grain size distribution can be seen in Fig. S1 and Table 4. The sample of 6m-60s-30m-50s exhibited a continuous distribution of the grain size, which can benefit a full coverage. In contrast, the grain sizes of the samples of 6m-20s-30m-50s, the 6m-60s-10m-50s and 6m-10s-30m-50s exhibited a relative centralized distribution.

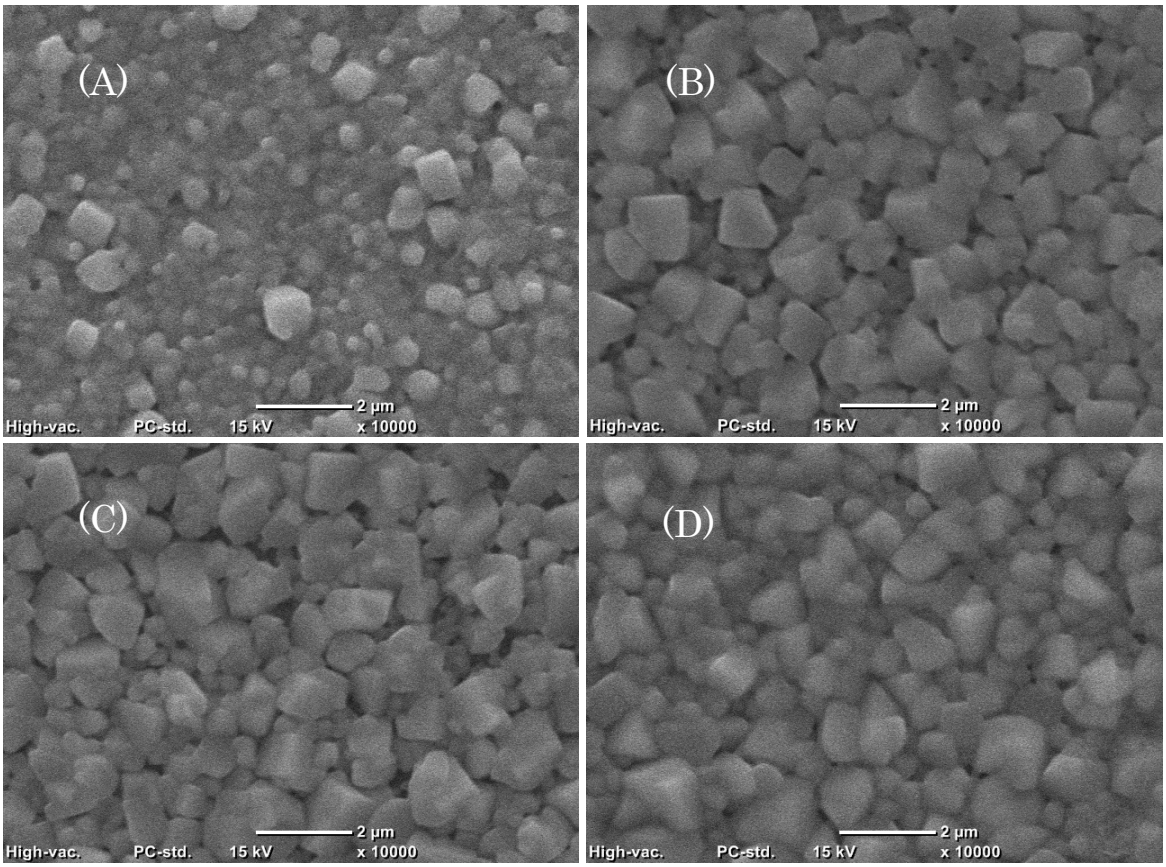

Fig. 8. SEM images of the surface morphology of the samples of 6m-xs-30m-50s. (A) x = 10. (B) x = 20. (C) x = 40. (D) x = 60.

Table 4. Statistical analysis on the grain size distribution of the perovskite films.

	Max./nm	Min./nm	Mean/nm
6m-60s	1980.21	585.44	1171.23
6m-60s-10m-50s	2438.82	594.53	1377.54
6m-60s-20m-50s	2057.82	617.07	1315.23
6m-60s-30m-50s	2461.41	713.67	1467.93
6m-10s-30m-50s	728.63	137.89	313.72
6m-20s-30m-50s	2359.29	617.39	1367.48
6m-40s-30m-50s	2607.01	607.13	1339.04

3.3.3 UV-visible absorption behaviors

Fig. 9 showed the UV-visible absorption behaviors of the films from the traditional single MAI solutions. All the samples possessed the same absorption threshold, indicating that the

bandgaps of the samples remained the same. However, the absorption strength of the samples are different from each other in different regions. For the film 6m-60s prepared from the traditional single MAI solution, it showed an absorption without strong peaks. As the concentration of the MAI solutions increased, the spectral absorption were enhanced in the short wavelength region (350-500 nm) as well as the reduced absorption in the long-wavelength region (600-750 nm).

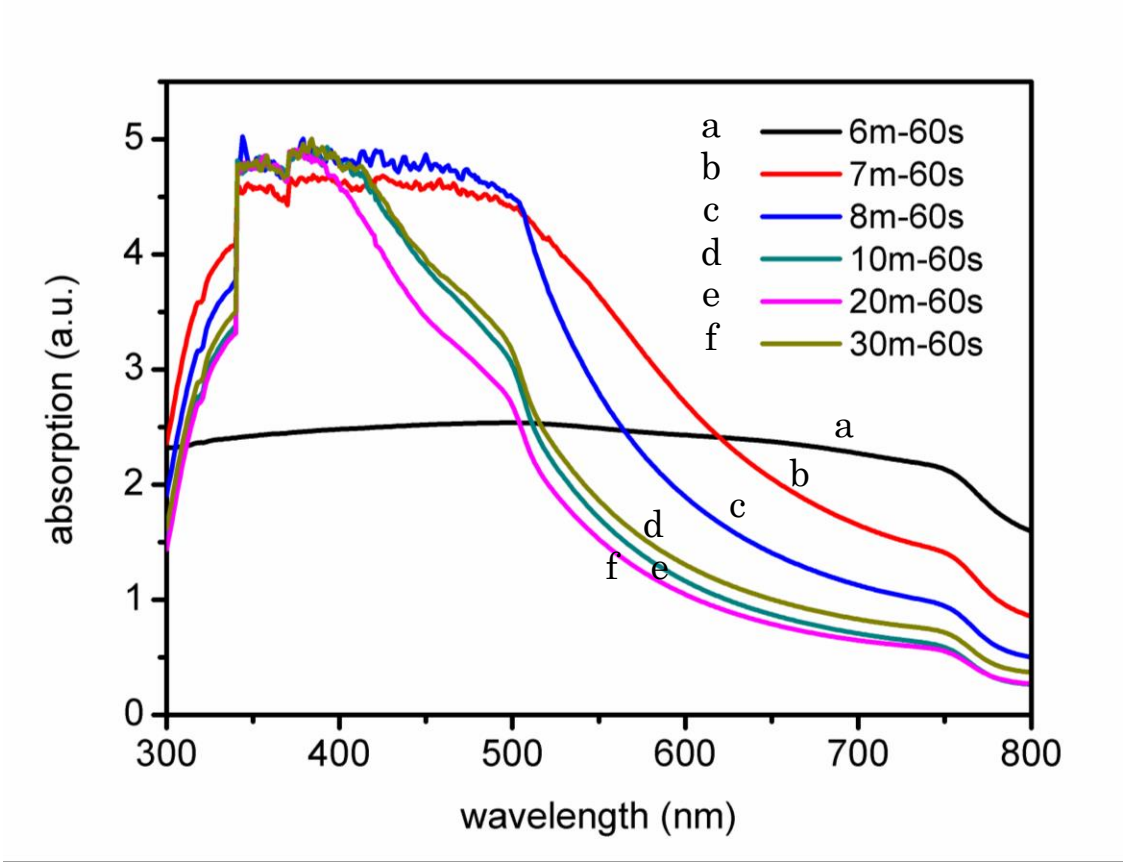

Fig. 9. UV-visible absorption of the samples via single solution method.

The spectral absorptions of the samples prepared via the concentration gradient controlled growth are showed in Fig. 10. Fig. 10(a) presented the spectral absorption of the samples prepared from different MAI concentrations. After the treatment of the high concentration MAI solutions, all the perovskite films demonstrated the enhanced absorption compared with 6m-60s. Particularly, the absorption was improved in the short-wavelength region. Additionally, the sample 6m-60s-10m-50s also showed a little enhancement in the long wavelength region. Regarding the loading time effect on the absorption of perovskite films, as shown in Fig. 10(b),

the sample of 6m-10s-30m-50s showed its major absorption located at the wavelength from 350 to 500 nm, as well as with a lower absorption than 6m-60s in the long wavelength region. In contrast, when the MAI loading time was higher than 20 seconds, the absorption of the samples of 6m-xs-30m-50s (x = 20, 40, 60) became higher than that of 6m-60s, broadened up to the short wavelength of ca. 350 nm.

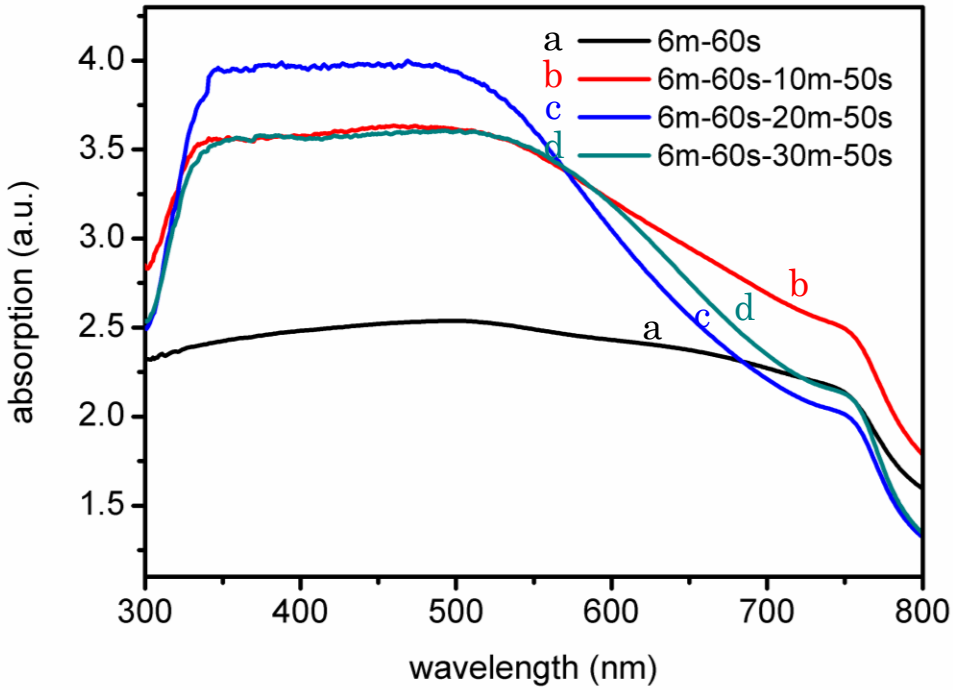

Fig. 10(a). UV-visible spectral absorption of the samples 6m-60s-xm-50s (x = 0, 10, 20, 30) via the concentration gradient controlled method.

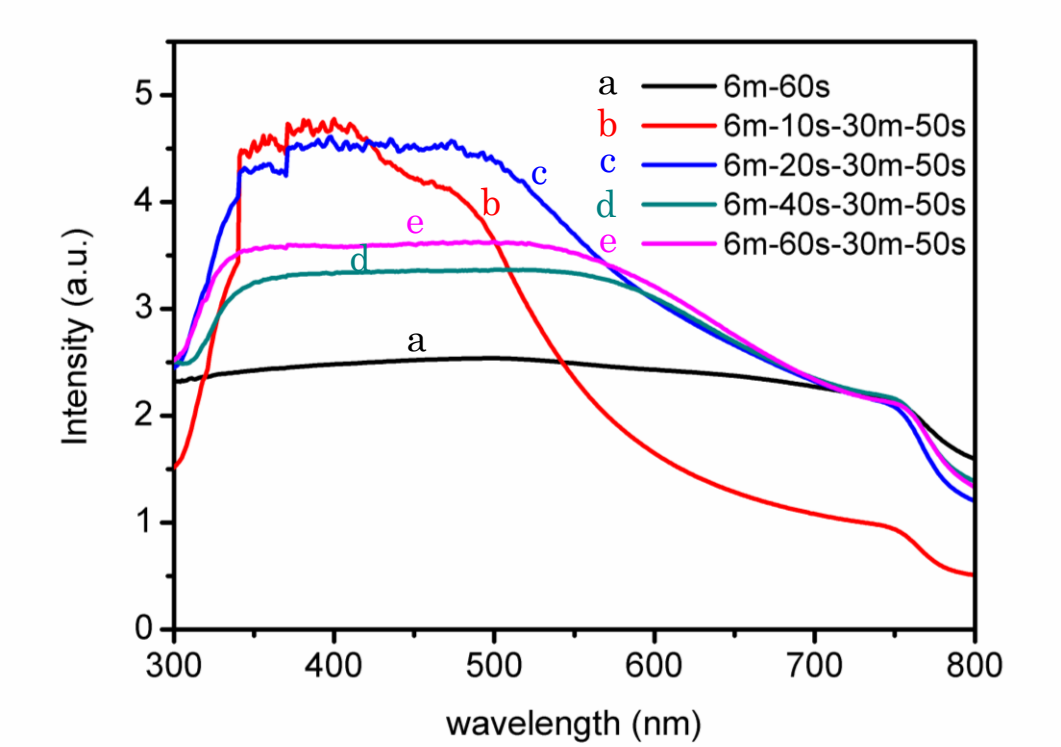

Fig. 10(b). UV-visible spectral absorption of the samples 6m-xs-30m-50s (x = 10, 20, 40, 60) via the concentration gradient controlled method.

The thickness of the films can be an important factor for spectral absorption. In order to evaluate the thickness effect, the cross-section FE-SEM images of the films (6m-60s, 6m-10s-30m-50s, 6m-60s-10m-50s, 6m-60s-30m-50s.) were shown in Fig. 11. The results indicated that all the thickness of the films are almost the same, ca, 450 ± 20nm. Therefore, the difference on spectral absorption is more likely to depend on the microstructures and surface morphologies of the films.

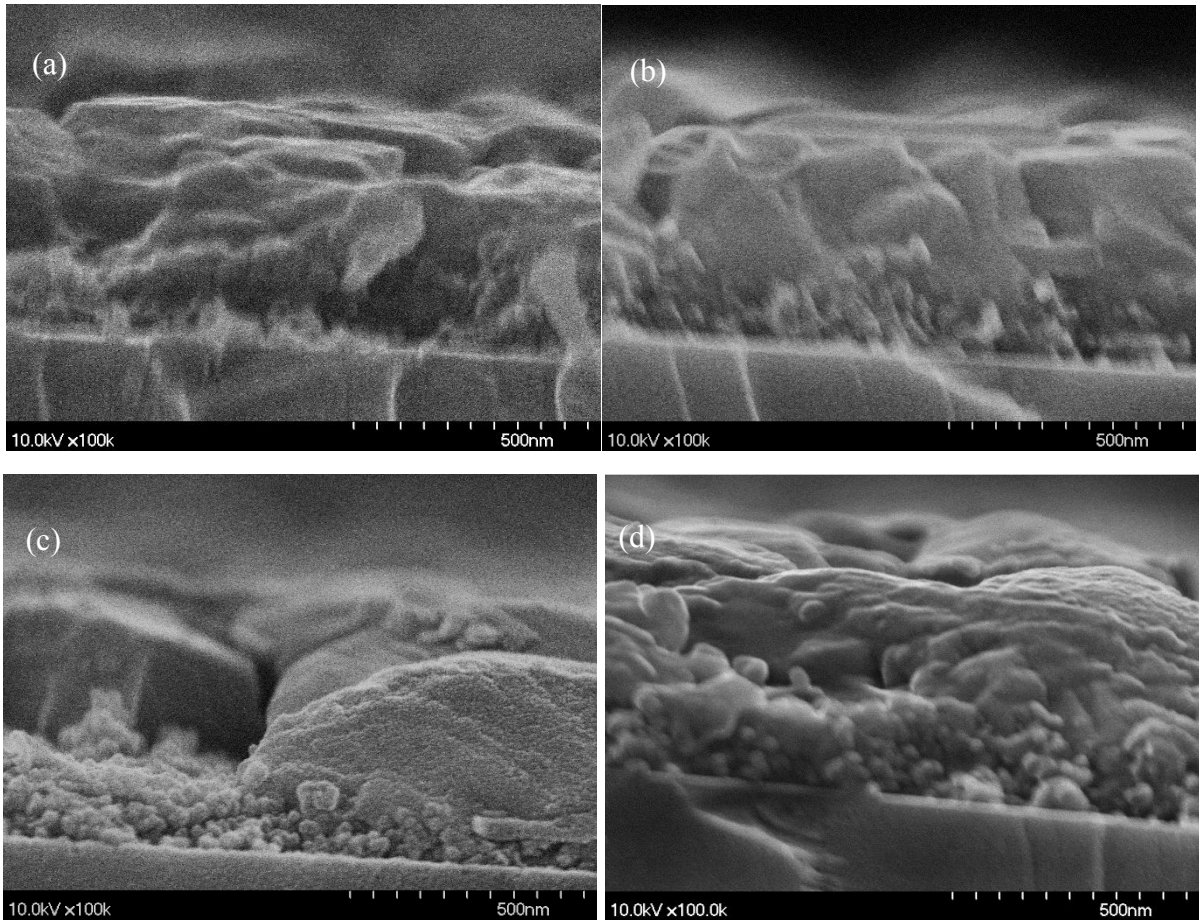

Fig. 11. Cross-section SEM images of the sample. a) 6m-60s, b) 6m-10s-30m-50s, c) 6m-60s-10m-50s, d) 6m-60s-30m-50s.

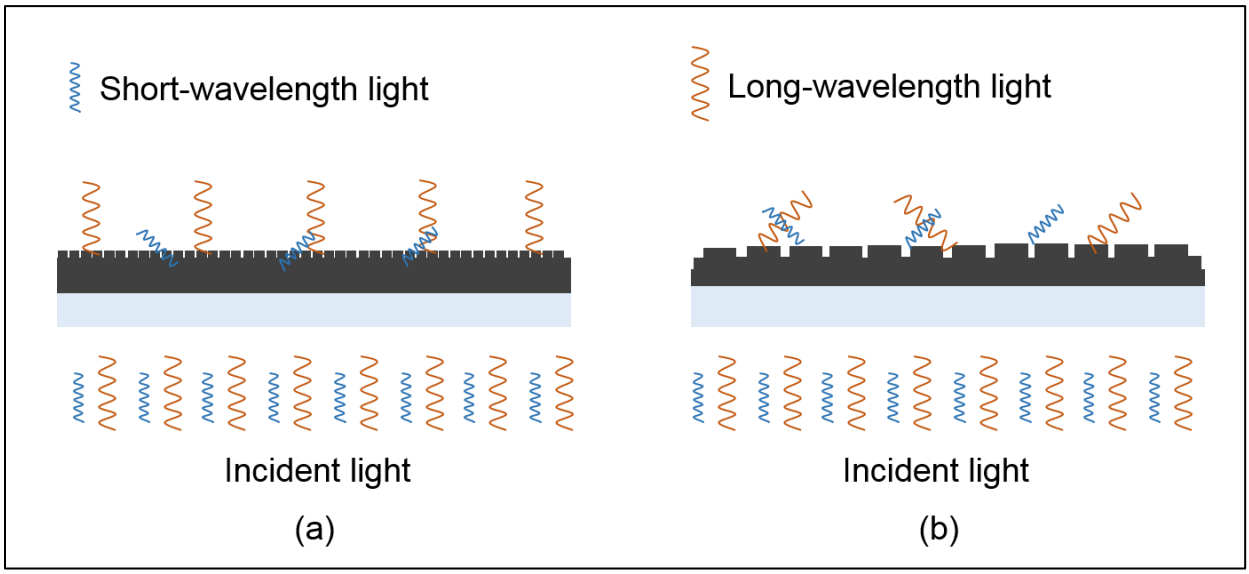

Fig. 12. Schematic illustration of grain-size-dependent Mie Scattering on the perovskite films.

The absorption strength of the perovskite films were sensitive to the particle sizes, and Mie scattering theory can be applied to explain this phenomenon. According to the Mie scattering theory, the scattering behavior of the incident light strongly depended on the particle sizes of the medium, which affected the absorption [14, 15]. When the wavelength of the incident light was comparable with the particle size, the scattering would be enhanced [14-16]. Therefore, as shown in Fig. 12(a), small perovskite grains can favor the scattering in the short-wavelength region, whereas, large perovskite grains can favor the scattering in the long-wavelength. For the samples of 6m-60s prepared via the one-step reaction, it mainly consisted of large perovskite grains with few nano-grains. Accordingly, it might have a strong scattering in the long-wavelength region. Since there were few nano-grains, the scattering in the short-wavelength could almost be ignored. However, the absorption from the contribution of PbI_2 residue can be ignored in our discussion because there was just a little PbI_2 residue in the film 6m-60s. Regarding the perovskite films prepared from the two-step concentration gradient reactions, the light scattering of the samples strongly depended on the MAI loading time in the first-step reaction and the MAI concentration in the second-step reaction. With the treatment of the higher concentration MAI solutions, small perovskite grains formed in the films. Accordingly, the scattering of incident light was enhanced in the short-wavelength region. Among the films of 6m-60s-xm-50s, the sample of 6m-60s-10m-60s showed the biggest grain size due to the low concentration growth. Consequently, it exhibited the strongest scattering in the long-wavelength region. Regarding the loading time effect on the scattering, the sample of 6m-10s-30m-50s showed its main grains of ca. 300 nm, in this case the scattering of incident light existed in the region of 350-500 nm while highest transmittance occurred in the long-wave regions (as shown in Fig. S2). As the MAI loading time increased, the perovskite films formed large grains of micrometers at the first step. Meanwhile, the sequential treatment of the high concentration MAI solution resulted in the dense films with some nano-grains. Therefore, compared to the sample of 6m-60s, these perovskite films had stronger scattering in the short-wavelength region and lower transmittances. Furthermore, the surface roughness also made contributions to the random scattering and re-absorption, which lead to strong photon-recycling in lead-halide perovskites because of the multiple absorption-diffusion-emission [17,18]. As a result, the large-grain perovskite films with some nano-grains and rough surfaces in our experiments achieved the enhanced absorptions in

the short-wavelength regions.

3.3.4 Photovoltaic performance of the solar devices

In order to evaluate the photovoltaic performance of the films, the mesoporous structured perovskite solar cells was fabricated as shown in Fig. 13. They were all assembled in ambient conditions with a high humidity of ca. 75%. And the MAI concentration effect and the loading time effect on photovoltaic performance were studied. Fig. 14 showed the MAI concentration effect on the *I-V* characteristics of the devices. The results showed that as the MAI concentration increased in the high concentration MAI solution treatment, the V_{oc}, J_{sc} and *PCE* of the devices increased. The low concentration MAI loading time effect on on the *I-V* characteristics of the devices are showed in Fig. 15. The results also indicated that as the MAI loading time increased at the low concentration MAI treatment, the V_{oc}, J_{sc} and *PCE* of the devices increased. The champion *I-V* data of each group was listed in Table 5. The champion device of the 6m-60s group exhibited a short current (J_{sc}) of 9.90 mA/cm^2, open-circuit voltage (V_{oc}) of 0.87 V and *PCE* of 5.25%. With the perovskite films treated by the high concentration MAI solutions, all the devices fabricated from the concentration gradient method obviously possessed higher photovoltaic performance than that of 6m-60s. Regarding the concentration effect, the group of 6m-60s-30m-50s showed the champion performance, with the highest J_{sc} of 18.09 mA/cm^2, V_{oc} of 0.98 V and *PCE* of 11.48%. Regarding the MAI loading time effect, the group of 6m-40s-30m-50s also showed the improved J_{sc} of 17.53 mA/cm^2, V_{oc} of 0.93V and *PCE* of 10.30%. As showed in the Table S1 and Table S2, there was a general tendency that the devices from the concentration gradient method exhibited higher photovoltaic performance than the traditional method. Therefore, the concentration gradient controlled growth looked like an effective method to prepare the high-quality films for high-performance perovskite solar cells.

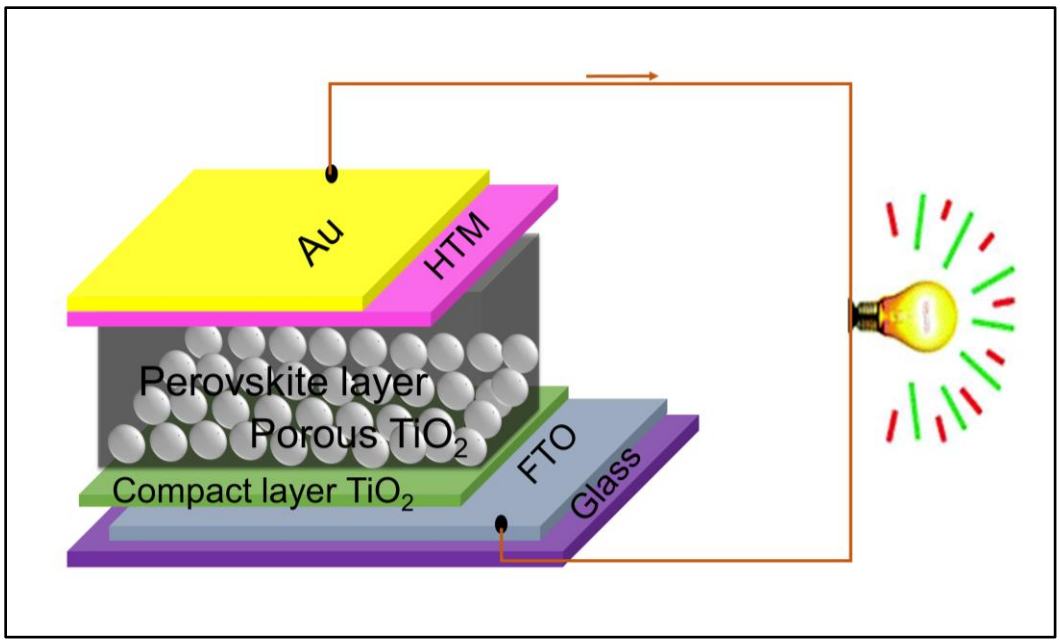

Fig. 13. Schematic of the mesoporous structured perovskite solar cells.

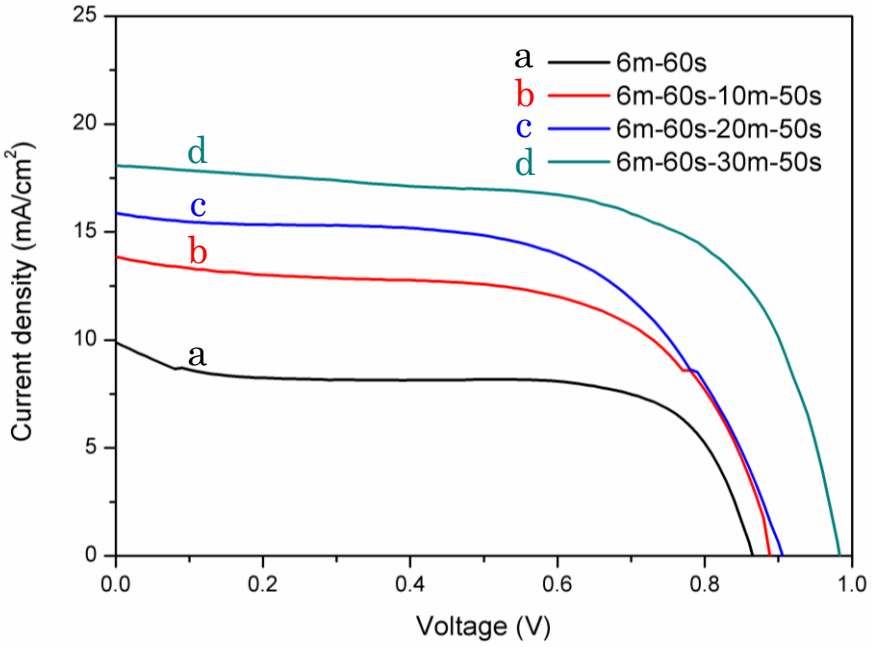

Fig. 14. MAI concentration effect on *I-V* characteristics of the perovskite solar cells under illumination of AM1.5G.

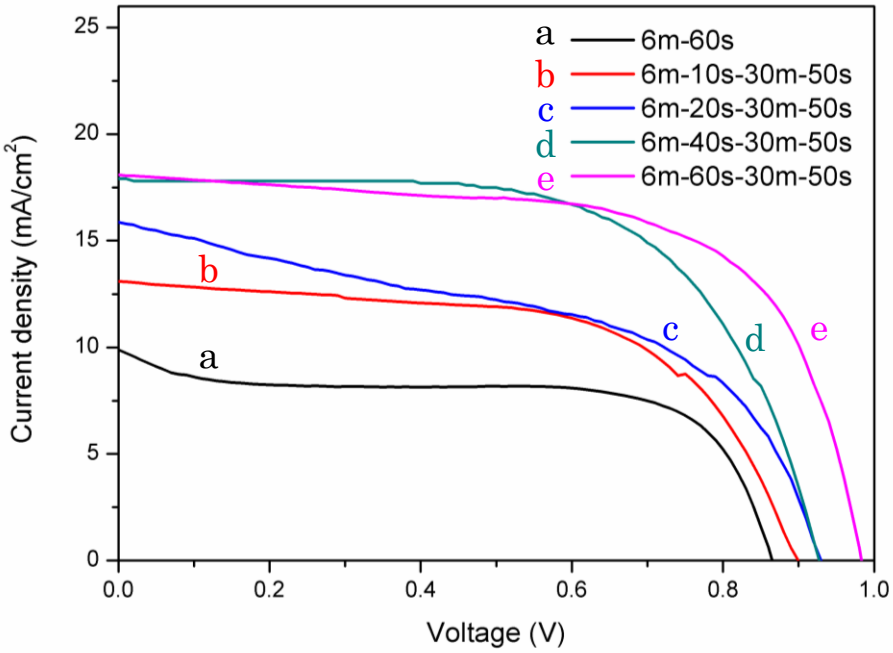

Fig. 15. MAI loading time effect on the *I-V* characteristics of the perovskite solar cells under illumination of AM1.5G.

Table 5. *I-V* characteristic of the champion solar devices of each group.

	J_{sc} (mA/cm^2)	V_{oc} (V)	FF	*PCE* (%)
6m-60s	9.89	0.87	0.61	5.25
6m-10s-30m-50	15.49	0.92	0.55	7.91
6m-20s-30m-50	14.53	0.89	0.53	6.81
6m-40s-30m-50	17.54	0.93	0.63	10.30
6m-60s-30m-50	18.09	0.98	0.65	11.48
6m-60s-20m-50	15.88	0.91	0.59	8.56
6m-60s-10m-50	13.85	0.89	0.61	7.52

The high performance of the perovskite solar cells was mainly due to the quality improvement of perovskite films. . First, the perovskite films via the concentration gradient method reached the better coverage than the sample 6m-60s, which can benefit to reduce the leakage current. At the same time, compared with the sample 6m-10s-30m-50s with nano-grains, the perovskite films with large grains can effectively reduce the grain boundaries and trapping centers. Second,

the concentration gradient controlled growth formed the perovskite films with little PbI_2 residue. The reduced PbI_2 residue in the perovskite films was reported to benefit the improvement of the photovoltaic performance of the device [19-21]. Moreover, the enhanced light absorption in the short-wavelength region can also make some contribution to the photovoltaic performance. Fig. 16 showed the comparison between the absorption and the AM1.5G solar irradiance. The energy distribution of the AM1.5G solar irradiance mainly located at the region of 450-800 nm [22]. Accordingly, it can be clearly seen that the enhanced absorption of the films could benefit the power conversion in the short-wavelength region. Compared with the sample 6m-60s, the samples of 6m-60s-30m-50s, 6m-40s-30m-20s 6m-60s-20m-50s showed a full coverage of the pure perovskite with small amount of nano-grains and significantly enhanced absorption in the short-wavelength region. Therefore, they performed as good candidates for the application on high-performance perovskite solar cells. In a word, the concentration gradient controlled growth of $CH_3NH_3PbI_3$ films must be a route to the perovskite solar cells with high-output.

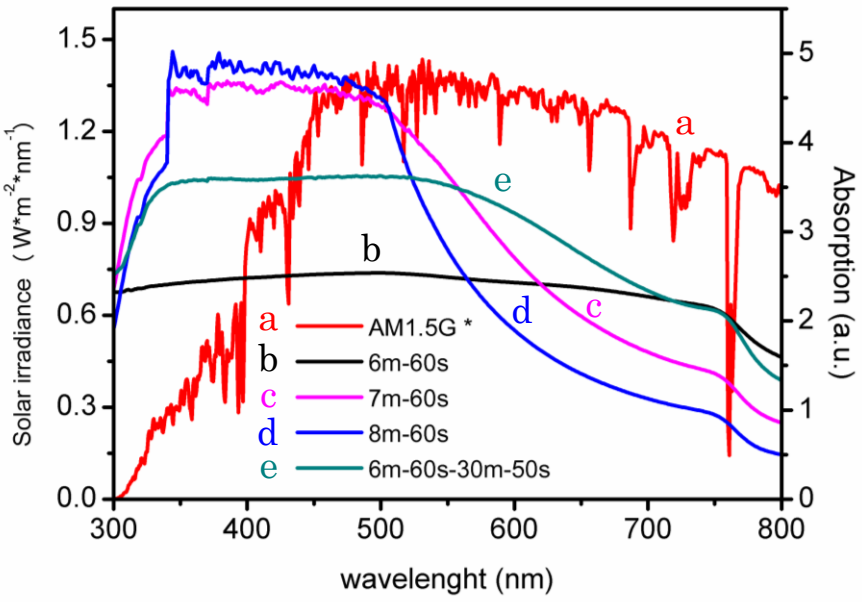

Fig. 16. Comparison of the UV-visible absorption of the samples with the AM1.5G solar irradiance. (* referred to [22])

3.3.5 Mechanism of concentration gradient controlled growth

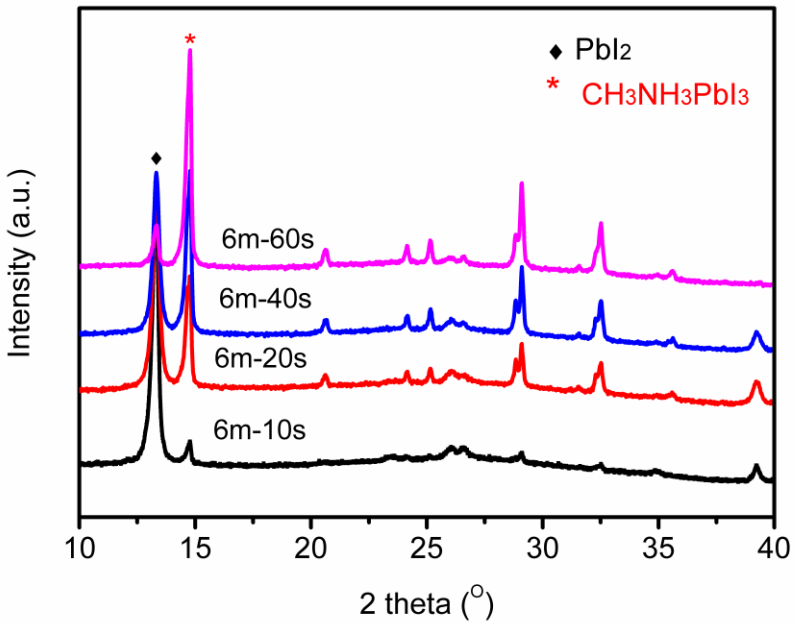

Fig. 17. Comparison of the XRD patterns of the samples of 6m-xs (x = 10, 20, 40, 60).

The two-step concentration gradient controlled growth resulted in the high-quality perovskite films. However, the mechanism is not so clear. Hereby the XRD and SEM were introduced to investigate the mechanism of the controlled growth. Fig. 17 showed the XRD patterns of the samples treated with 6 mg/ml MAI solutions for different times. The resulted revealed that as the MAI solution loading time increased, the content of perovskites in the films gradually increased, indicating a time-dependent reaction between the low concentration MAI solution and the PbI_2 films to form the $CH_3NH_3PbI_3$ perovskite.

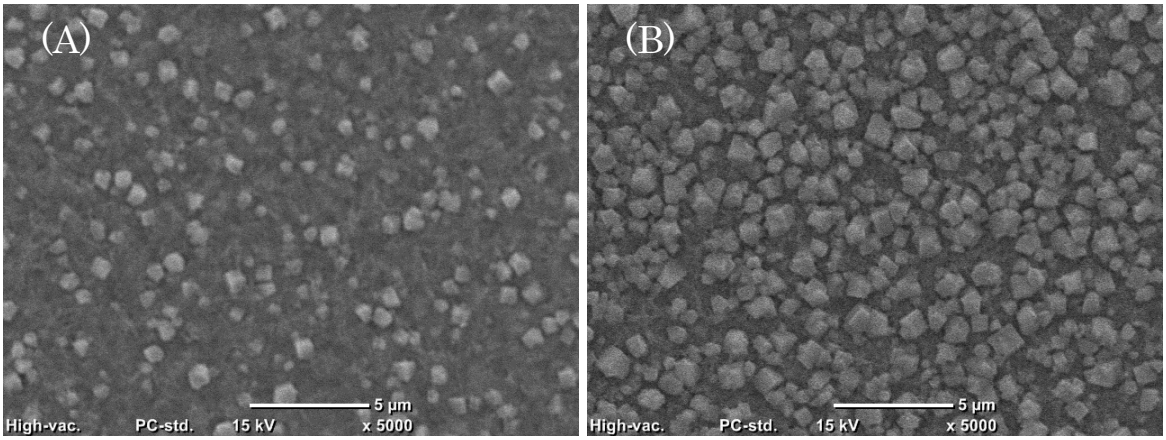

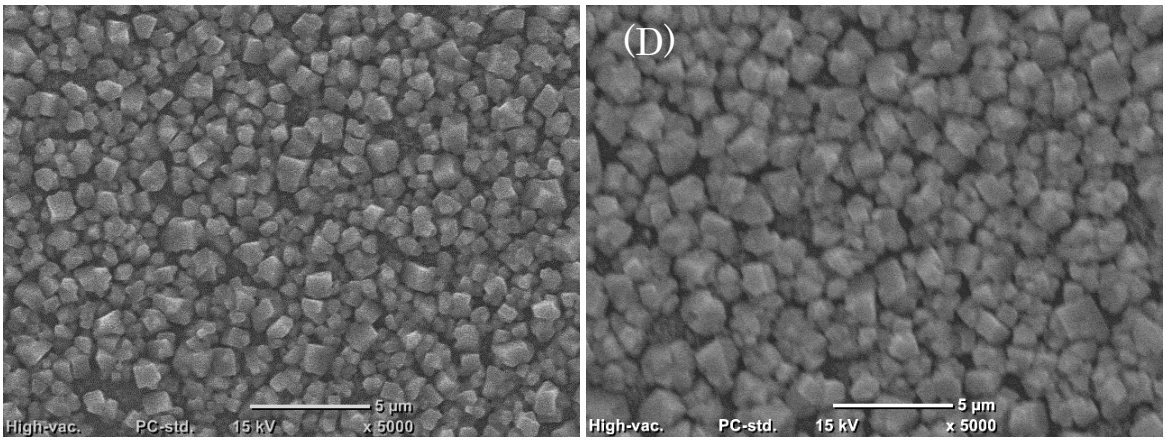

Fig. 18. SEM images of the surface morphology of the samples of 6m-xs. (A) x = 10. (B) x = 20. (C) x = 40. (D) x = 60.

When the MAI solution was loaded on the surface of the PbI_2 films, it slowly reacted with the PbI_2 and formed perovskites. Furthermore, the SEM images of the samples 6m-xs are shown in Fig. 18. They clearly demonstrated that small amount of small perovskite particles discontinuously distributed on the surface of the PbI_2 films after the 6 mg/ml MAI solution loaded for 10 seconds, with most of the PbI_2 film uncovered. As the MAI loading time increased, the particle size became bigger and the coverage of the perovskite films increased. However, even the loading time was up to 60 seconds and some particle size grown up to 1.5 μm, there were still PbI_2 residue and spaces in the films. According to the theory of crystal nucleation and growth, the nucleation calls for higher interfacial energy than grain growth [12,13]. During the formation of the perovskite films, the lower concentration MAI solutions offered less interfacial free energy between the solid surface and the solution. Consequently, only a few nucleation centers could occurred at the high-energetic sites at the PbI_2 films. After that, they performed as the perovskite seeds and grown up to the bigger grains. In contrast, the low-energetic sites at the PbI_2 films could not nucleate but remained due to the low interfacial free energy. As the reaction went on, the concentration of the MAI solution decreased, which made the nucleation of perovskite more difficult. Therefore, the sample 6m-60s formed a film with large perovskite grains and small amount of PbI_2 residue left at the spaces between the perovskite grains. In addition, the PbI_2 residue at the spaces was uncovered, thus it can be used for further reaction at the second step.

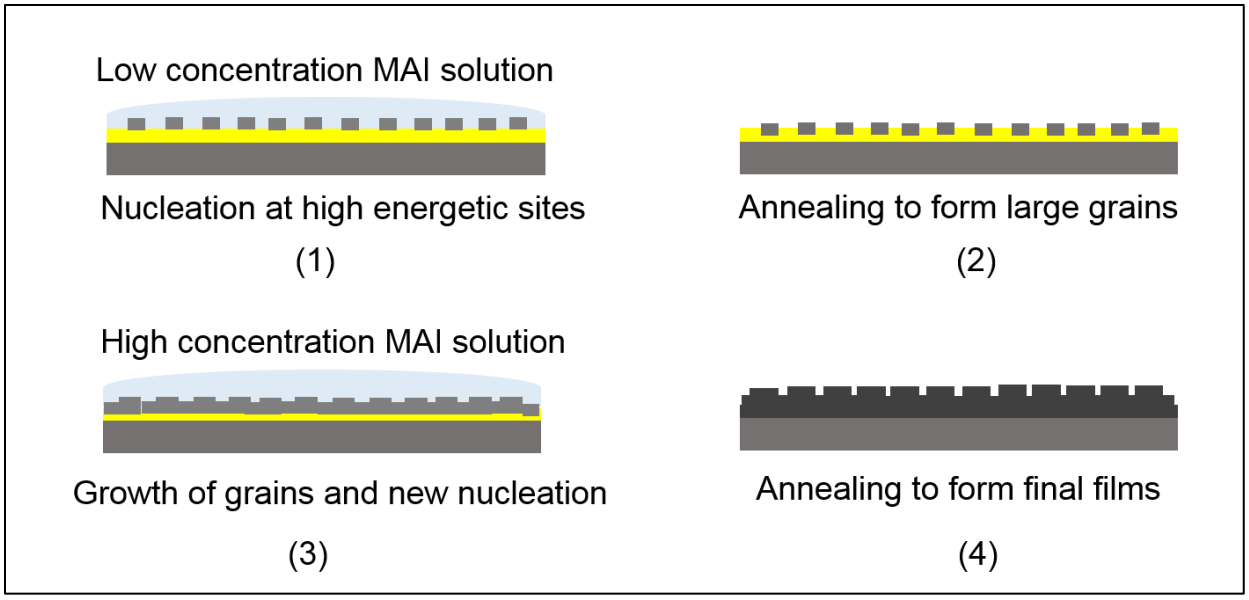

Fig. 19. Schematic illustration of the nucleation/crystallization for the formation of perovskite film via two-step concentration gradient growth.

According the discussion above, the mechanism of the concentration gradient controlled growth can be explained as Fig. 19. First, the PbI_2 films was formed at the substrates with some high-energetic sites at the surfaces. Second, when the 6 mg/ml MAI solution was loaded on the surfaces, the high-energetic sites reacted with the MAI solution and formed discontinuous perovskite seeds. Considering that the perovskite nucleation called for a higher interfacial free energy than grain growth, the low-energetic PbI_2 parts could not react with the low concentration MAI solution. Particularly, as the reaction went on, the MAI was consumed as well as the interfacial free energy decreased. Therefore, only the perovskite seeds formed at the high-energetic sites and grew up at this step. Third, when the high concentration MAI solutions were loaded on the surface of the films, these pre-formed perovskite grains performed as the seeds for the further reaction and continued to grow. At the same time, new nucleation occurred at the interface because the interfacial free energy increased. Consequently, new small perovskite grains formed and tightly filled the spaces between the former grains. Finally, the $CH_3NH_3PbI_3$ perovskite films with large grains and full coverage were formed on the substrates by the two-step concentration gradient controlled growth.

Regarding the loading time effect on the 6m-xs-30m-50s films, it mainly affected the growth of the perovskite grains at the first step. There were just a few perovskite grains discontinuously

left in the sample of 6m-10s after the 10 seconds reaction. Whereas, most of the PbI_2 film was uncovered, which resulted in too many nucleation centers at the second-step reaction. Therefore, the finally-prepared sample of 6m-10s-30m-50s mainly formed small grains of ca. 300 nm. As the MAI loading time increased at the first-step reaction, the perovskite grains grew up and gradually covered the films with larger perovskite grains, the fewer spaces and the less PbI_2 residue. When the 30 mg/ml MAI solution was loaded at the second-step, it reacted with the residue PbI_2 and triggered the new nucleation and growth of perovskite. These new grains filled the spaces between large grains and formed the perovskite films with large and small grains.

Regarding the MAI concentration effect on the 6m-60s-xm-50s films, it mainly affected the nucleation at the second steps. As mentioned above, the 10 mg/ml MAI solution offered higher interfacial energy than 6 mg/ml MAI solution, but lower interfacial free energy for the nucleation than 20 and 30 mg/ml MAI solutions at the second-step reaction. Therefore, in the sample of 6m-60s-10m-50s, the growth of the former perovskite grains dominated, resulting in larger grains but with some PbI_2 residue still left in the spaces after the reaction. When the higher concentration MAI solutions (20, 30 mg/ml) were loaded on the sample of 6m-60s, they offered higher interfacial free energy for the new nucleation and growth in the spaces. Consequently, the small perovskite grains were formed and filled the spaces, resulting in the complete reaction and the improved coverage of the films with the multi-sized perovskite grains [23].

3.4 Conclusion

In summary, we developed a new method to grow the high-quality $CH_3NH_3PbI_3$ perovskite films via the two-step concentration gradient controlled reactions. We used two concentration MAI solutions to prepare perovskite films. First, the MAI solution (6 mg/ml) induced the nucleation and the growth of perovskite grains in the first-step reaction, achieving large grains up to 1.4 μm with spaces between each other. And then the following treatment of the high concentration MAI solutions (10, 20, 30 mg/ml) resulted in the well-covered perovskite films with multi-size grains, which reduced grain boundaries and trapping centers. Due to the grain-size-dependent light scattering, the perovskite films with the large grains showed a significantly-enhanced absorption in the long-wavelength region, while the absorption of the perovskite films with small grains mainly located in the short-wavelength region. The energy distribution of the

sunlight indicated that the enhanced spectral absorption in the visible region can favor the power conversion of solar cells. Therefore, among the perovskite films prepared via the concentration gradient controlled growth, the films of 6m-60s-30m-50s, 6m-40s-30m-50s and 6m-60s-20m-50s showed large perovskite grains, well coverage and the strong absorption in the long-wavelength region, which can favor the photovoltaic performance of solar cells. Consequently, the corresponding solar devices fabricated in ambient conditions with high humidity showed an obviously enhanced short current of 18.09 mA/cm^2, open circuit voltage of 0.98 V and *PCE* up to 11.48%. Finally, a model of nucleation and growth has been developed to explain the mechanism for the concentration gradient controlled growth of the $CH_3NH_3PbI_3$ perovskite films.

Reference

[1] A. Kojima, K. Teshima, Y. Shirai, T. Miyasaka, Organometal halide perovskites as visible-light sensitizers for photovoltaic cells, J. Am. Chem. Soc. 2009, **131**, 6050-6051.

[2] Hui-Seon Kim, Chang-Ryul Lee, Jeong-Hyeok Im, Ki-Beom Lee, Thomas Moehl, Arianna Marchioro, Soo-Jin Moon, Robin Humphry-Baker, Jun-Ho Yum, Jacques E. Moser, Michael Grätzel, Nam-Gyu Park, Lead iodide perovskite sensitized all-solid-state submicron thin film mesoscopic solar cell with efficiency exceeding 9%, Sci. Rep. 2012, **2**, 591.

[3] National Renewable Energy Laboratory USA, Best research-cell efficiencies. http://www.nrel.gov/ncpv/images/efficiency_chart.jpg, 2017(accessed 17.01.03).

[4] Martin A. Green, Anita Ho-Baillie & Henry J. Snaith, The emergence of perovskite solar cells, Nat. Photonics, 2014, **8**, 506-514.

[5] Julian Burschka, Norman Pellet, Soo-Jin Moon, Robin Humphry-Baker, Peng Gao, Mohammad K. Nazeeruddin & Michael Grätzel, Sequential deposition as a route to high-performance perovskite-sensitized solar cells, Nature 2013, **499**, 316-319.

[6] Jeong-Hyeok Im, In-Hyuk Jang, Norman Pellet, Michael Grätzel & Nam-Gyu Park, Growth of $CH_3NH_3PbI_3$ cuboids with controlled size for high-efficiency perovskite solar cells, Nat. Nanotechnol. 2014, **9**, 927-932.

[7] Mengjin Yang, Taiyang Zhang, Philip Schulz, Zhen Li, Ge Li, Dong Hoe Kim, Nanjie Guo, Joseph J. Berry, Kai Zhu, Yixin Zhao, Facile fabrication of large-grain $CH_3NH_3PbI_{3-x}Br_x$ films for high-efficiency solar cells via CH_3NH_3Br-selective Ostwald ripening, Nat. Comm. 2016, **7**, 12305.

[8] Xiong Li, Dongqin Bi, Chenyi Yi, Jean-David Décoppet, Jingshan Luo, Shaik Mohammed Zakeeruddin, Anders Hagfeldt, Michael Grätzel, A vacuum flash-assisted solution process for high-efficiency large-area perovskite solar cells, Sciences 2016, **353** (6294), 58-62.

[9] Sibel Y. Leblebici, Linn Leppert, Yanbo Li, Sebastian E. Reyes-Lillo, Sebastian Wickenburg, Ed Wong, Jiye Lee, Mauro Melli, Dominik Ziegler, Daniel K. Angell, D. Frank Ogletree, Paul D. Ashby, Francesca M. Toma, Jeffrey B. Neaton, Ian D. Sharp, Alexander Weber-Bargioni, Perovskite solar cells: Different facets of performance, Nat. Energy 2016, **1**, 16093.

[10] D.Y. Son, J.W. Lee, Y.J. Choi, I.H. Jang, S. Lee, P.J. Yoo, H,J. Shin, N.Y. Ahn, M.S, Choi, D.H. Kim, Nam-Gyu Park, Self-formed grain boundary healing layer for highly efficient $CH_3NH_3PbI_3$ perovskite solar cells, Nat. Energy 2016, **1**, 16081.

[11] W.Z. Li, W. Zhang, S. Van Reenen, R. J. Sutton, J.D. Fan, A.A. Haghighirad, M.B. Johnston, L.D. Wang and H.J. Snaith, Enhanced UV-light stability of planar heterojunction perovskite solar cells with cesium bromide interface modification, Energy Environ. Sci. 2016, **9**, 490-498.

[12] J.A. Venables, G.D.T. Spiller and M. Hanbucken, Nucleation and growth of thin films, Rep. Prog. Phys. 1984, **47**, 399-459.

[13] S.E. Offerman, N.H. van Dijk, J. Sietsma, S. Grigull, E.M. Lauridsen, L. Margulies, H.F. Poulsen, M.T. Rekveldt, S. van der Zwaag, Grain nucleation and growth during phase transformations, Science 2002, **298** (5595), 1003-1005.

[14] G. Mie, Analen der physic, 1908*,* **25** (3), 377.

[15] M. Mishchenko, L. Travis, A. Lacis. Scattering, Absorption, and Emission of Light by Small Particle*s*. New York: Cambridge University Press (2002).

[16] P.W. Barber, S. S. Hill, Light scattering by particles: Computational methods. Singapore: Advanced Series in Applied Physics 2 (1990).

[17] L.M. Pazos-Outón, M. Szumilo, R. Lamboll, J.M. Richter, M.C. Quesada, M.A. Jalebi, H.J. Beeson, M. Vrućinić, M. Alsari, H.J. Snaith, B. Ehrler, Photon recycling in lead iodide perovskite solar cells, Science 2016, **351** (6280), 1430-1433.

[18] Eli Yablonovitch, Lead halides join the top optoelectronic league, Science 2016, **351** (6280), 1401.

[19] Yixin Zhao and Kai Zhu, Three-step sequential solution deposition of PbI_2-free $CH_3NH_3PbI_3$ perovskite, J. Mater. Chem. A 2015, **3**, 9086-9091.

[20] Y.Y. Zhou, M.J, Yang, A.L. Vasiliev, H.F. Garces, Y.X. Zhao, D. Wang, S.P. Pang, K. Zhu, N.P. Padture, Growth control of compact $CH_3NH_3PbI_3$ thin films via enhanced solid-state precursor reaction for efficient planar perovskite solar cells, J. Mater. Chem. A 2015, **3** (17), 9249-9256.

[21] T.Y. Zhang, M.J. Yang, Y.X. Zhao, K. Zhu, Controllable sequential deposition of planar $CH_3NH_3PbI_3$ perovskite films via adjustable volume expansion, Nano Lett. 2015, **15** (6), 3959-3963.

[22] National Renewable Energy Laboratory USA, Reference Solar Spectral Irradiance: Air Mass 1.5, http://rredc.nrel.gov/solar/spectra/am1.5/, 2017(accessed 17.01.03).

[23] Chunfeng Lan, Shuai Zhao, Chu Zhang, Weiguo Liu, Shuzi Hayase, Tingli Ma, Concentration gradient controlled growth of $CH_3NH_3PbI_3$ films and light-scattering-enhanced

spectral absorption in long- wavelength region, CrystEngComm, 2016, **18**, 9243-9251.

Chapter 4. Effect of lead-free $(CH_3NH_3)_3Bi_2I_9$ perovskite addition on spectrum absorption and enhanced photovoltaic performance of bismuth triiodide solar cells

4.1 Introduction

Halide perovskites have many excellent optical properties, such as suitable bandgaps and small effective mass, making them excellent absorbing materials for solar cells [1-3]. The power conversion efficiency (*PCE*) of halide perovskite solar cells certified by the National Renewable Energy Lab has sharply increased to 22.1% in the past six years, making them quite comparable with silicon solar cells in the near future [4]. However, there are still several drawbacks for halide perovskite solar cells, such as the degradation of perovskite when exposed to air, hysteresis and lead pollutions, which hinder their further commercialization [5-8]. Recent work pointed out that bismuth compounds can be potential candidates to solve the lead-pollution for future perovskite solar cells [9].

Lead-free bismuth compounds, such as Bi_2CrFeO_6, BiI_3 and $A_3Bi_2I_9$ perovskites (A = CH_3NH_3, Cs), have attracted much attention for photovoltaic applications [10-13]. The $A_3Bi_2I_9$ perovskites are air-stable and lead-free halide perovskites among these materials. Unfortunately, their bandgaps are up to 2.1 eV, too high for efficient visible light absorption. Therefore, the $A_3Bi_2I_9$ solar cells exhibited the *PCE* not higher than 1.02% [13-15]. BiI_3 was reported with the bandgaps between 1.43 and 2.2 eV. It was considered as a promising absorber owning to its high absorption coefficient (10^5 cm^{-1}) and electron mobility (260±50 $cm^2/(V \cdot s)$), as well as low carrier concentration (1×10^8 cm^{-3}) [11,16-18]. However, the BiI_3 solar cells still exhibited a low power conversion efficiency (*PCE*) and open circuit voltage (V_{oc}). One explanation for this phenomenon was attributed to the mismatching alignment of the energy levels between BiI_3 and TiO_2 [11]. Therefore, spectral absorption tuning and energy levels realignment are important topics for the development of bismuth compounds for solar cell applications.

As we know, the co-absorption of two dyes for the active layer is an efficient approach to tune spectral absorption for the dye-sensitized solar cells, e.g. mixed organic dyes of PcS15 and D131

exhibited a dramatic enhancement of the photocurrent response for the entire visible-light region with tuning of the electron-pushing abilities [19]. In addition, the integration of ZnS, CdS and $Cu_{2-x}S$ inorganic materials can lead to a staggered gap alignment, full-spectrum solar energy absorption and efficient charge separation [20], and the Pb-In binary perovskites cells also exhibited a higher PCE than single In-based perovskite solar cells [21]. Therefore, the integration of lead-free materials could be a potential method to tune their spectral absorption and realign their energy levels. In this article, the composite active layers of BiI_3 and $(CH_3NH_3)_3Bi_2I_9$ (abbreviated as MBI) were prepared, and their optical properties were studied for the lead-free solar cell applications.

4. 2 Experimental

4.2.1 Preparation of $(BiI_3)_{1-x}(MBI)_x$ composite films

589 mg of BiI_3 was dissolved in 1 mL of N, N-dimethyl- at room temperature. It was filtered using PTFE syringe filters (0.45 μm) before further processed. MBI can be prepared from the solution with BiI_3 and CH_3NH_3I (MAI) (molar ratio = 1:1.5) [15]. Therefore, the precursors of BiI_3 and MBI mixtures were prepared by adding different contents of MAI into the BiI_3 solution (stoichiometric $(BiI_3)_{1-x}(MBI)_x$, x = 0, 0.10, 0.20, 0.50, 0.75 and 1.0). After mixed by ultrasonic mixer for 20 minutes, 0.15 ml of the precursors were dropped on regular glass substrates which were covered with the mesoporous TiO_2 layer, and then spin coated at a speed of 2000 rpm for 20 seconds. And then these films were annealed at 100 ºC for 30 min under ambient conditions to obtain different $(BiI_3)_{1-x}(MBI)_x$ films of 170 μm for the measurements of X-ray diffraction, UV-visible spectrum and surface morphology. For the measurement of the valence band, the samples were prepared on fluorine-doped tin oxide glass substrates through the same method.

4.2.2 Fabrication of devices

FTO glass substrates were etched with 2 M HCl and zinc power, washed with IPA, acetone and clean water, and then dried before use. The TiO_2 precursor was prepared as reported in Ref. [22]. It was spin coated on the substrates, and then sintered at 450 ºC for 1 hour to form a compact layer. After that, the mesoporous TiO_2 gel was spin coated on the compact layer and sintered at 500 ºC for 30 minutes. When the substrates were cooled down, 0.15 ml of $(BiI_3)_{1-x}(MBI)_x$ precursors were dropped on them, and then spin coated at 2000 rpm for 20 seconds.

These films were annealed on hotplate at 100 ^{o}C for 30 minutes. For the preparation of hole transport materials (HTMs), 72.3 mg of Spiro-OMeTAD, 28.8 µl of 4-tert-butylpyridine and 17.5 µl of a stock solution of 520 mg· ml^{-1} lithium bis-(trifluoromethyl sulphonyl) imide in acetonitrile were dissolved in 1 ml of chlorobenzene. The solution was spin coated on the bismuth composite layers to form a hole transport layer. Finally, 30 nm of silver was evaporated on the samples to form an electrode. In our experiment each group consisted of four devices. And all the processes were taken out in ambient conditions with the humidity of ca. 55%.

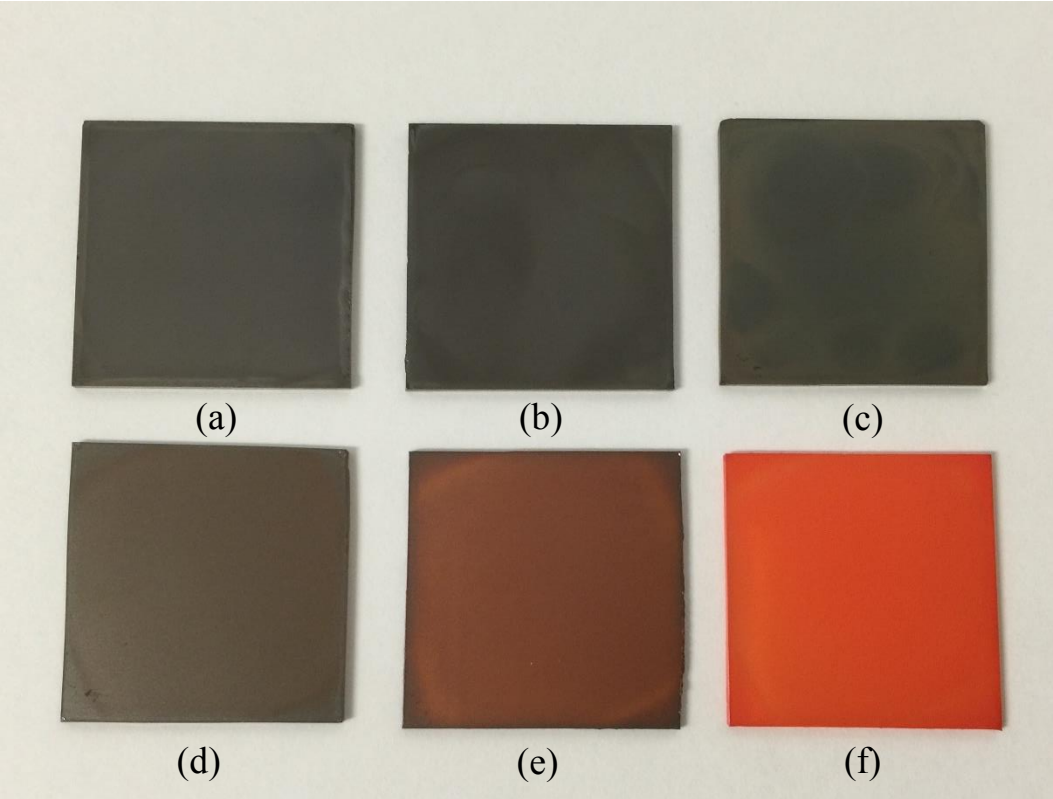

Fig. 1. $(BiI_3)_{1-x}(MBI)_x$ films prepared by the solution method (from left to right, top to bottom:(a) x = 0, (b) x = 0.10, (c) x = 0.20, (d) x = 0.50, (e) x = 0.75, (f) x = 1.0).

4.2.3 Characterization

The X-ray diffracting diagram was measured from 10 ° to 40 ° at a scanning speed of 0.01 °/s using a X-ray diffractometer (XRD, RINT 2100, Rigaku) with Cu *Kα* radiation (λ = 1. 54056 Å). The scanning electron microscope (SEM, JCM-6000, JEOL) was used to characterize the microstructures. Energy dispersive X-ray spectrometry (EDX, Genesis XM2, EDAX) was

applied to determine the stoichiometric ratio of the composite films by detecting the molar ratios of I: Bi atoms. A UV-VIS-NIR spectrophotometer (V-670, JASSCO) was used to determine the optical properties of the products by the absorption spectra, and the bandgaps were calculated using the Tauc Plot. An ionization energy measuring device was used to evaluate the valence band by photoelectron yield spectroscopy (PYS, KV205-HK, Bunkoukeiki). Photovoltaic characteristics of the solar devices were measured by a solar simulator (CEP-2000, Bunkoukeiki) interfaced with a xenon lamp (BSOX150LC, Bunkoukeiki) at 100 mW/cm^2 under AM 1.5 conditions. The power of the light exposure from the solar simulator was fixed with an amorphous Si photodetector (BS-520 S/N 353, Bunkoukeiki) to avoid any discrepancy between the calibrated diode and the measured devices. The cell area was precisely controlled using a 0.12 cm^2 black metal mask to measure the photovoltaic performances. And the *I-V* characteristic was determined by the forward scanning and reserve scanning.

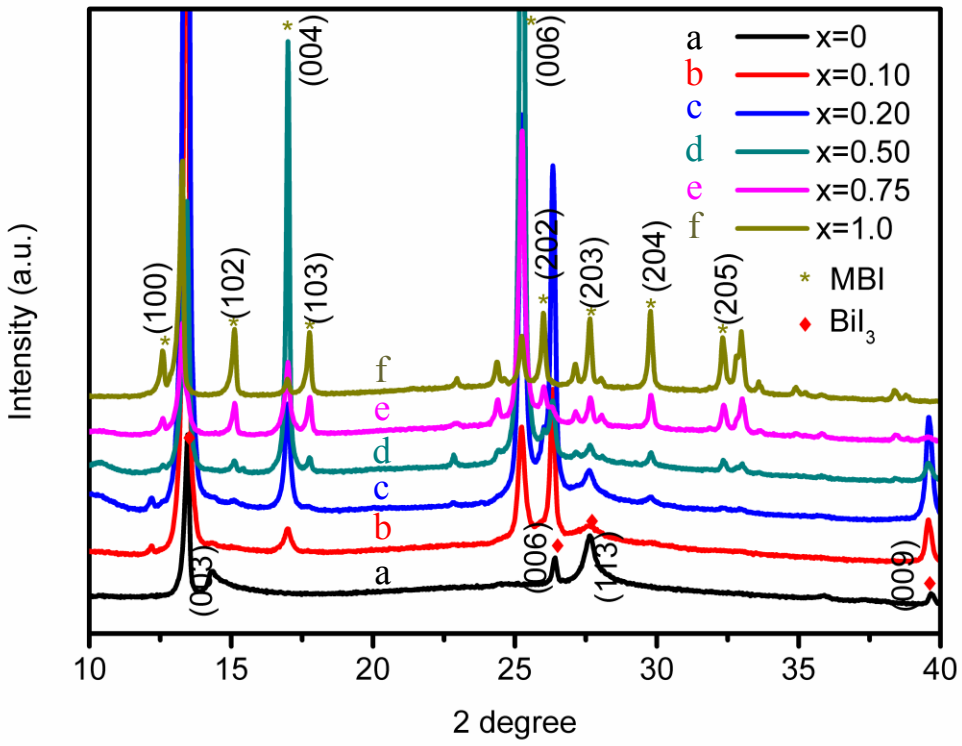

Fig. 2. XRD patterns of the $(BiI_3)_{1-x}(MBI)_x$ films.

4.3 Results and discussion

As shown in Fig. 1, the color of the as-prepared films was significantly affected by the addition of MAI. It changed from black to red, implying that certain reaction has occurred after the addition of MAI. Fig. 2 showed the XRD patterns of the films. For the film without the MAI additive, the XRD pattern demonstrated a pure hexagonal BiI_3 phase, consistent with the BiI_3 film diffraction data reported in the literature (JCPDS, 7-269) [20]. With the MAI added into the precursors, the intensity of BiI_3 peaks changed and the hexagonal MBI was formed as the second phase. For x = 0.10 and x = 0.20, the (003) peaks of BiI_3 dramatically increased, implying an enhanced crystallization. As x increased to 0.50 and 0.75, the MBI phase replaced BiI_3 and dominated in the samples. Finally, it formed a pure hexagonal MBI phase when x = 1.0, matching the MBI diffraction data reported in Ref. [15]. For the films where BiI_3 dominated, the (003)-orientation of BiI_3 was evaluated by the lotgering factor (LF) as following [22,23].

$$\mathrm{LF} = \frac{P-P0}{1-P0} \tag{1}$$

where P is defined as the following equation.

$$P = \frac{I(003)}{(I(003)+I(113))} \tag{2}$$

where I(003) and I(113) are the intensities of peak (001) and (113) respectively. And P0 is calculated from the BiI_3 with a random particle distribution (PDF#48-1795). The LF varies from 0 to 1; LF = 0 corresponds to random orientation, and LF = 1 to perfect orientation. As showed in Table 1, the LF for the films of x = 0, 0.10 and 0.20 were 0.686, 0.973 and 0.979, respectively, indicating higher (003)-orientation with more MBI. However, The MAI phase wasn't found in any films, suggesting that a chemical reaction occurred between MAI and BiI_3 as follows:

$$2\ BiI_3 + 3\ CH_3NH_3I \rightarrow (CH_3NH_3)_3Bi_2I_9 \tag{3}$$

Table 1. Lotgering factors of BiI_3 (003)-orientation calculated by the intensities of the peak (003) and (113) from the XRD results.

	Intensity of peak (003)	Intensity of peak (113)	P	LF
PDF#48-1795	17	100	0.145	0
x = 0	13110	4790	0.732	0.686
x = 0.10	91455	2160	0.977	0.973
x = 0.20	152390	2725	0.982	0.979

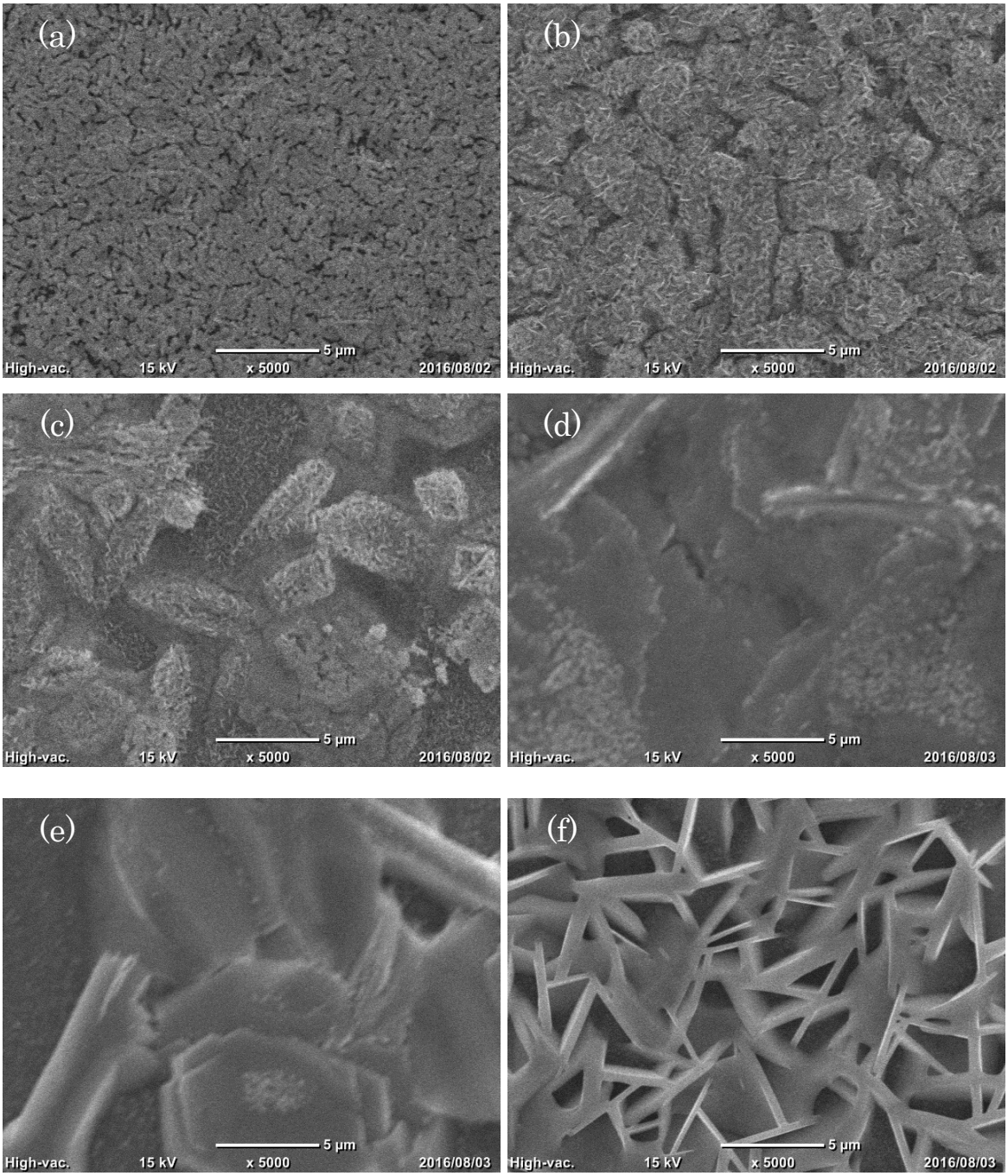

Fig. 3. FE-SEM images of surface morphology of the $(BiI_3)_{1-x}(MBI)_x$ films. (a) x = 0, (b) x = 0.10, (c) x = 0.20, (d) x = 0.50, (e) x = 0.75, (f) x =1.0.

The SEM images in Fig. 3 showed the surface morphologies of the films. We can see that the introduction of MBI significantly affected the crystallization and the morphologies of the

composite films. Fig. 3(a) revealed that the BiI_3 film was a film of small grains and with some micro-cracks. Fig. 3(b) revealed that in the composite film of x = 0.10, the BiI_3 grains became larger with some MBI crystal seeds formed at them. Also, Fig. 3(c) showed that the dense composite film (x = 0.20) was formed with larger BiI_3 grains, and the MBI sheets still existed in the BiI_3 grains as nano-sheets. However, as mentioned in the XRD results, when $x \geq 0.5$ the MBI dominated in the composite films. Correspondingly, the surface morphologies were totally changed. As shown in Fig. 3(d, e), the layer-structured MBI grains were mainly grown as (001)-oriented with the grain size larger than 5 μm. Some gel-like substances and disconnection also existed in these films. Finally, as shown in Fig. 3(f), the MBI film displayed a texture-structured non-oriented growth. Regarding the composite effect on surface morphologies of the films, even though both BiI_3 and MBI are hexagonal with Bi^{3+} and I^-, the lattice mismatching made them hard to form homogenous alloys but created lots of BiI_3-MBI interfaces [15,23]. Regarding the enlarged grains in the composite films, the mechanism is not yet to be clarified. One explanation is that the MBI nano-sheets performed as nucleation centers for the major BiI_3 phase [24]. The other explanation is that low concentration benefited the growth up of large BiI_3 grains [25].

The EDX data is shown in Fig. S1 and Table 2. The molar ratios of I:Bi atoms calculated from the EDX results were 3.06, 3.19, 3.40, 3.98, 4.20 and 4.68. Correspondingly, the stoichiometric ratios of MBI: BiI_3 in the films were in agreement with the precursors. Hence, these films were signed as $(BiI_3)_{1-x}(MBI)_x$ in the following discussion. At last, it should be pointed out that the crystallization of the films is not so comparable as that processed by a physical method [11,12], which can influence the performance of solar cells.

Table 2. Comparison of the molar ratios of I:Bi atoms in precursors and the $(BiI_3)_{1-x}(MBI)_x$ films.

	x=0	x=0.10	x=0.20	x=0.50	x=0.75	x=1.0
molar ratio of I:Bi in Precursors	3	3.15	3.30	3.75	4.125	4.5
molar ratio of I:Bi from EDX results	3.06	3.19	3.40	3.98	4.20	4.68

(a)

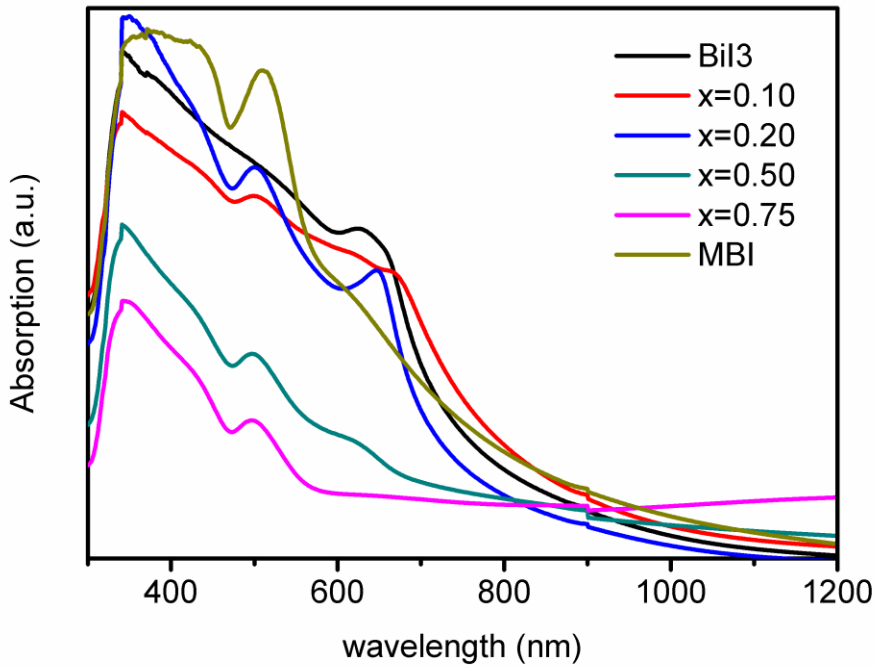

(b)

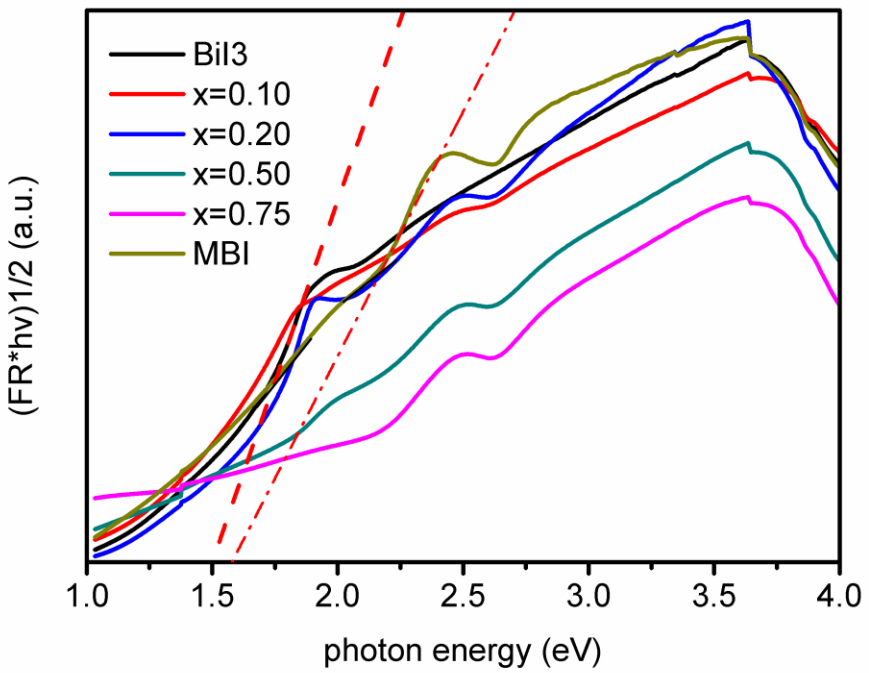

Fig. 4. UV-visible absorption spectrum of the $(BiI_3)_{1-x}(MBI)_x$ films. (a) Absorption strength. (b) Tauc plot of ($h\gamma$)versus ($h\gamma$ *absorption)$^{1/2}$.

As shown in Fig. 4(a), the UV-visible spectral absorption of the $(BiI_3)_{1-x}(MBI)_x$ films was

investigated in the wavelength range of 300-1200 nm. The absorption onsets of the BiI_3 film and the MBI film located at ca. 700 nm and 590 nm, respectively. However, the absorption onsets of the composite films varied with the content of the MBI, showing a phenomenon of multi-absorptions. Meanwhile, there was a phenomenon of weakened absorption strength in the composite films, especially for the samples of $(BiI_3)_{0.5}(MBI)_{0.5}$ and $(BiI_3)_{0.25}(MBI)_{0.75}$. The mechanism for such a phenomenon can be explained by multiple factors. One explanation is that the large grains in the composite films reduced the light scattering and harvesting [26]. The other could be that the gelatinous substances affected the absorption of the $(BiI_3)_{0.5}(MBI)_{0.5}$ and $(BiI_3)_{0.25}(MBI)_{0.75}$ composites films [27]. The detailed bandgaps of the BiI_3 and MBI films were calculated with the Tauc equation [28]:

$$\alpha h\gamma = \beta(h\gamma - E_g)^n \quad (4)$$

where α is the absorption coefficient, $h\gamma$ is the photon energy, β is a constant, and E_g is the bandgap. Considering that BiI_3 and MBI were reported as indirect bandgap materials, n = ½ is used for the evaluation [11,15]. Therefore, as shown in Fig. 4(b), the bandgaps of the BiI_3 and MBI films were estimated to be 1.77 and 2.15 eV, respectively. However, it is impossible to directly evaluate the bandgaps of the composite films because of the multi-absorption effects.

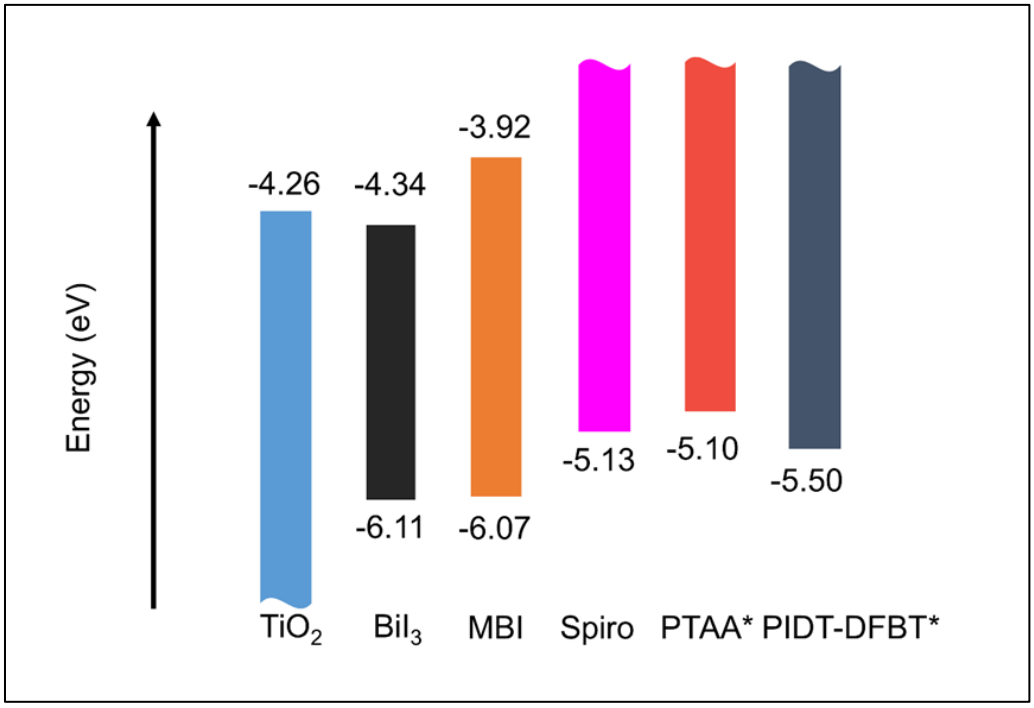

Fig. 5. Energy band diagram of the BiI_3 and MBI films. * Ref [11].

Table 3. Valance bands of the $(BiI_3)_{1-x}(MBI)_x$ films (x = 0, 0.1, 0.2, 0.5, 0.75, 1.0).

x	0	0.10	0.20	0.50	0.75	1.0
Valance band (eV)	-6.11	-6.11	-6.11	-6.06	-6.10	-6.07

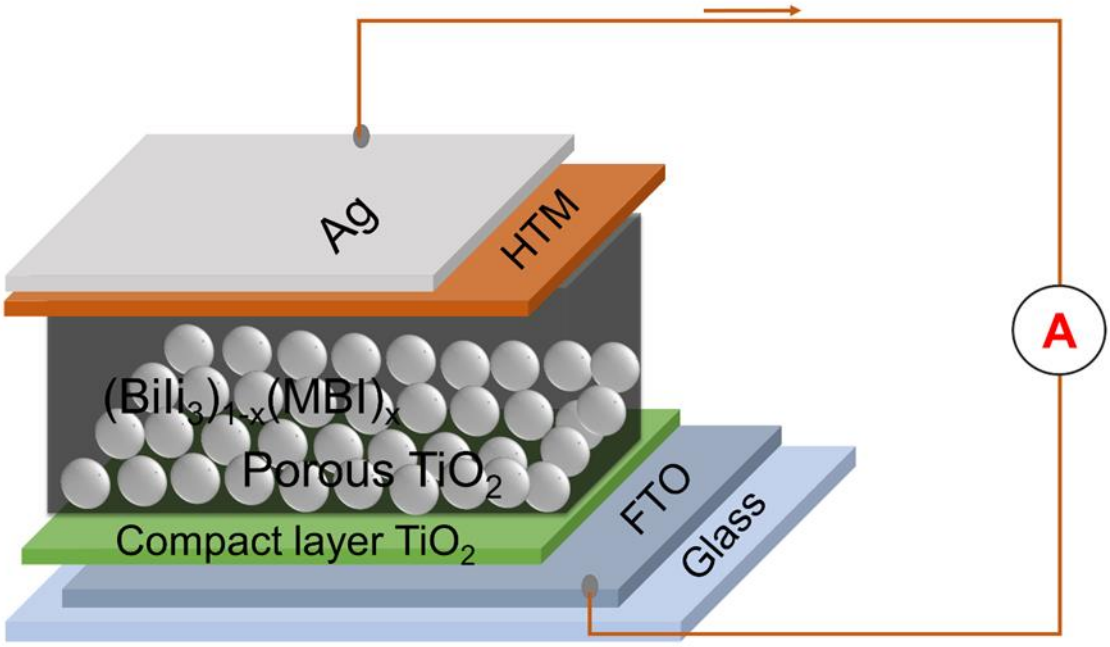

Fig. 6. Schematic of the $(BiI_3)_{1-x}(MBI)_x$ solar cells.

Energy level matching is a key point affecting the charge transport in solar cells. In order to experimentally estimate the energetic position of the valence band, PYS was performed on the $(BiI_3)_{1-x}(MBI)_x$ films growing on the FTO substrates. As shown in Fig. S2 and Table 3, all the valence bands of the $(BiI_3)_{1-x}(MBI)_x$ films are approximately -6.10 eV, showing little dispersion when x varies from 0 to 1.0. This is because the top of the valence band in BiI_3 and MBI materials is mainly contributed to the antibonding 6s character of the partially oxidized Bi^{3+} cation and I^- anion, and both of the materials were reported with a valence band of around -6.00~-6.10 eV [11,15]. Therefore, there was no obvious dispersion observed in the valence band in the $(BiI_3)_{1-x}$ $(MBI)_x$ composites. In contrast, the spin−orbit coupling along with the large atomic weight of the Bi^{3+} cation can lead to a more disperse conduction band and lower electron effective mass [15-17]. Accordingly, a schematic energy band diagram is constructed in Fig. 5,

where the conduction band of MBI is higher than TiO_2 while that of BiI_3 is a bit lower than TiO_2. However, owing to that the bandgaps of the composites cannot be precisely qualified, it is unable to quantitatively determine their conduction bands here.

The $(BiI_3)_{1-x}(MBI)_x$ solar cells were fabricated in order to evaluate their potential application for solar cells. As illustrated in Fig. 6, the $(BiI_3)_{1-x}(MBI)_x$ solar cells were with a structure of FTO/ compact-TiO_2/mesoprous-TiO_2&absorber/HTM/Ag. The champion *I-V* data of each group is presented in Table 4, and the *I-V* curves are shown in Fig. 7. All the $(BiI_3)_{1-x}(MBI)_x$ devices showed photovoltaic outputs in our study, in which the BiI_3 solar cell showed the V_{oc} of 0.44 V, J_{sc} of 0.25 mA/cm^2 and *PCE* of 0.045%, and the MBI solar cell showed a V_{oc} of 0.46 V, J_{sc} of 0.13 mA/cm^2 and *PCE* of 0.023%. Interestingly, as shown in Fig. S3 and Table S1, there was a phenomenon that, with a small amount of the MBI into the BiI_3 films, the photovoltaic performance was significantly enhanced in the solar cells, in which the $(BiI_3)_{0.8}(MBI)_{0.2}$ solar cells reached the optimum performance. Compared with the BiI_3 solar cells, they showed the champion *PCE* increased from 0.045% to 0.076% and the V_{oc} obviously improved from 0.44 to 0.57 V.

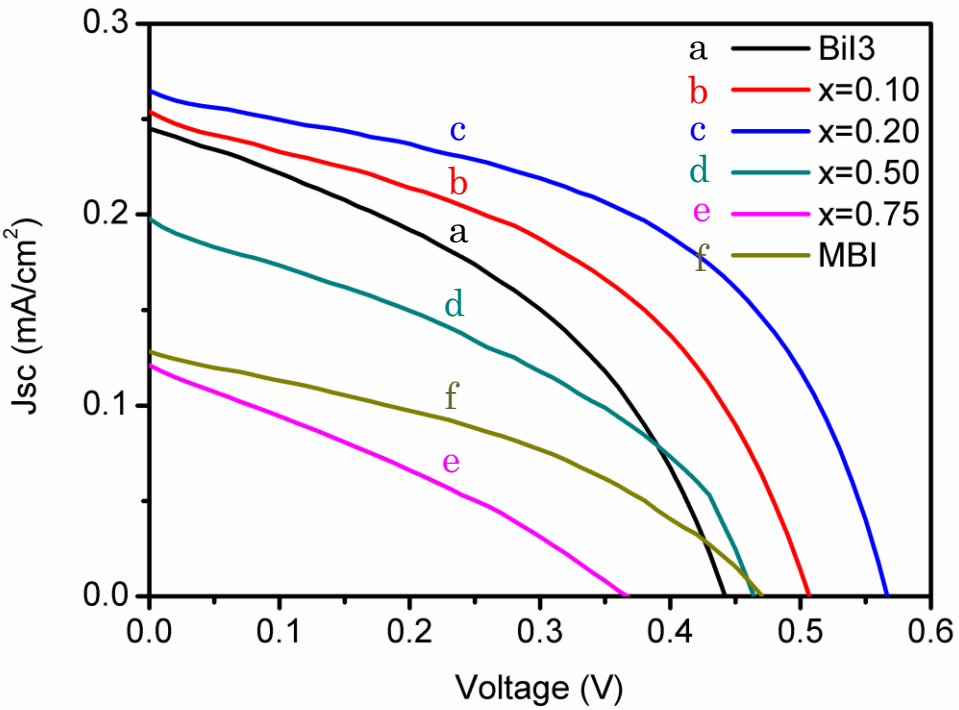

Fig. 7. *I-V* characteristics of the $(BiI_3)_{1-x}(MBI)_x$ solar cells.

Table 4. *I-V* characteristic of the champion $(BiI_3)_{1-x}(MBI)_x$ solar cells.

	0	0.10	0.20	0.50	0.75	1
Jsc (mA/cm^2)	0.245	0.254	0.265	0.197	0.121	0.128
V_{oc} (V)	0.442	0.507	0.567	0.465	0.366	0.460
FF	0.417	0.453	0.503	0.385	0.298	0.367
PCE (%)	0.0451	0.0582	0.0755	0.0354	0.0132	0.0231
Series resistance (Ω)	3953	3975	3075	2984	9429	8153
Shunt resistance (Ω)	36938	43781	56962	35790	18777	33303

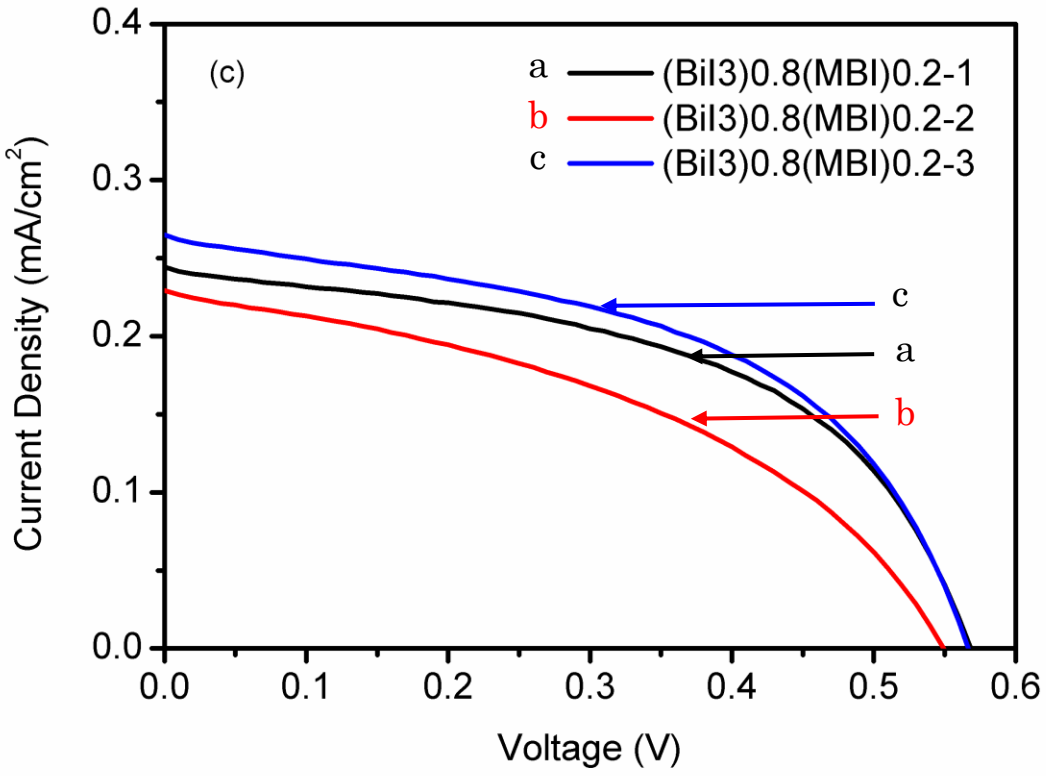

Fig. 8. *I-V* characteristics of the $(BiI_3)_{0.8}(MBI)_{0.2}$ solar cells.

The photovoltaic performance of the solar cells strongly depended on the $(BiI_3)_{1-x}(MBI)_x$ active layers. For the BiI_3 and the MBI solar cells, the energy band diagram suggested that the

photo-excited holes from the BiI_3 and the MBI films can be injected into the Spiro assuming a good separation. However, since the conduction band of BiI_3 was quite proximate to that of TiO_2, there were no enough driving force for the excited electron injection from BiI_3 into the TiO_2 layer [18]. And the theoretical *PCE* of BiI_3 solar cells would probably have a relatively low maximum. Accordingly, as shown in Table 5, the BiI_3 solar cells with PTAA/ PIDT-DFBT as HTMs fabricated from a physical method only showed the V_{oc} of 0.22 and 0.42 V [11]. In our experiments we obtained a higher V_{oc} of 0.44 V but the *PCE* of the BiI_3 solar cell was still very low. For the MBI perovskite solar cells, the low *PCE* was mainly because the bandgap of MBI is too large for effective absorption of visible light.

Table 5. *I-V* characteristic of the $(BiI_3)_{1-x}(MBI)_x$ and the BiI_3 solar cells reported.

	ETM	HTM	HOMO of HTM (eV)	V_{oc} (V)	J_{sc} (mA/cm^2)	*PCE* (%)
BiI_3	TiO_2	Spiro	-5.15	0.442	0.245	0.0451
$(BiI_3)_{0.8}(MBI)_{0.2}$	TiO_2	Spiro	-5.15	0.567	0.265	0.0755
BiI_3 -1 *	TiO_2	PTAA	-5.1	0.22	3.85	0.367
BiI_3-2 *	TiO_2	PIDT-DFBT	-5.5	0.44	2.39	0.0231

* reported in Ref. [11].

Regarding the enhanced photovoltaic performance in the composite solar cells, there are two explanations on it. First, it was attributed to the improved crystallization and coverage. As the XRD and SEM results mentioned above, the introduction of MBI significantly improved the BiI_3 crystallization of the $(BiI_3)_{0.8}$ $(MBI)_{0.2}$ films and optimized the film quality, this can effectively reduce the recombination and leakage in the devices. Moreover, the series resistance of the $(BiI_3)_{0.8}(MBI)_{0.2}$ solar cells was relatively lower than others, indicating a more effective charge transport. Second, it was attributed to the band bending in the composite films. As shown in Fig. 8, the band bending occurred at the MBI-BiI_3 interfaces in the $(BiI_3)_{1-x}(MBI)_x$ composites. When two semiconductors are in contact, the electrons of the high conduction band material and that of the low conduction band material can migrate to each other, forming a stable space charge region at the hetero-interface and an upward band-bending at the interface [29]. Therefore, compared with the BiI_3, the conduction band of the $(BiI_3)_{1-x}(MBI)_x$ composite systems became higher. Considering that the conduction band of the pure BiI_3 is approaching to the TiO_2, the band bending can make the injection of the photon-excited electrons easier from the composite

absorbing layers into the TiO_2. Particularly, because the large amount of the MBI nano-sheets in the BiI_3 grains created lots of BiI_3-MBI interfaces, the conduction bands of the whole BiI_3-MBI systems have been improved compared to that of the pure BiI_3 films. Therefore, the obviously enhanced V_{oc} and *PCE* are observed in the $(BiI_3)_{0.8}(MBI)_{0.2}$ solar cells.

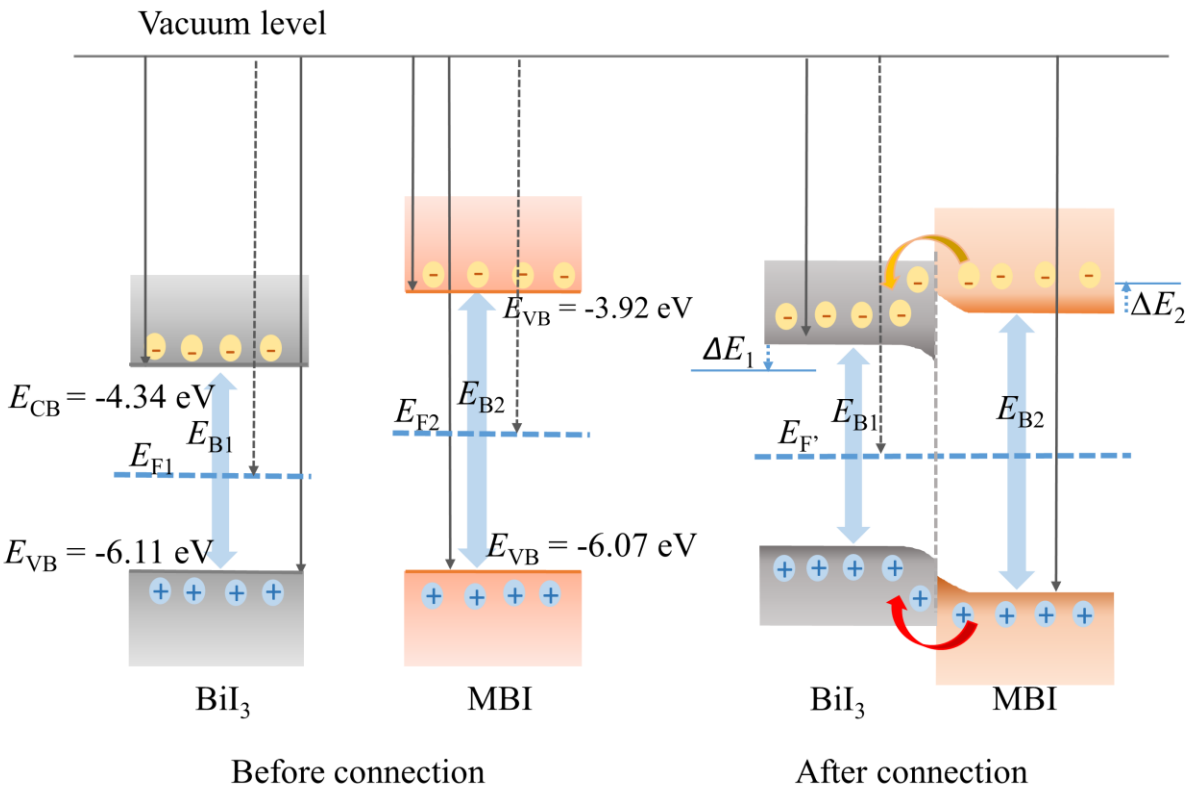

Fig. 8. Schematic of the band bending in the $(BiI_3)_{1-x}(MBI)_x$ composite films. (E_{CB} is the conduction band, E_{VB} is the valence band, E_F is the Fermi level, and ΔE is the bended energy. After connection, E_{F2}-E_{F1}=ΔE_1 +ΔE_2)

Regarding the enhanced photovoltaic performance in the composite solar cells, there are two explanations for it. First, it was attributed to the enhanced crystallization and coverage. As the XRD and SEM results mentioned above, the introduction of MBI significantly improved the BiI_3 crystallization of the $(BiI_3)_{0.8}$ $(MBI)_{0.2}$ films and optimized the film quality, this can effectively reduce the recombination and leakage in the devices. In addition, the series resistance of the

$(BiI_3)_{0.8}(MBI)_{0.2}$ solar cells was relatively lower than others, indicating a more effective charge transport. Second, this phenomenon was attributed to the conduction band bending. As shown in Fig. 8, a conduction band bending occurred at the MBI-BiI_3 interfaces in the $(BiI_3)_{1-x}(MBI)_x$ composites. When two semiconductors are in contact, the electrons of the high conduction band material and that of the low conduction band material can migrate to each other, forming a stable space charge region at the hetero-interface and an upward band-bending at the interface [26]. Therefore, compared with the BiI_3, the conduction band of the $(BiI_3)_{1-x}(MBI)_x$ composite systems became higher. Considering that the conduction band of the pure BiI_3 is approaching to the TiO_2, the band bending can make it easier for the photon-excited electrons from the composite absorbing layers into the TiO_2. Particularly, because the large amount of the MBI nano-sheets in the BiI_3 grains created lots of BiI_3-MBI interfaces, the conduction bands of the whole BiI_3-MBI systems have been improved compared to that of the pure BiI_3 films. Therefore, compared with that of the pure BiI_3 solar cells, the obviously enhanced V_{oc} and *PCE* are observed in the $(BiI_3)_{0.8}(MBI)_{0.2}$ solar cells.

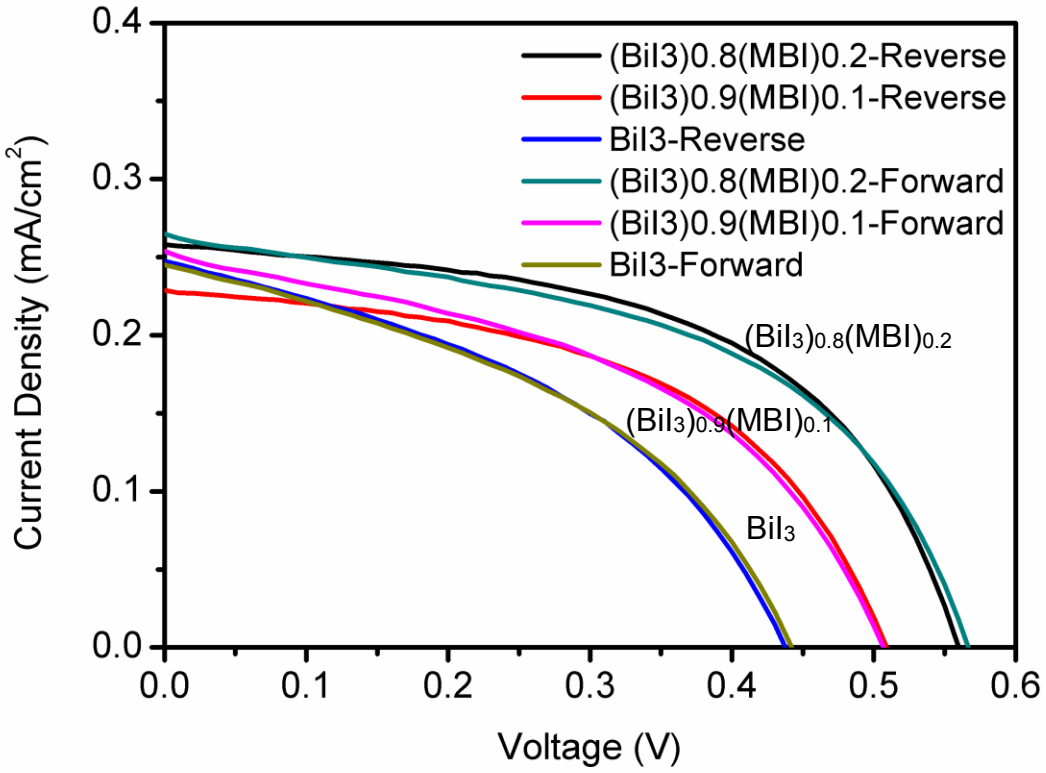

Fig. 9. Comparison on *I-V* characteristics between the forward and reverse scanning of the

$(BiI_3)_{1-x}(MBI)_x$ solar cells.

Besides the V_{oc} and *PCE*, the hysteresis properties of the $(BiI_3)_{1-x}(MBI)_x$ solar cells with the champion performance were also investigated. As showed in Fig. 9, the comparison between the forward and reverse scanning of the solar cells clearly revealed hysteresis-less properties of the $(BiI_3)_{0.8}(MBI)_{0.2}$ composite solar cells. The hysteresis of the perovskite solar cells was thought to relate to the ionic or vacuum defects [30]. Therefore, there are few defects in the $BiI_3)_{0.8}(MBI)_{0.2}$ composite solar cells. And small amount of the MBI performed as the active materials in the composite films. In a word, the multiplicative effects between the BiI_3 and MBI in the composites lead to the enhanced photovoltaic performance of some composite solar devices.

In our study, we also found that some other composite solar cells performed worse than the pure solar cells, such as the low *PCE* and V_{oc} of devices, or the failure of the devices, *e.g.* the$(BiI_3)_{0.5}(MBI)_{0.5}$ solar cells. Taking the XRD and SEM results into the consideration, some failures of the devices in the $(BiI_3)_{0.5}(MBI)_{0.5}$ group are likely due to the amorphous substances in the composite films. And the low *PCE* and V_{oc} of the $(BiI_3)_{0.25}(MBI)_{0.75}$ composite solar cells were more likely owing to the disconnection in the composite films. Regarding the MBI solar cells, considering that the net-work structure lead to the porous structures in the MBI films, it was easy to create some failures of the devices. Moreover, it should also be pointed out that the J_{sc} was low in our study, but the reasons were complicated. One of the reasons can be attributed to the HTM used in the $(BiI_3)_{1-x}(MBI)_x$ devices, because PTAA and PIDT-DFBT have a higher hole mobility than Spiro [11,13]. Another reason of low FF and low V_{oc} is due to the high carrier density of the MBI ($\sim 10^{16}$ cm^{-3}), because the high background carrier densities in the light-absorber can contribute to the bulk recombination and reduce the FFs and V_{oc} [14,31].

4.4 Conclusion

In summary, we have developed a new method to tune the optical properties of lead-free materials by composite the BiI_3 and MBI perovskite for solar cell applications. The active layers of $(BiI_3)_{1-x}(MBI)_x$ showed the gradient in the colors, crystallization and surface morphologies. Meanwhile, they had the same valence bands, but with different absorptions and conduction bands. The introduction of the MBI into BiI_3 resulted in a phenomenon of multi-absorption,

which affected their photovoltaic performance. Compared with the BiI_3 solar cells and MBI perovskite solar cells, some $(BiI_3)_{1-x}(MBI)_x$ composite solar cells exhibited an optimized photovoltaic output. Particularly, compared with the BiI_3 solar cells, the V_{oc} and *PCE* of the $(BiI_3)_{0.8}(MBI)_{0.2}$ composite solar cells were significantly improved from 0.44 to 0.57 V and from 0.045% to 0.076%, respectively. This phenomenon was mainly attributed to two reasons. One is the enhanced BiI_3 crystallization after the small amount introduction of MBI, which effectively reduced the recombination. The other is the band bending at the BiI_3-MBI interfaces in the composites which optimized the energy level matching between the absorbing layers and TiO_2 and lead to the more efficient electron injection from the absorbing layer to TiO_2. Our results indicated that the properly-designed composites of lead-free materials with different absorptions and energy levels can be an effective strategy to design new solar cells.

Reference

[1] A. Kojima, K. Teshima, Y. Shirai, T. Miyasaka, Organometal halide perovskites as visible-light sensitizers for photovoltaic cells, J. Am. Chem. Soc. 2009, **131**, 6050-6051.

[2] Mingzhen Liu, Michael B. Johnston, Henry J. Snaith, Efficient planar heterojunction perovskite solar cells by vapour deposition, Nature 2013, **501**, 395-398.

[3] Wanyi Nie, Hsinhan Tsai, Reza Asadpour, Jean-Christophe Blancon, Amanda J. Neukirch, Gautam Gupta, Jared J. Crochet, Manish Chhowalla, Sergei Tretiak, Muhammad A. Alam, Hsing-Lin Wang, Aditya D. Mohite. Perovskite solar cells with millimeter-scale grains, Science 2015, **347**(6221), 522-525.

[4] National Renewable Energy Laboratory USA, Best research-cell efficiencies. http://www.nrel.gov/ncpv/images/efficiency_chart.jpg, 2017(accessed 17.01.03).

[5] Michael Grätzel, The light and shade of perovskite solar cells, Nature Mater. 2014, **13**, 838 - 842.

[6] Teng Zhang, Haining Chen, Yang Bai, Shuang Xiao, Lei Zhu, Chen Hu, Qingzhong Xue, Shihe Yang, Understanding the relationship between ion migrationand the anomalous hysteresis in high-efficiency perovskite solar cells: A fresh perspective from halide substitution, Nano Energy 2016, **26**, 620-630.

[7] Haining Chen, Xiaoli Zheng, Qiang Li, Yinglong Yang, Shuang Xiao, Chen Hua, Yang Bai, Teng Zhang, Kam Sing Wong, Shihe Yang, Amorphous precursor route to the conformable oriented crystallization of $CH_3NH_3PbBr_3$ in mesoporous scaffolds: Toward efficient and thermally stable carbon-based perovskite solar cells, J. Mater. Chem. A 2016, **4**, 12897-12912.

[8] Haining Chen, Zhanhua Wei, Hexiang He, Xiaoli Zheng, Kam Sing Wong, and Shihe Yang, Solvent engineering boosts the efficiency of paintable carbon-based perovskite solar cells to beyond 14%, Adv. Energy Mater. 2016, **6(8)**, 1502087.

[9] Peng Gao, Michael Grätzel and Mohammad K. Nazeeruddin, Organohalide lead perovskites for photovoltaic applications, Energy Environ. Sci. 2014, **7**, 2448-2463.

[10] R. Nechache, C. Harnagea, S. Li, L. Cardenas, W. Huang, J. Chakrabartty, F. Rosei, Bandgap tuning of multiferroic oxide solar cells, Nat. Photonics 2015, **9**, 61-67.

[11] Anna J. Lehner, Hengbin Wang, Douglas H. Fabini, Christopher D. Liman, Claire-Alice Hébert, Erin E. Perry, Ming Wang, Guillermo C. Bazan, Michael L. Chabinyc and Ram Seshadri,

Electronic structure and photovoltaic application of BiI_3, Appl. Phys. Lett. 2015, **107**, 131109.

[12] Chenghong Nie, Jieyu Chen, Yulong Bai, Shifeng Zhao, The ferroelectric photovoltaic spectral response regulated by band-gap in $BiFe_{0.9}Cr_{0.1}O_3$ films, Mater. Lett. 2016, **175**, 258 - 261.

[13] Byung-Wook Park, Bertrand Philippe, Xiaoliang Zhang, Håkan Rensmo, Gerrit Boschloo, Erik M.J. Johansson, Bismuth based hybrid perovskites $A_3Bi_2I_9$ (*A*: Methylammoniumor cesium) for solar cell application, Adv. Mater. 2015, **27**, 6806-6813.

[14] Trilok Singh, Ashish Kulkarni, Masashi Ikegami, and Tsutomu Miyasaka, Effect of electron transporting layer on bismuth-based lead-free perovskite $(CH_3NH_3)_3Bi_2I_9$ for photovoltaic applications, ACS Appl. Mater. Interfaces 2016, **8**, 14542-14547.

[15] Miaoqiang Lyu, Jung-Ho Yun, Molang Cai, Yalong Jiao, Paul V. Bernhardt, Meng Zhang, Qiong Wang, Aijun Du, Hongxia Wang, Gang Liu, and Lianzhou Wang, Organic-inorganic bismuth(III)-based material: A lead-free, air-stable and solution-processable light-absorber beyond organolead perovskites, Nano Res. 2016, **9**(3), 692-702.

[16] Nikolas J. Podraza, Wei Qiu, Beverly B. Hinojosa, Haixuan Xu, Michael A. Motyka, Simon R. Phillpot, James E. Baciak, Susan Trolier-McKinstry, and Juan C. Nino, Band gap and structure of single crystal BiI_3: Resolving discrepancies in literature, J. Appl. Phys. 2013, **114**, 033110.

[17] M. Ikeda, T. Oka, K. Mori and M. Atsuta, Study of dark current blocking layer for BiI_3 X-ray detector film, Nuclear Science Symposium Conference Record, IEEE, 2004, **7**, 4520-4523.

[18] Riley E. Brandt, Rachel C. Kurchin, Robert L. Z. Hoye, Jeremy R. Poindexter, Mark W. B. Wilson, Soumitra Sulekar, Frances Lenahan, Patricia X. T. Yen, Vladan Stevanović, Juan C. Nino, Moungi G. Bawendi, and Tonio Buonassisi, Investigation of bismuth triiodide (BiI_3) for photovoltaic applications, J. Phys. Chem. Lett. 2015, **6**, 4297-4302.

[19] Mutsumi Kimura, Hirotaka Nomoto, Naruhiko Masaki, Shogo Mori, Dye molecules for simple co-sensitization process: Fabrication of mixed-dye-sensitized solar cells, Angew. Chem. 2012, **124**, 4447-4450.

[20] Tao-Tao Zhuang, Yan Liu, Yi Li, Yuan Zhao, Liang Wu, Jun Jiang, and Shu-Hong Yu, Integration of semiconducting sulfides for full-spectrum solar energy absorption and efficient charge separation, Angew. Chem. Int. Ed. 2016, **55**, 6396 -6400.

[21] Zhao-Kui Wang, Meng Li, Ying-Guo Yang, Yun Hu, Heng Ma, Xing-Yu Gao, and Liang-

Sheng Liao, High efficiency Pb-In binary metal perovskite solar cells. Adv. Mater. 2016, 28(31), 00626.

[22] Huawei Zhou, Yantao Shi, Qingshun Dong, Hong Zhang, Yujin Xing, Kai Wang, Yi Du, and Tingli Ma, Hole-conductor-free, metal-electrode-free $TiO_2/CH_3NH_3PbI_3$ heterojunction solar cells based on a low-temperature carbon electrode. J. Phys. Chem. Lett. 2014, **5**, 3241−3246.

[23] Chunrui Wang, Qing Yang, Kaibin Tang, and Yitai Qian, Preparation and vibrational properties of BiI_3 nanocrystals, Chem. Lett. 2001, **30** (2), 154-155.

[24] N. Kubota, Effect of impurities on the growth kinetics of crystals, Cryst. Res. Technol. 2001, **36**(8-10), 749-769.

[25] Jeong-Hyeok Im, In-Hyuk Jang, Norman Pellet, Michael Grätzel & Nam-Gyu Park, Growth of $CH_3NH_3PbI_3$ cuboids with controlled size for high-efficiency perovskite solar cells, Nat. Nanotechnol. 2014, **9**, 927-932.

[26] Kai Zhu, Nathan R. Neale, Alexander Miedaner, and Arthur J. Frank, Enhanced charge-collection efficiencies and light scattering in dye-sensitized solar cells Using Oriented TiO_2 Nanotubes Arrays, Nano Lett. 2007, **7**(1), 69-74.

[27] S. Kondo, A. Kato, and T. Saito, Optical absorption of BiI_3 clusters embedded in CdI_2 films, Phys. Stat. Sol. (a) **182** (2000), 661-668.

[28] J. Tauc, R. Grigorovici, A. Vancu, Optical properties and electronic structure of amorphous germanium, Phys. Stat. Sol. B 1966, **15**, 627-637.

[29] Le Thi Quynh, Chien Nguyen Van, Yugandhar Bitla, Jhih-Wei Chen, Thi Hien Do, Wen-Yen Tzeng, Sheng-Chieh Liao, Kai-An Tsai, Yi-Chun Chen, Chun-Lin Wu, Chih-Huang Lai, Chih-Wei Luo, Yung-Jung Hsu, and Ying-Hao Chu, Self-assembled $BiFeO_3$-ε-Fe_2O_3 vertical heteroepitaxy for visible light photoelectrochemistry, Adv. Energy Mater. 2016, **6(18)**,1600686.

[30] W. Tress, N. Marinova, T. Moehl, S.M. Zakeeruddin, M.K. Nazeeruddin and M. Gratzel, Understanding the rate-dependent *J-V* hysteresis, slow time component, and aging in $CH_3NH_3PbI_3$ perovskite solar cells: the role of a compensated electric field. Energy Environ. Sci. 2015, **8**, 995-1004.

[31] C.C. Stoumpos, C.D. Malliakas, M.G. Kanatzidis, Semiconducting tin and lead iodide perovskites with organic cations: phase transitions, high mobilities, and near-infrared photoluminescent properties. Inorg. Chem. 2013, **52**, 9019−9038.

Chapter 5. Investigation on structures, bandgaps and electronic structures of lead-free La_2NiMnO_6 double perovskites for potential application of solar cell

5.1 Introduction

Hybrid organic-inorganic perovskite solar cells (PSCs) have experienced a rapid development since perovskite materials were first applied to replace organic dyes in solar cells in 2009 [1]. Their power conversion efficiency has reached 22.1% to date, making them comparable to traditional silicon solar cells [1-3]. The extraordinary high conversion efficiency of hybrid PSCs can be attributed to the excellent optical properties of halide perovskites (ABX_3-structured), e.g. the typical methylammonium lead iodide perovskite ($CH_3NH_3PbI_3$) usually has a suitable bandgap of 1.5 eV, a large absorption coefficient up to 10^5 cm^{-1}, a long electron-hole diffusion length up to 175 μm [3], as well as the bipolar carrier transport ability [4,5]. However, although the halide perovskite materials have exhibited many merits in the current PSCs, they are still facing several drawbacks which may block their future practical wide range application. One of them is the degradation of the halide perovskite materials as well as the poor long-term stability of devices. This comes from the *A*-site of methylammonium organic group in the ABX_3-structure of the hybrid perovskites. Another problem is the lead pollution from the *B*-site ion. As we know, lead is a heavy metal element and it will do harm to our environment and human health [4,5]. Therefore, the development of environmental-friendly and stable perovskite materials are required to overcome these drawbacks. Previous work suggested that multiferroic perovskite oxides might be potential alternatives for solar cell application [5].

The multiferroic perovskite oxides, such as $[KNbO_3]_{1-x}[BaNi_{1/2}Nb_{1/2}O_{3-\delta}]_x$, $BiFeO_3$ and Bi_2CrFeO_6, are expected to replace the lead halide perovskites in perovskite solar cells [6-10]. However, the bandgap of $BiFeO_3$ is too large to absorb the visible lights [9]. Although the bandgap of $[KNbO_3]_{1-x}$ $[BaNi_{1/2}Nb_{1/2}O_{3-\delta}]_x$ has been narrowed, it is still difficult to apply it into the solar cells because there are too many defects in it [10]. For Bi_2CrFeO_6 perovskites, it was reported they possessed experimental bandgaps of 1.6 -1.9 eV, very suitable for visible light

harvesting. And the solar cells with the structure of ITO/ Bi_2CrFeO_6/Nb-doped $SrTiO_3$ were also fabricated by R. Nechache *et al.*, and they have achieved a high power conversion efficiency of 8.1%. Unfortunately, the disadvantage of Bi_2CrFeO_6 perovskites is also apparent. First, the preparation of Bi_2CrFeO_6 perovskites needed an expensive physical vapor deposition (usually pulse laser deposition). Second, the experimental condition to deposit the Bi_2CrFeO_6 films was quite complicated. Therefore, it is hard to achieve higher performance solar cells and not suitable for mass production process [12,13]. Some other alternatives must be developed to overcome these disadvantages.

Recently, the double perovskites La_2NiMnO_6 are becoming attractive materials. Kitamura *et al.* reported that these materials have an experimental bandgap of 1.5 eV [14]. Compared with Bi_2CrFeO_6 and $[KNbO_3]_{1-x}[BaNi_{1/2}Nb_{1/2}O_{3-\delta}]_x$, La_2NiMnO_6 double perovskites can be easily synthesized by a chemical method [15]. At the same time, Dass and Sun *et al*. reported that different synthesis conditions resulted in La_2NiMnO_6 with different crystal structures, and they found that the crystal structures strongly influenced their physical properties, such as dielectric properties and magnetic properties [15,16]. However, so far there is little study on the electronic properties of different structured La_2NiMnO_6, such as *B*-site and phase effects on bandgaps, electronic structures, which would be key factors influencing their solar cell application.

In this work, we tried to synthesize the La_2NiMnO_6 materials by the Pechini method [16], and investigated their crystal structures by X-Ray diffraction and X-ray photoelectron spectroscopy. In order to further explore their potential application for perovskite solar cells, we also carried out the theoretical investigation of bandgaps and electronic structures based on the density functional theory. The results of experimental and theoretical study revealed that the monoclinic La_2NiMnO_6 double perovskite is a better candidate than the rhombohedral La_2NiMnO_6 for the visible light harvesting.

5.2 Experimental procedure

5.2.1 Preparation of materials

Stoichiometric lanthanum acetate (99.9%, Alfa Aesar), nickel acetate (98.0%, Wako Pure Chemical) and manganese acetate (99.0%, Wako Pure Chemical) were mixed in the citric acid/ ethylene glycol solution as the precursor. The presursor was heated at 120 °C for 4 hours to form

a dry-gel. And then, the dry-gel was pyrolized to obtain a homogenous powder at 400 °C for 5 hours. The powder was ground and heated in a tube furnace under different synthesizing conditions. One sample was prepared in the air at 600 °C for 10 hours with a heating rate 5 °C/min, labeled as LNM600. The other sample was rapidly annealed in a tube furnace under oxygen atmosphere at 900 °C for 10 hours, labeled as LNM900.

5.2.2 Characterization of materials

The X-ray diffracting patterns were measured from 15 ° to 75 ° at a scanning speed of 0.01 °/s using a X-ray diffractometer (XRD, RINT 2100, Rigaku) with Cu Kα radiation (λ = 1. 54056 Å). The microstructure and chemical composition were characterized by a field-emission scanning electron microscope (FE-SEM, S5200, Hitachi) with an energy dispersive X-ray spectroscopy (EDX). The valence state of Ni and Mn elements was determined by the X-ray photoelectron spectroscopy (XPS, AXIS-HS, KRATOS). The optical properties of the products was determined using a UV-VIS-NIR spectrophotometer with an integrator (V-670, JASSCO) by diffuse reflectance spectra, and the bandgaps were calculated with Tauc Plot. The valence band of the samples was evaluated by an ionization energy measuring device through photoelectron yield spectroscopy (PYS, KV205-HK, Bunkoukeiki).

5.2.3 Theoretical calculations

Quantum ESPRESSO simulation package based on the density functional theory was introduced for all calculations using plane-wave basis sets [17,18]. The generalized gradient approximation (GGA) with the Perdew-Burke-Ernzerhof (PBE) functional had been considered for the exchange-correlation effects [19]. Projector augmented wave (PAW) was used to describe the electron-ion interactions and 40 Ry was set for the cutoffs of plane-wave basis sets. The ground-state configurations were determined by the 4×4×4 Monkhorst-Pack *k*-mesh for the self-consistent calculations and the density of states (DOS) calculations were carried out by a denser grid. Before electronic and optical properties calculations, the atomic positions and lattice vectors were fully relaxed. The bandgaps were seriously underestimated by the DFT calculation with respect to the transition metal oxides because we ignored the strong on-site Coulomb interactions between localized electrons in this case. GGA+*U* method is an effective method to

offset this underestimation, because it adds an orbital-dependent term to reflect the exchange and correlation potentials. In our calculation, the U_{eff} = 3 eV for Ni 3*d* and Mn 3*d* orbitals was set as Ref. [20].

5.3 Results and discussion

5.3.1 Structural characterization

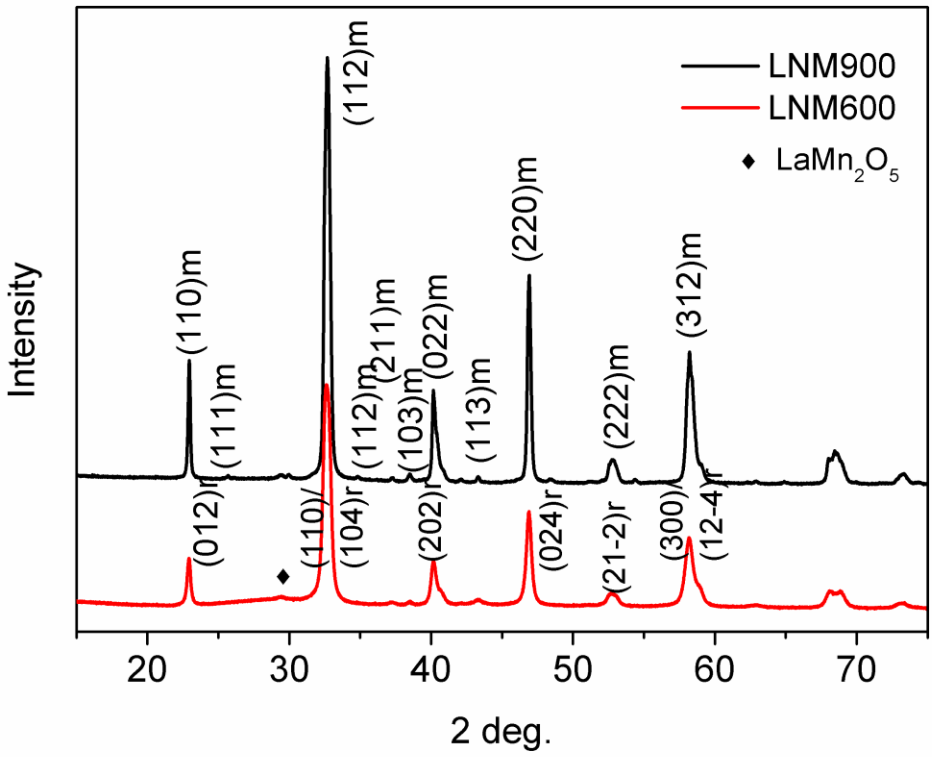

Fig. 1. XRD patterns of the samples LNM600 and LNM900.

The samples formed under different conditions showed different appearances. The color of the sample LNM600 looked dark black, whereas, the sample LNM900 was gray black. These results were in agreement with that reported by Dass [16]. Fig. 1 showed the powder XRD patterns of the two samples. It indicated that the sample LNM600 was a rhombohedral phase of La_2NiMnO_6 (PDF 01-072-8297) with the space group *R*-3. For the XRD pattern of LNM900, there was a slight location difference of peaks at around 32° and the existence of (111) at 25.65 °, suggesting

that it might be orthorhombic phase with the space group *Pbnm* (PDF 01-075-2899) or monoclinic with the space group $P2_1/n$ (PDF 01-072-7793). Regarding the sample LNM900, it was reported that the monoclinic La_2NiMnO_6 was *B*-site ordered, whereas the orthorhombic La_2NiMnO_6 was *B*-site disordered [15,16]. The temperature to synthesize disordered La_2NiMnO_6 was lower than that to prepare ordered La_2NiMnO_6. When rapid high-temperature annealing was applied, it could conquer the nucleation of disordered perovskite and benefit the formation of *B*-site ordered double perovskites [15]. Hence, our XRD results suggested that the sample LNM900 was the *B*-site ordered monoclinic phase with the space group $P2_1/n$. In addition, small amount of impurity was also found in LNM900. This is attributed to the existence of $LaMn_2O_5$ (PDF 00-052-1095).

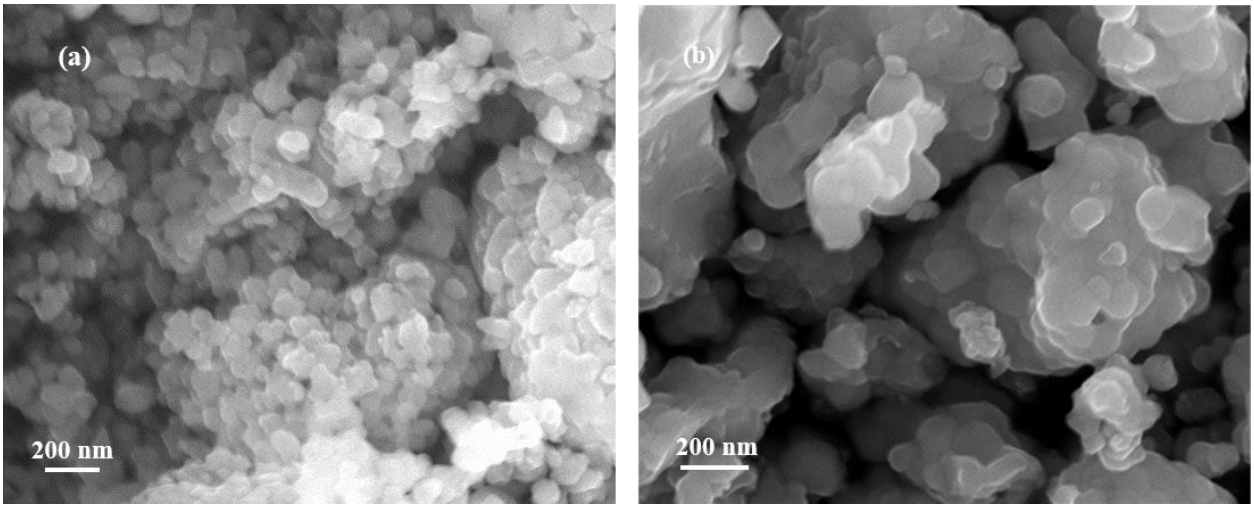

Fig. 2. FE-SEM images of the La_2NiMnO_6 powders: a) LNM600; b) LNM900.

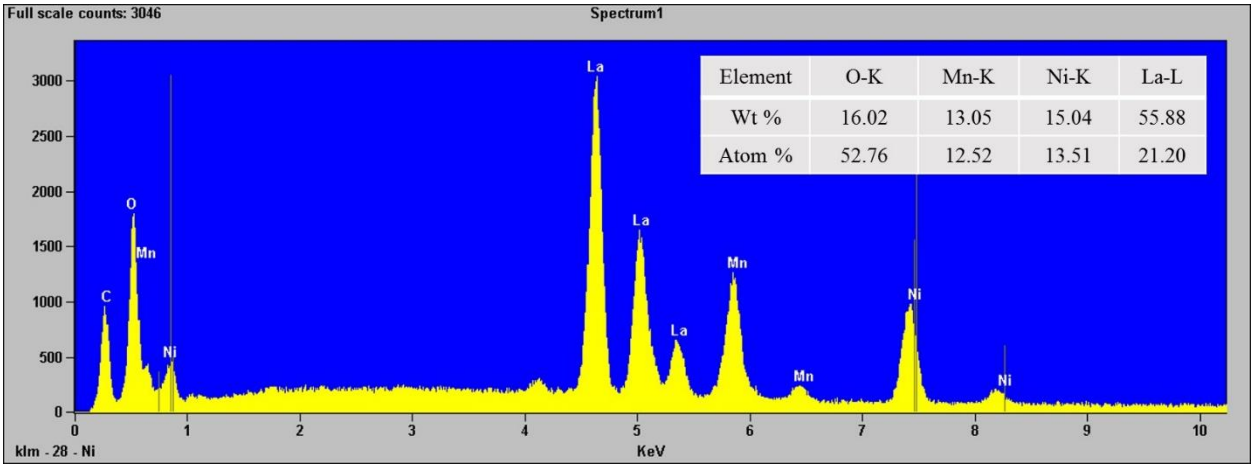

Fig. 3. EDX patterns and results from the sample LNM900.

Fig. 2 showed the SEM images of the sample LNM600 and LNM900. Homogeneous nano-particles have been found both in LNM600 and LNM900. However, the higher synthesizing temperature attributed to the larger particle size. The particle size of LNM600 was ca. 50 nm and that of LNM900 was ca. 500 nm. The aggregation of particles was also found in LNM900 because high annealing temperature favored the growth up of particles. Further EDX results from the sample LNM900 were presented in Fig. 3. It confirmed that Mn, La and Ni elements existed in the sample. And the molar ratio of Mn and Ni in the prepared sample was approximately 1:1.

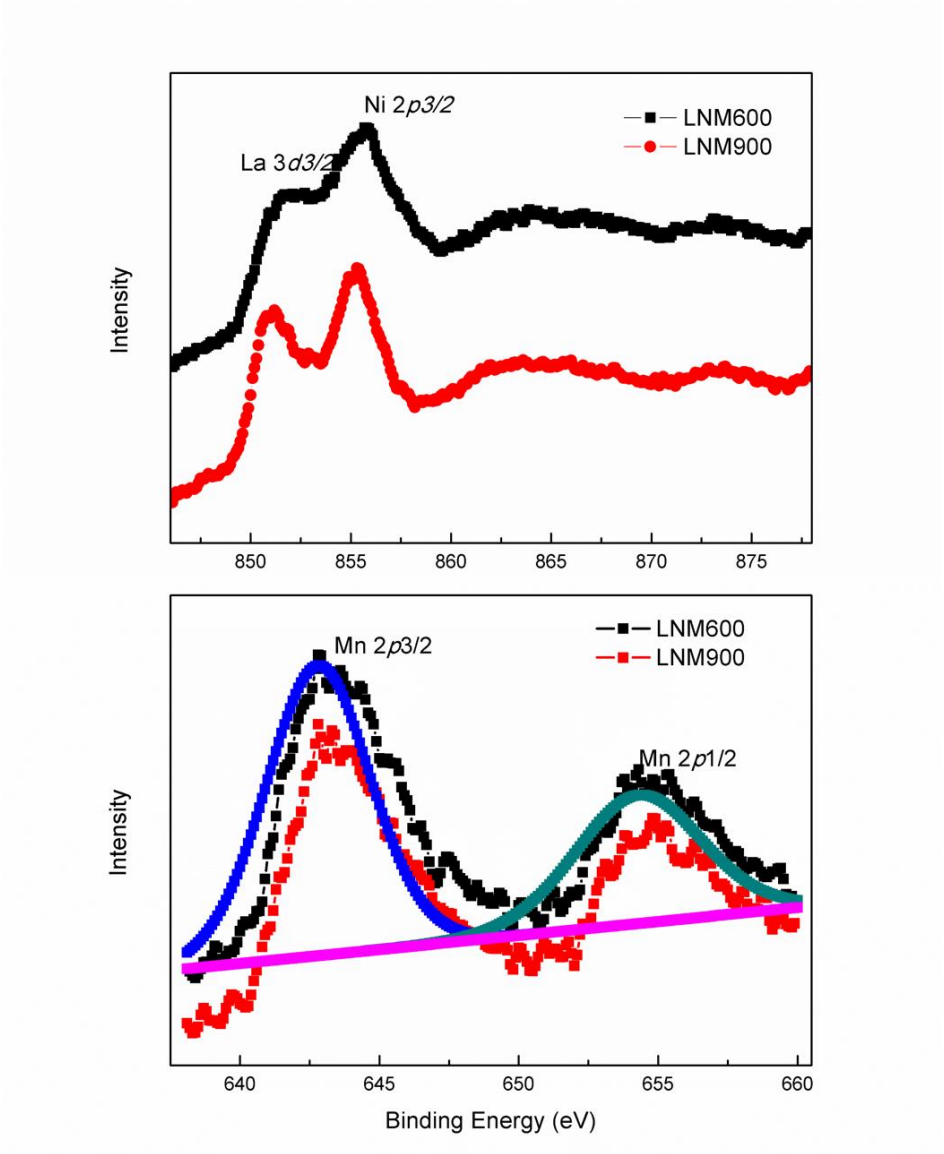

Fig. 4. XPS patterns of the samples LNM600 and LNM900. (a) Ni 2*p*→3*d* XPS spectrum, (b)

Mn 2*p*→3*d* XPS spectrum.

Valence states of elements are key points influenced the physical properties of perovskites. Fig. 4(a) and 4(b) showed the XPS patterns of LNM600 and LNM900 to determine the valence state of the *B*-site elements. It was difficult to distinguish Ni^{2+} from Ni^{3+} in the weak peaks at ca. 870 eV (Ni $2p_{1/2}$) of the X-ray absorbing spectrum results [14]. Moreover, the characteristic peaks of the La element were close to that of the Ni element. Therefore, it was impossible to directly determine the valence state of Ni in our results. Luckily, the sharp structures from 640 eV to 645 eV of Mn $2p_{3/2}$ are reliable benchmarks to identify the Mn state because few other elements smeared them [14, 21]. The peak structure in this arrangement strongly depended on the multiplet structures related to the hybridization with the O 2*p* ligands, as well as the Mn 3*d*-3*d* and 2*p*-3*d* Coulomb and exchange interactions [14,15]. The split structures of peaks from 640 eV to 645 eV were thought as a symbol of the Mn^{4+} state. However, None of them were observed in LNM600 nor LNM900. In contrast, the structure was in agreement with that of Mn state in $LaMnO_3$ as reported [23]. Therefore, it can be deduced that the Mn^{3+} state was likely dominant in our samples. Meanwhile, in order to maintain a state of neutral charge, it can be concluded that both LNM600 and LNM900 were mainly with the *B*-site element of Ni^{3+} formal oxidation-state [21]. To sum up, the XRD and XPS results suggested the sample LNM600 was rhombothedral with the *B*-site of Ni^{3+}/Mn^{3+} and LNM900 was monoclinic with the *B*-site of Ni^{3+}/Mn^{3+}.

5.3.2 UV-vis optical absorption properties and electronic structure

Fig. 5 showed the UV-visible diffuse reflectance spectra results of the La_2NiMnO_6 powders. The reflectance of the sample LNM600 was near infrared range, and the bandgap of LNM600 determined from the *Tauc plot* is ca. 1.2 eV. Whereas, the the band of the sample LNM900 deduced was ca. 1.4 eV. The results were very close to that of the La_2NiMnO_6 film as reported by Kitamura [14]. Compared with the single perovksite $LaMnO_3$ whose experimental bandgap of 1.7 eV and theoretical bandgap of 2.0 eV [22], it can be seen that both LNM600 and LNM900 showed much narrower bandgaps. This phenomenon can be attributed to the higher octahedrons distortion in La_2NiMnO_6 crystal after the introduction of Ni^{3+} into the *B*-site [21]. The bandgap difference of 0.2 eV between LNM600 and LNM900 might be attributed to the larger crystal

distortion of *R-3* phase, which might result in higher local energy [16]. The more detailed contributions of Mn and Ni on the bandgap were discussed in the following calculation.

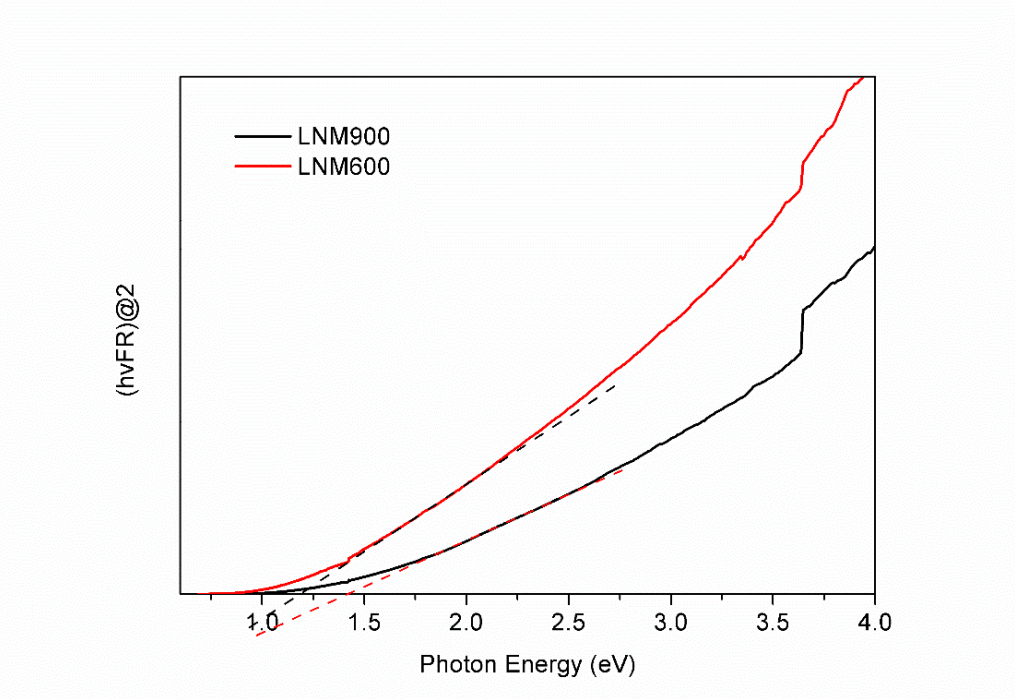

Fig. 5. UV-Vis diffuse reflectance spectra of LNM600 and LNM900 after *K-M* conversion and *Tauc Plot* treatment.

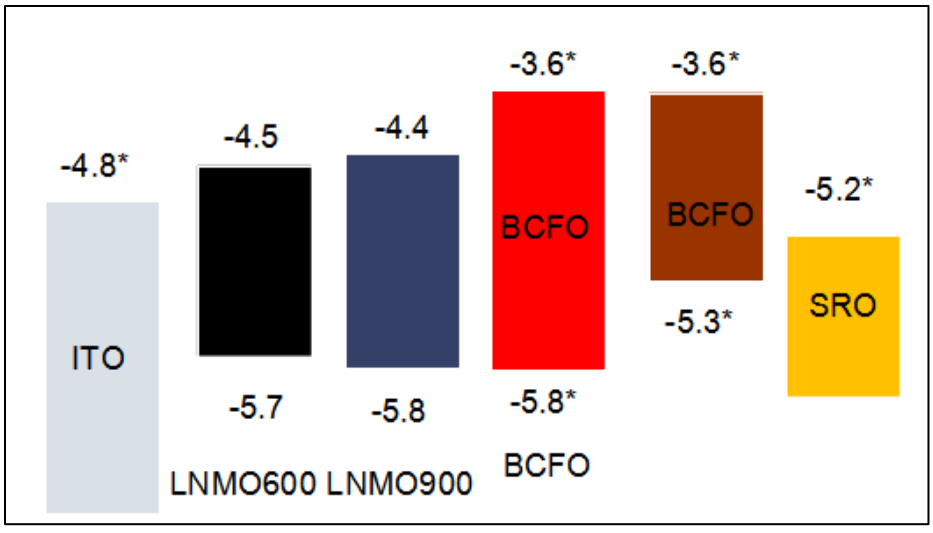

Fig. 6. Energy band diagrams of LNM600, LNM900 and BCFO materials *et al.* reported. (* referred to Ref.[6])

Energy levels of materials is very important to design solar cells. To understand the energy level of La_2NiMnO_6, photoelectron yield spectroscopy was applied to evaluate the valence bands of the samples. The results showed that the experimental valence bands of LNM600 and LNM900 were -5.7 eV and -5.8 eV, respectively, very close to each other. As discussed above, there are little difference of the valence states of *B*-site ion in the sample LNM600 and LNM900. Thus, the difference of valence band might result from the crystal structures of the La_2NiMnO_6. For La_2NiMnO_6 with *B*-site of Ni^{2+}/Mn^{4+}, the maximum valence band was considered to be a state derived from Mn 3*d* [14]. However, to date there is no report on this for La_2NiMnO_6 with *B*-site of Ni^{3+}/Mn^{3+}. We will try to discuss it in the following calculations in our work. Based on the bandgaps and valence states, an energy level diagram was drawn as in Fig. 6. The conduction bands of LNM600 and LNM900 are higher than that of ITO and $SrRuO_3$ thin films. The energy level difference from monoclinic LNM900 to $SrRuO_3$ was 0.8 eV, whereas the difference was 0.7 eV for that of rhombothedral LNM600 to $SrRuO_3$. Considering that $SrRuO_3$ is a suitable electron conductor [24], the photon-excited electron in La_2NiMnO_6 could be injected into $SrRuO_3$ layer and form a Schottky junction. As mentioned above, although there might be lots of defects in Bi_2CrFeO_6 layers, the simple Schottky solar cells with the structure of ITO/Bi_2CrFeO_6 /$SrRuO_3$ reached a high power conversion efficiency [6]. Therefore, it is anticipated that the La_2NiMnO_6 perovskites could replace Bi_2CrFeO_6 to fabricate lead-free perovksite solar cells. Furthermore, from the views of the energy level matching and bandgaps, it can be deduced that the monoclinic La_2NiMnO_6 would be a better candidate than the rhombothedral La_2NiMnO_6 for solar cell applications.

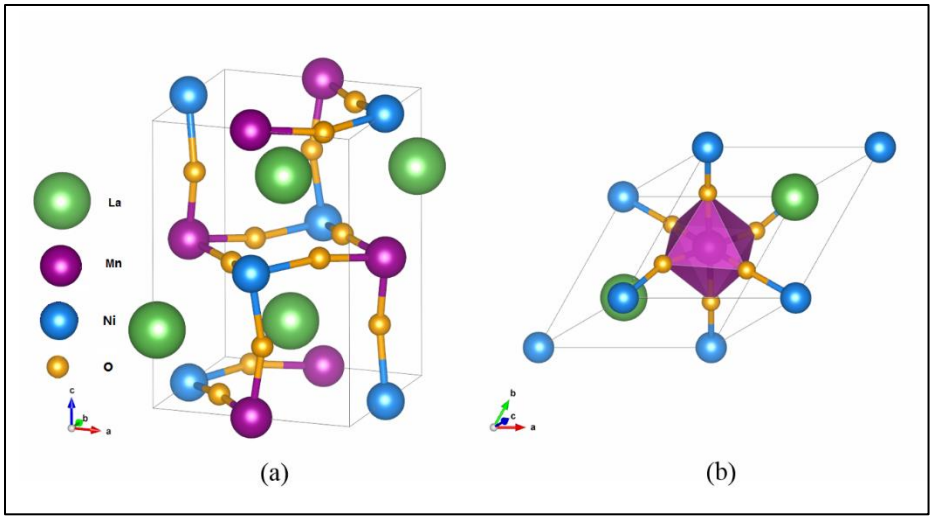

Fig. 7. Projected density of states of La_2NiMnO_6 with the space group *P* 21/n and *R*-3.

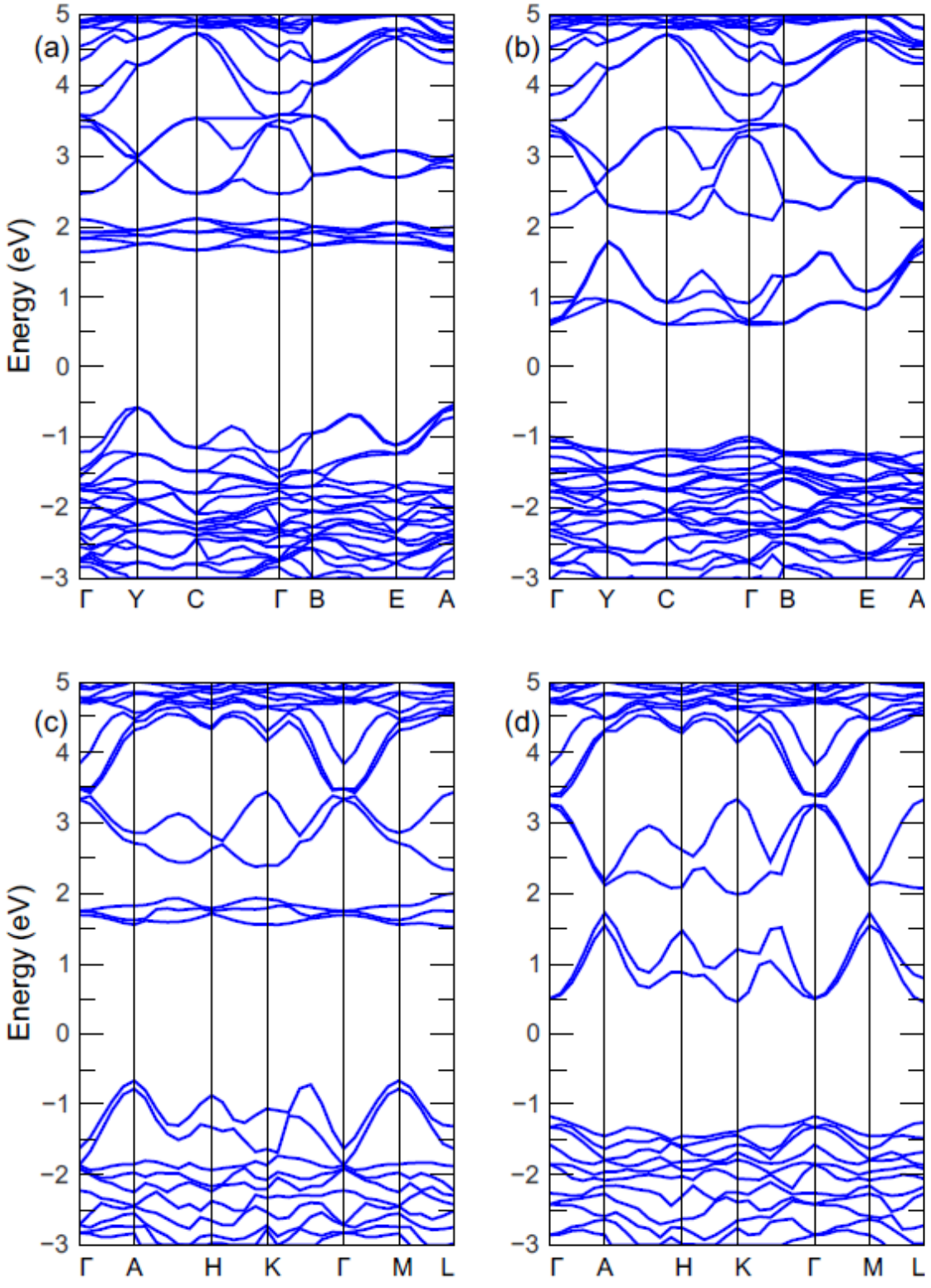

Fig. 8. Band structures of La_2NiMnO_6, (a) majority spin of *P* 21/n state; (b) minority spin of *P* 21/n state; (c) majority spin of *R* -3 state; (d) minority spin of *R* -3 state.

La_2NiMnO_6 with different structures have showed different optical properties. However, the origin for this phenomenon was confused. In order to understand the phase effects on electronic properties of La_2NiMnO_6 perovskites, DFT calculation was introduced to investigate their bandgaps and electronic structures. At the beginning, as listed in Table 1, Broyden-Fletcher-Goldfarb-Shanno algorithm was used to optimize two different geometrical structures of the La_2NiMnO_6. According to the valence states and crystal structures mentioned above, La_2NiMnO_6 of two different phases were optimized under PBE-GGA level. Their geometrical structures are shown in Fig. 7 [25]. The lattice parameters of ferromagnetic state calculated in $P2_1/n$ and *R*-3 phases agreed well with the experimental results [26]. However, the distance of central Ni atoms with the corner O atoms in the octahedron was slightly longer than that of Mn with the O atoms, suggesting a higher distortion in crystal structure when Mn was half-replaced by Ni in $LaMnO_3$. Meanwhile, the optimized angle of Ni-O-Mn in the monoclinic La_2NiMnO_6 was larger than that of the rhombohedral La_2NiMnO_6. It indicated that there was a smaller distortion of crystal structure in the $P2_1/n$ La_2NiMnO_6, which might be an explanation for the larger bandgap of the monoclinic.

Table 1. Parameters for crystal structures of La_2NiMnO_6 with two different phases.

	P 21/n		*R*-3	
	Exp.[a]	Cal.	Exp.[a]	Cal.
a	5.467	5.436	5.475	5.359
b	5.51	5.411		
c	7.751	7.653	60.67	61.48
distance (Ni-O)				
x-y	2.011	2.019	2.008	2.013
	1.976	2.017		
z	2.016	2.02		
distance (Mn-O)				
x-y	1.983	1.889	1.927	1.887
	1.889	1.89		
z	1.908	1.889		
angle (Ni-O-Mn)				

x-y	168.92	157.55	162.79	158.64
	157.21	158.09		
z	161.85	156.37		

[a] reference 26.

The optimized crystal structures was applied to calculate the band structures and density of states of La_2NiMnO_6. The theoretical band structures near the Fermi energy level along the high symmetry *k*-points are depicted in Fig. 8 for $P2_1/n$ and *R*-3 phases, respectively. The general band structures at the conduction band minimum (CBM) and valence band maximum (VBM) are similar for the $P2_1/n$ La_2NiMnO_6 and the *R*-3 La_2NiMnO_6 in our calculated results. The bandgap of the $P2_1/n$ La_2NiMnO_6 is 1.133 eV, whereas the bandgap of the *R*-3 La_2NiMnO_6 is slightly smaller to 1.109 eV. The calculated bandgaps are corresponding to, but a little lower than the experimental results in our study.

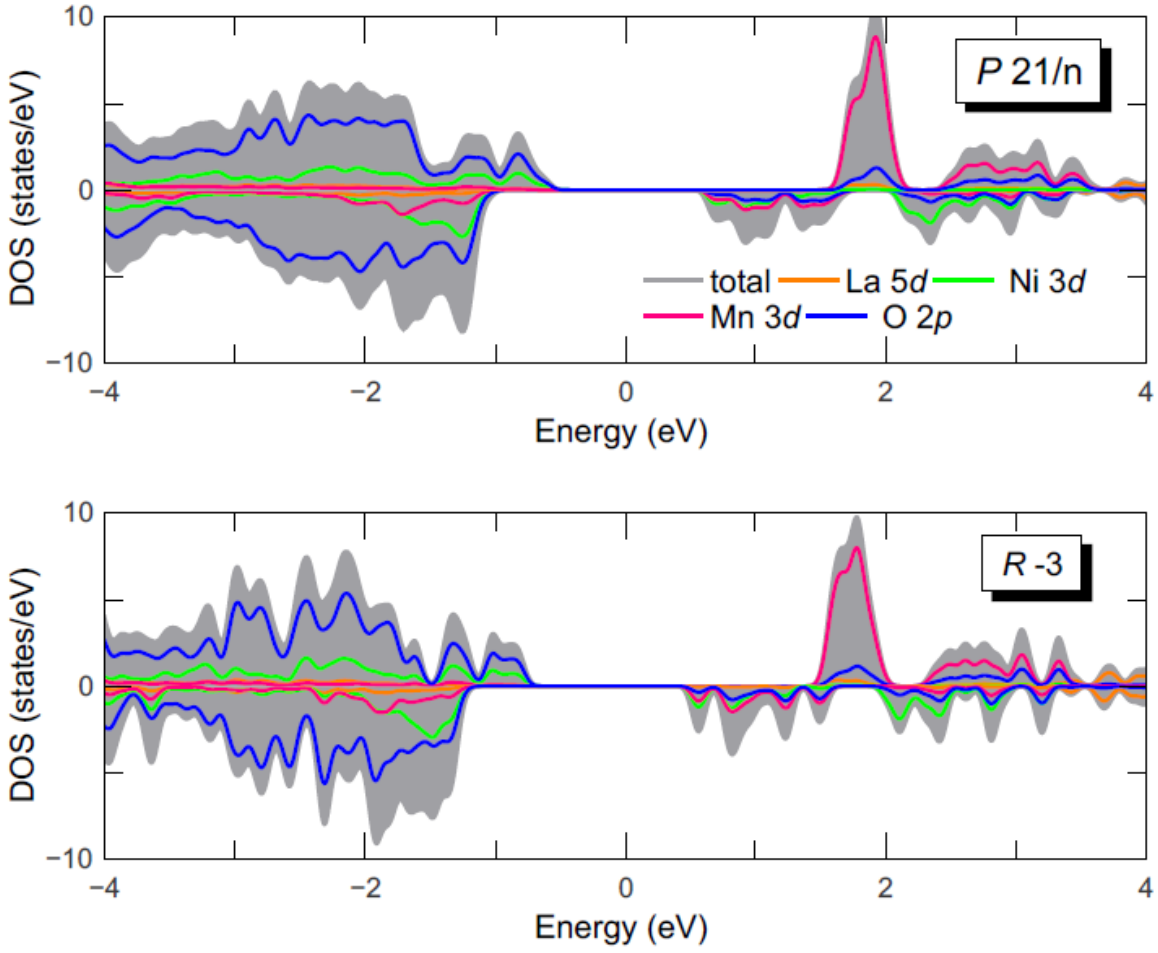

Fig. 9. Electronic structures of La_2NiMnO_6, (up): *P* 21/n; (down): *R*-3.

In order to further understand the electronic structures, the total density and partial density of the states of La_2NiMnO_6 double perovskites were calculated, and the results were shown in Fig. 9. It can be seen that the valence band maximum was mainly attributed to the interaction of Ni 3*d* orbitals as well as O 2*p* orbitals in both $P2_1/n$ La_2NiMnO_6 and *R*-3 La_2NiMnO_6. Accordingly, with a valence band originated from O 2*p* orbitals, the valence bands of La_2NiMnO_6 double perovskites have increased. Simultaneously, the bottom of the conduction band was primarily attributed to the hybridization between O 2*p* and Mn 3*d* orbitals. Consequently, compared with the single perovskite $LaMnO_3$, the bandgaps of double perovskite La_2NiMnO_6 were narrowed, and this mainly come from the improvement of the valence band [22]. Nevertheless, it is worthwhile pointing out that at the top of the valance band and the bottom of the conduction band in the minority-spin configuration, there was the hybridization between not only Ni 3*d,* but also Mn 3*d* orbitals with O 2*p* orbitals. Therefore, the results of experimental and theoretical study revealed that the *B*-site substitution in single perovskite oxides is actually a feasible method to tune the bandgap and electronic structures of perovskite oxides, and the crystal structures can strongly influence their optical properties [27].

5.4 Conclusion

Homogenous rhombohedral and monoclinic La_2NiMnO_6 double perovskites were synthesized by the Pechini Method under different conditions. XPS analysis reveals that Ni^{3+} and Mn^{3+} states dominate both in monoclinic and rhombohedral La_2NiMnO_6. UV-Vis diffuse reflectance spectra reveals that the bandgap of the monoclinic La_2NiMnO_6 is ca. 1.4 eV, and the bandgap of the rhombothedral La_2NiMnO_6 is ca. 1.2 eV from Tauc plot. The experimental valence bands of the monoclinic La_2NiMnO_6 and the rhombothedral La_2NiMnO_6 are -5.8 eV and -5.7 eV, respectively. Further results from the density function theory calculation demonstrate that the theoretical bandgap of monoclinic La_2NiMnO_6 is 1.133 eV and that of rhombothedral La_2NiMnO_6 perovskites is 1.109 eV. The small difference of the bandgaps comes from the larger distortion of *B*-site in the rhombothedral crystal structure than in the monoclinic structure. Moreover, the calculation demonstrates that the top of valence band of these La_2NiMnO_6 is mainly attributed to the interaction of Ni 3*d* orbitals and O 2*p* orbitals, whereas the bottom of the conduction band

primarily comes from the hybridization between Mn 3*d* and O 2*p* orbitals. The energy level diagram drawn from the experimental data suggests that the monoclinic La_2NiMnO_6 would be a better candidate for light harvesting than rhombohedral La_2NiMnO_6.

References

[1] A. Kojima, K. Teshima, Y. Shirai, T. Miyasaka, Organometal halide perovskites as visible-light sensitizers for photovoltaic cells, J. Am. Chem. Soc. 2009, **131**, 6050-6051.

[2] Woon Seok Yang, Jun Hong Noh, Nam Joong Jeon, Young Chan Kim, High-performance photovoltaic perovskite layers fabricated through intramolecular exchange, Science 2015, **348**, 1234-1237.

[3] Qingfeng Dong, Yanjun Fang, Yuchuan Shao, Padhraic Mulligan, Jie Qiu, Lei Cao, Jinsong Huang, Electron-hole diffusion lengths > 175 μm in solution-grown $CH_3NH_3PbI_3$ single crystals, Science 2015, **347**, 967-970.

[4] S. Kazim, M.K. Nazeeruddin, M. Grätzel, S. Ahmad, Perovskite as light harvester: A game changer in photovoltaics, Angew. Chem. Int. Ed. 2014, **53**, 2812-2824.

[5] Peng Gao, Michael Grätzel and Mohammad K. Nazeeruddin, Organohalide lead perovskites for photovoltaic applications, Energy Environ. Sci. 2014, **7**, 2448-2463.

[6] R. Nechache, C. Harnagea, S. Li, L. Cardenas, W. Huang, J. Chakrabartty & F. Rosei, Bandgap tuning of multiferroic oxide solar cells, Nat. Photonics 2015, **9**, 61-67.

[7] ZHAO Qing-xun, WEN Meng-xian, WANG Shu-biao, GUAN Li, LIU Bao-ting, Electronic structures and optical properties of $BiFeO_3$ and Bi_2FeCrO_6, J. Synth. Cryst. 2008, **37** (6), 1390-139.

[8] R. Nechache, C. Harnagea, S. Licoccia, E. Traversa, A. Ruediger, A. Pignolet, and F. Rosei, Photovoltaic properties of Bi_2FeCrO_6 epitaxial thin films, Appl. Phys. Lett. 2011, **98**, 202902.

[9] T. Choi, S. Lee, Y. Choi, V. Kiryukhin, S.W. Cheong, Switchable ferroelectric diode and photovoltaic effect in $BiFeO_3$, Science 2009, **324**, 63-66.

[10] Ilya Grinberg, D. Vincent West, Maria Torres, Gaoyang Gou, David M. Stein, Liyan Wu, Guannan Chen, Eric M. Gallo, Andrew R. Akbashev, Peter K. Davies, Jonathan E. Spanier, Andrew M. Rappe, Perovskite oxides for visible-light-absorbing ferroelectric and photovoltaic materials, Nature 2013, **503**, 509-512.

[11] Riad Nechache, Catalin Harnagea, Louis-Philippe Carignan, Olivier Gautreau, Lucian Pintilie, Mangala P. Singh, David Ménard, Patrick Fournier, Marin Alexe, and Alain Pignolet,

Epitaxial thin films of the multiferroic double perovskite Bi_2FeCrO_6 grown on (100)-oriented $SrTiO_3$ substrates: Growth, characterization, and optimization, J. Appl. Phys. 2009, **105**, 061621.

[12] Sushil K. Singh, S. Shanthy, and H. Ishiwara, Reduced leakage current in $BiFeO_3$-$BiCrO_3$ nanocomposite films formed by chemical solution deposition, J. Appl. Phys. 2010, **108**, 054102.

[13] Riad Nechache, Catalin Harnagea, Louis-Philippe Carignan, Olivier Gautreau, Lucian Pintilie, Mangala P. Singh, David Ménard, Patrick Fournier, Marin Alexe, and Alain Pignolet, Epitaxial thin films of the multiferroic double perovskite Bi_2FeCrO_6 grown on (100)-oriented $SrTiO_3$ substrates: Growth, characterization, and optimization, J. Appl. Phys. 2009, **105**, 061621.

[14] M. Kitamura, I. Ohkubo, M. Matsunami, K. Horiba, H. Kumigashira, Y. Matsumoto, H. Koinuma, and M. Oshima, Electronic structure characterization of La_2NiMnO_6 epitaxial thin films using synchrotron-radiation photoelectron spectroscopy and optical spectroscopy, Appl. Phys. Lett. 2009, **94**, 262503.

[15] Zhiqing Zhang, Hongbin Jian, Xianwu Tang, Jie Yang, Xuebin Zhu, Yuping Sun, Synthesis and characterization of ordered and disordered polycrystalline La_2NiMnO_6 thin films by sol-gel, Dalton Trans. 2012, **41**, 11836-11840.

[16] R.I. Dass, J.Q. Yan, J. B. Goodenough, Oxygen stoichiometry, ferromagnetism, and transport properties of $La_{2-x}NiMnO_{6+\delta}$, Phys. Rev. B 2003, **68**, 064415.

[17] N. Troullier, J.L. Martins, Efficient pseudopotentials for plane-wave calculations, Phys. Rev. B 1991, **43**, 1993.

[18] P. Giannozzi, S. Baroni, N. Bonini *et al.*, QUANTUM ESPRESSO: a modular and open-source software project for quantum simulations of materials, J. Phys.: Condens. Matter. 2009, **21**, 395502.

[19] J.P. Perdew, K. Burke, and M. Ernzerhof, Generalized gradient approximation made simple, Phys. Rev. Lett. 1996, **77**, 3865.

[20] M. Zhu, Y. Lin, E.W.C. Lo, *et al.*, Electronic and magnetic properties of La_2NiMnO_6 and La_2CoMnO_6 with cationic ordering, Appl. Phys. Lett. 2012, **100**, 062406.

[21] M.C. Sánchez, J. García, J. Blasco, G. Subías, J. Perez-Cacho, Local electronic and geometrical structure of $LaNi_{1-x}MnxO_{3+\delta}$ perovskites determined by x-ray-absorption

spectroscopy, Phys. Rev. B 2002, **65**, 144409.

[22] D. Munoz, N.M. Harrison, F. Illas, Electronic and magnetic structure of $LaMnO_3$ from hybrid periodic density-functional theory, Phys. Rev. B 2004, **69**, 085115.

[23] C. Mitra, Z. Hu, P. Raychaudhuri, S. Wirth, S.I. Csiszar, H.H. Hsieh, H.J. Lin, C.T. Chen, L.H. Tjeng, Direct observation of electron doping in $La_{0.7}Ce_{0.3}MnO_3$ using x-ray absorption spectroscopy, Phys. Rev. B 2003, **67**, 092404.

[24] F Bern, M Ziese, A Setzer, E Pippel, D Hesse and I Vrejoiu, Structural, magnetic and electrical properties of $SrRuO_3$ films and $SrRuO_3/SrTiO_3$ superlattices, J. Phys.: Condens. Matter. 2013, **25**, 496003.

[25] K. Momma, F. Izumi, VESTA 3 for three-dimensional visualization of crystal, volumetric and morphology data, J. Appl. Crystallogr. 2011, **44**, 1272.

[26] C.L. Bull, D. Gleeson, K.S. Knight, Determination of *B*-site ordering and structural transformations in the mixed transition metal perovskites La_2CoMnO_6 and La_2NiMnO_6, J. Phys.: Condens. Matter 2003, **15**, 4927.

[27] C.F. Lan, S Zhao, T.T. Xu, J. Ma, S. Hayase, T.L. Ma, Investigation on structures, band gaps, and electronic structures of lead free La_2NiMnO_6 double perovskite materials for potential application of solar cell. J. Alloys Compd. 2016, **655**, 208-214.

General conclusions

The thesis was focused on the development of the absorbing materials for perovskite solar cells. In Chapter 1, we introduced the recent process of halide perovskite solar cells. They are being developed rapidly. However, so far they are still facing several drawbacks, such as the request of higher power conversion efficiency, lead-pollution, hysteresis and instability. These are hindering their further commercialization. In order to overcome these drawbacks, first, in this thesis we developed a new method to control the growth of high-quality $CH_3NH_3PbI_3$ perovskite films for high-performance perovskite solar cells, and then we developed the composite perovskite layers for lead-free solar cell applications from the aspects of microstructure control, absorption tuning and energy level realignment. At last, we investigated the structures and electronical properties of stable double perovskite La_2NiMnO_6 oxide materials for their potential application on solar cells.

In Chapter 2, we briefly summarized the experimental procedures, including the general preparation and characterization of perovskite materials and electrodes, as well as devices used in this thesis.

In Chapter 3, a new method of two-step concentration gradient controlled reactions has been developed to prepare high-quality $CH_3NH_3PbI_3$ perovskite films. Compared with the traditional single solution method, the concentration gradient controlled method lead to the perovskite films with large grains and full coverage. Meanwhile, the spectral absorption of the perovskite films was enhanced due to the size-dependent light scattering. When the perovskite solar cells were fabricated from these films in ambient conditions with high humidity, they exhibited an obviously improved photovoltaic performance. Furthermore, the mechanism for the concentration gradient controlled growth has also been explored by the XRD and SEM. This method offered a new approach to prepare high-quality films.

In Chapter 4, lead-free composite absorbing materials with $(CH_3NH_3)_3Bi_2I_9$ perovskite and BiI_3 were developed. Enhanced crystallization was found in BiI_3-based composite films with the introduction of lead-free $(CH_3NH_3)_3Bi_2I_9$ perovskite. Multi-absorptions and tuned energy levels were observed in the BiI_3-based composites due to the addition of $(CH_3NH_3)_3Bi_2I_9$. We found that the photovoltaic performance of the BiI_3-based composite solar cells was significantly improved due to the introduction of $(CH_3NH_3)_3Bi_2I_9$ perovskite, with the obviously improved V_{oc}

from 0.44 to 0.57 V, and the power conversion efficiency from 0.045% to 0.076%. The design of composites offered a new route to design the lead-free solar cells.

In Chapter 5, we tried to develop the lead-free double perovskite oxide absorber for the stable solar cells. The perovskites La_2NiMnO_6 are first studied for application on perovskite solar cells. Their structures and optical/electronic properties were studied from the experimental and theoretical aspects. The structures and properties of double perovskite La_2NiMnO_6 materials varied with the synthesizing conditions. The monoclinic La_2NiMnO_6 sample had an experimental bandgap of 1.4 eV and the valence band of -5.8 eV. Whereas, the rhombohedral La_2NiMnO_6 had an experimental bandgap of 1.2 eV and the valance band of -5.7 eV. Furthermore, the density function theory calculation confirmed that the theoretical bandgap of the monoclinic La_2NiMnO_6 was larger than that of the rhombohedral La_2NiMnO_6, which was mainly attributed to the *B*-site distortion. Simultaneously, the interaction of the Ni 3*d*, O 2*p* and Mn 3*d* orbitals resulted in the variation of the top of the VB and the bottom of the CB in La_2NiMnO_6 perovskites. Our results showed that monoclinic La_2NiMnO_6 is a better candidate of absorbing materials for solar cells than the rhombohedral La_2NiMnO_6.

Future Prospects

The perovskite solar cells based on the $CH_3NH_3PbX_3$ materials (X = I, Br and Cl) have been developing very well in the recent two years. Their efficiency certified by NREL has reached 22.1% by far and the stability has been sharply improved to 6 months, which make them more rival to silicon solar cells. However, the silicon solar cells also developed well. The cost of silicon solar cells has been significantly reduced to 1/3 during the past five years. And the power conversion efficiency of practical silicon solar module reached a new record above 26% in this year. All these created more challenges for the development of perovskite solar cells in the future.

The future prospects of perovskite solar cells might include following fields, the development of high-quality perovskite layers, architectures designing of solar cells, sealing and recycling. The current research indicated that the performance of perovskite solar cells can be sharply affected by the quality of perovskite active layers and the architecture of solar cells. The perovskite layers fundamentally influence the light absorption and energy conversion, and the architectures will affect the charge transport and the stability of the devices. Therefore, the optimizations of perovskite layers and architectures are expected to improve the performance of the perovskite solar cells. Besides the photovoltaic performance of the perovskite solar cells, their sealing and recycling are becoming the research hotspot. Sealing of the devices will be a key point for the long-term stable solar cells, particularly for oxygen and humidity sensitive perovskite solar cells. This will affect the cost of manufacturing and using and their commercialization. The recycling of degraded perovskite solar cells can not only reduce the risk of lead-pollution, but also reduce the practical cost. At last, the lead problem might be wholly resolved by developing new lead-free perovskite materials. The investigation of lead-free perovskite materials for solar cells will still be a big challenge, because it seems that expect the Pb-based materials, other single halide perovskite cannot obtain a high optical performance. However, the investigation in this field can be focused on the double perovskite oxides, layered perovskite materials or the pseudo-perovskite solar cells.

Achievements

Publications

1. **CF Lan**, S Zhao, TT Xu, J Ma, S Hayase, TL Ma, Investigation on structures, band gaps, and electronic structures of lead free La_2NiMnO_6 double perovskite materials for potential application of solar cell. Journal of Alloys and Compounds 2016, 655, pp 208-214.
2. **CF Lan**, S Zhao, C. Zhang, WG Liu, S Hayase, TL Ma, Concentration gradient controlled growth of $CH_3NH_3PbI_3$ films and light-scattering-enhanced spectral absorption in long-wavelength region, CrystEngComm 2016, 18, pp 9243 - 9251.
3. **CF Lan**, S Zhao, C Zhang, WG Liu, S Hayase, TL Ma, Effect of Multiplicative Interaction between Bismuth Triiodide and Layered Organic-Inoganic Perovskite on Spectrum Absorption and Photovoltaic Performance of Solar Cells, Alloys and Compounds 2017, 701, pp 834-840.
4. S Zhao, **CF Lan**, J Ma, SS Pandey, S Hayase, TL Ma, First principles study on the electronic and optical properties of B-site ordered double perovskite Sr_2MMoO_6 (M = Mg, Ca, and Zn). Solid State Communications 2015, 213, pp 19-23.
5. S Zhao, LG Gao, **CF Lan**, SS Pandey, S Hayase, TL Ma, First principles analysis of oxygen vacancy formation and migration in Sr_2BMoO_6 (B = Mg, Co, Ni), RSC Advances. 2016, 38(6), pp 31968-31975.

Conference

1. Poster: **Chunfeng Lan**, Jie Ma, Shuai Zhao, Tingli Ma, Studies of synthesis and properties of Pb-free provskite $SrTi_xFe_{1-x}O_{3-\delta}$ and its potential application for perovskite solar cells, 第 6 回薄膜太陽電池セミナー２０１４, Oct 15-16th, 2014, Hiroshima, Japan.

Acknowledgement

First, I would like to express my deepest thanks to my supervisor Prof. Tingli Ma. She offered me the opportunity to study in Japan. She is very knowledgeable and creative on solar cells, having taught me many knowledges in this field. She effectively guided my PhD thesis research. In addition, she is energetic and passionate, setting up a good example to follow in my academic research in Japan.

Second, I would like to show my great thanks to Prof. Shuzi Hayase and Prof. Shyam S. Pandey. Prof. Shuzi Hayase is very professional on semiconductor materials and solar cells. He can clearly explain his ideas to his students and carefully teach them. I still remember that I learnt a lot from the class and daily discussion with Prof. Hayase on lead-free perovskite materials. Prof. Shyam S. Pandey is a kindly professor in daily life and has many creative skills on experiments. He offered me many suggestions and supported me a lot during my experiment in the solar lab. More importantly, they offered me the platform to do experiment on solar cells. Without their helps, I could hardly finish my thesis in time. In addition, they kindly did me a lot of favor in my daily life, including writing recommendation letter for me on job hunting.

Third, I would like to thank all the members in the solar lab, including the Prof. Ogomi, Mr. Sakamoto, Miss Nishimura, Mr. Shimazaki, Dr. Teresa, and the students Dr. Kapil, Dr. Ajay, Mr. Hirotani, Mr. Morimoto, Mr. Nishiyama and Mr. Moriya *et al*. During my studying in the solar lab, they helped me a lot on experiments, such as the UV-visible spectral measurement, I-V measurement, sputtering use. They let me feel like in a big warm family.

Forth, I would like to thank all the members in Ma Lab and my tutor Mr. Zhao Qi. They gave me many suggestions and strongly encouraged me when I faced troubles. Particularly, I would like thank to Mr. Zhao Shuai, he supported the theoretical part in Chapter 5 in my thesis. With their helps, I successfully carried out my research.

Last but not least, I would like to express my thanks to my family. My family is just like a warm mind harbor for me when I am living abroad. Their support and encouragement have always inspired me to fight for a better research work and a better life in the future. Finally, I also expressed my gratitude to the persons who once made contribution to this thesis, I feel sorry but I could not show my thanks to them one by one.

Appendix

For Chapter 3.

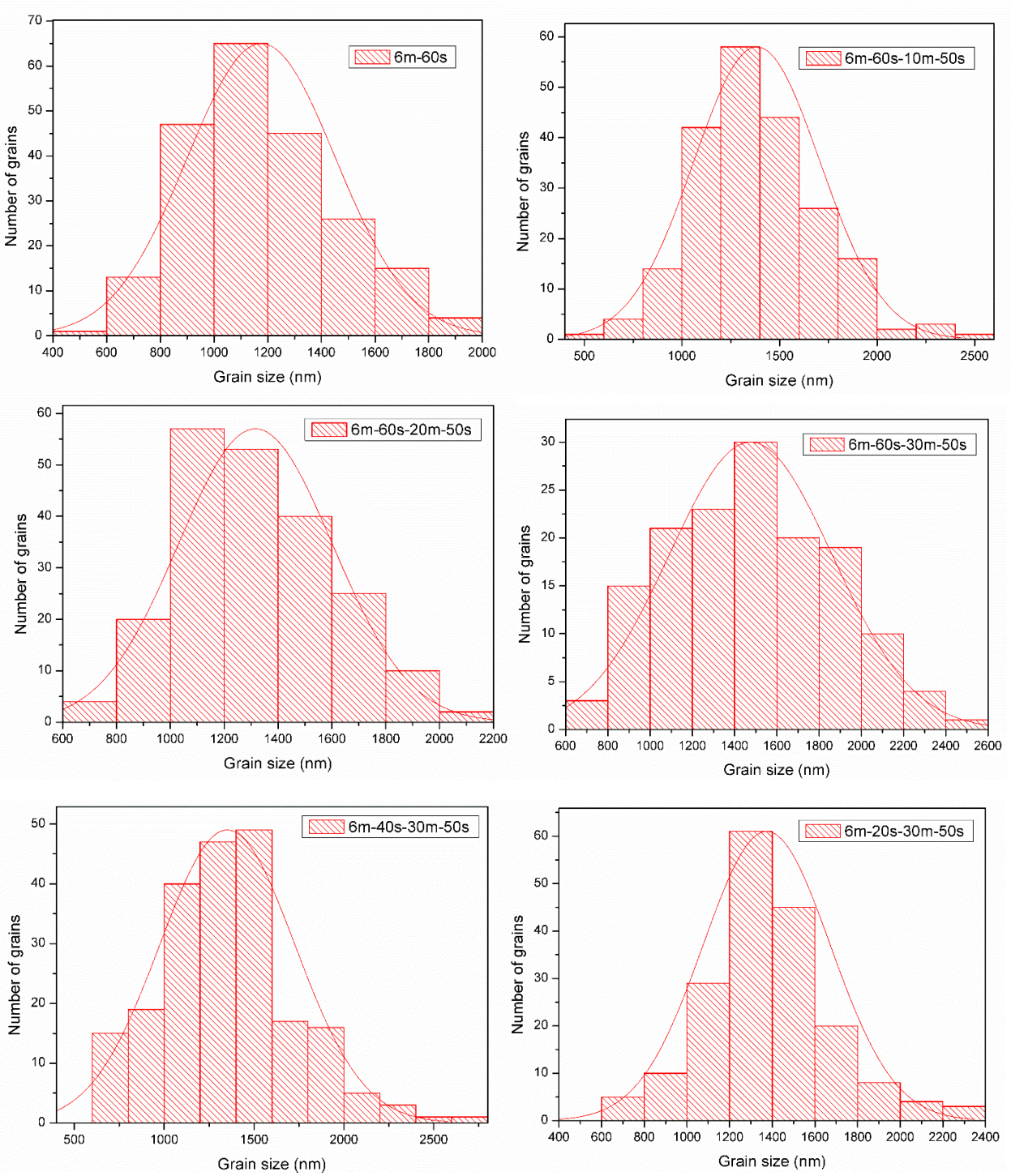

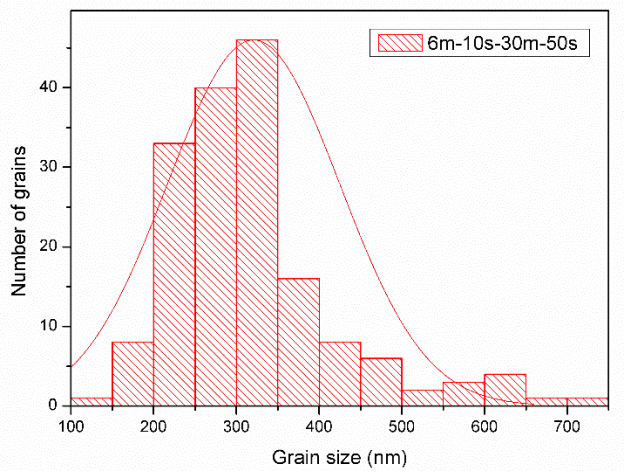

Fig. S1. Histogram of the grain sizes of the perovskite films.

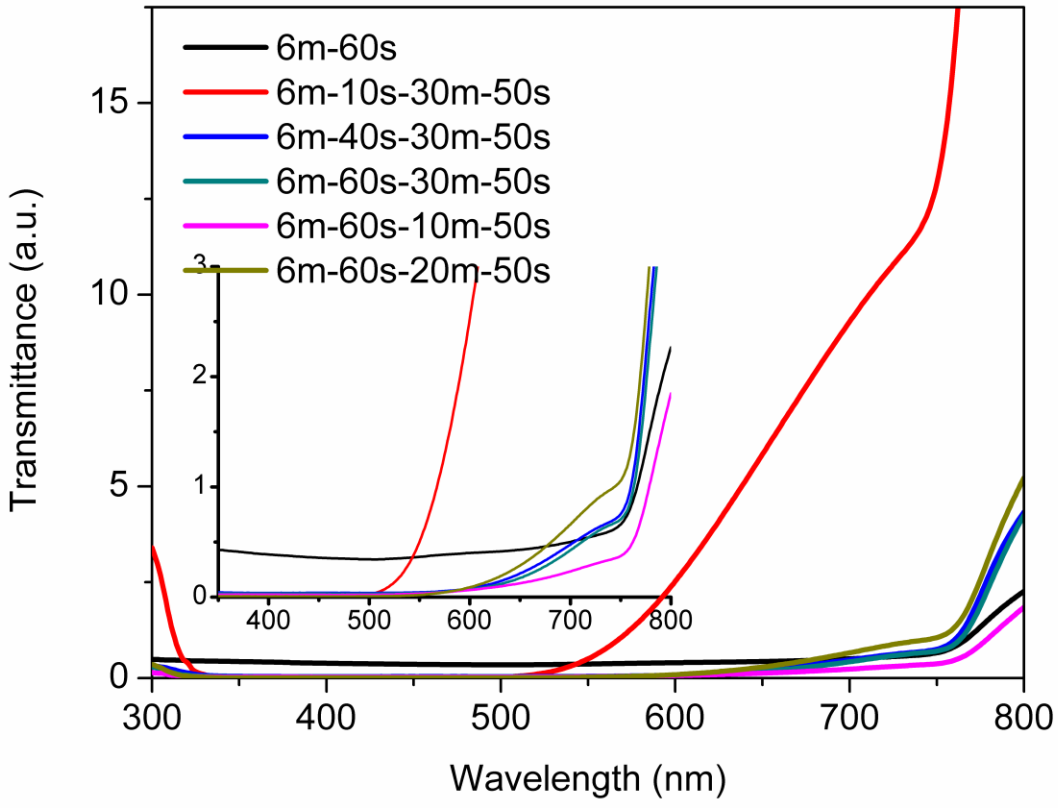

Fig. S2. Transmission of the perovskite films.

Table S1. List of *I-V* information of the solar devices (MAI concentration effect).

	J_{sc} (mA/cm^2)	V_{oc} (V)	FF	*PCE* (%)
6m-60s				
	9.90	0.87	0.61	5.25
	10.63	0.80	0.46	3.96
6m-60s-10m-50s				
	12.52	0.91	0.58	6.59
	13.93	0.89	0.53	6.50
	13.85	0.89	0.61	7.52
6m-60s-20m-50s				
	15.88	0.91	0.59	8.56
	16.79	0.91	0.62	9.57
	17.60	0.91	0.62	9.92
6m-60s-30m-50s				
	18.09	0.98	0.65	11.48
	17.89	0.98	0.62	10.92
	17.48	0.97	0.64	10.81

Table S2. List of *I-V* information of the solar devices (MAI loading time effect)

	J_{sc} (mA/cm^2)	V_{oc} (V)	FF	*PCE* (%)
6m-60s				
	9.90	0.87	0.61	5.25
	10.63	0.80	0.46	3.96
6m-10s-30m-50s				
	13.10	0.90	0.60	7.02
	11.81	1.00	0.67	7.93
	15.49	0.92	0.55	7.91
	14.87	0.94	0.68	9.53
6m-20s-30m-50s				
	11.07	0.97	0.62	6.61

	15.87	0.93	0.49	7.29
	13.18	0.94	0.70	8.60
	14.53	0.89	0.53	6.81
6m-40s-30m-50s				
	15.07	0.92	0.63	8.77
	17.87	0.93	0.63	10.47
	17.54	0.93	0.63	10.30
6m-60s-30m-50s				
	18.09	0.98	0.65	11.48
	17.89	0.98	0.62	10.92
	17.48	0.97	0.64	10.81

For Chapter 4

EDX results of the films

The EDX was performed on the $(BiI_3)_{1-x}(MBI)_x$ films coated with Au and Pd.

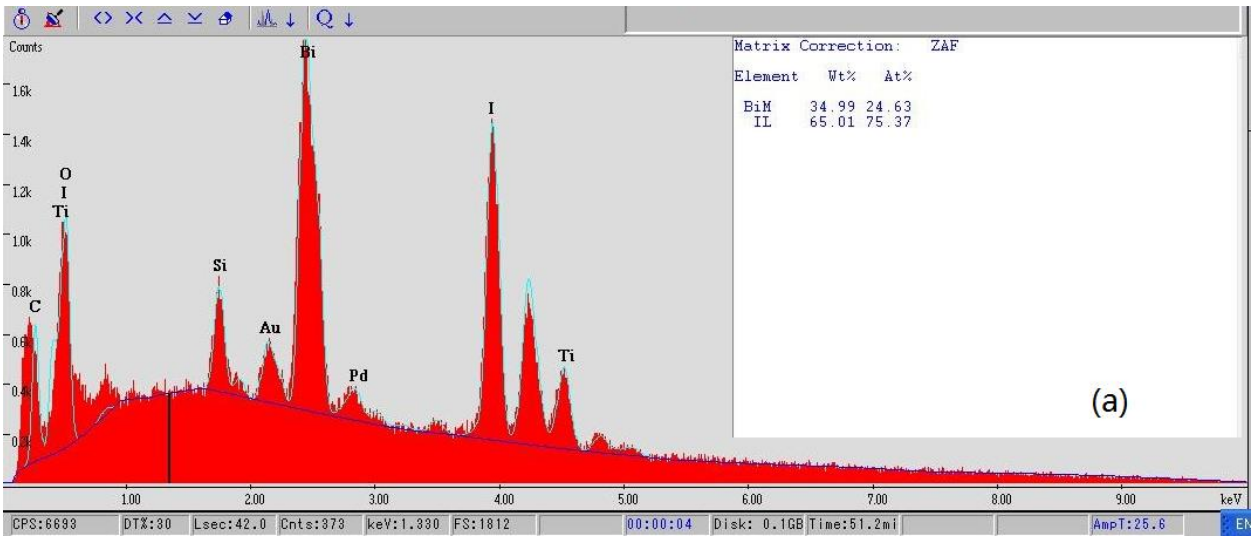

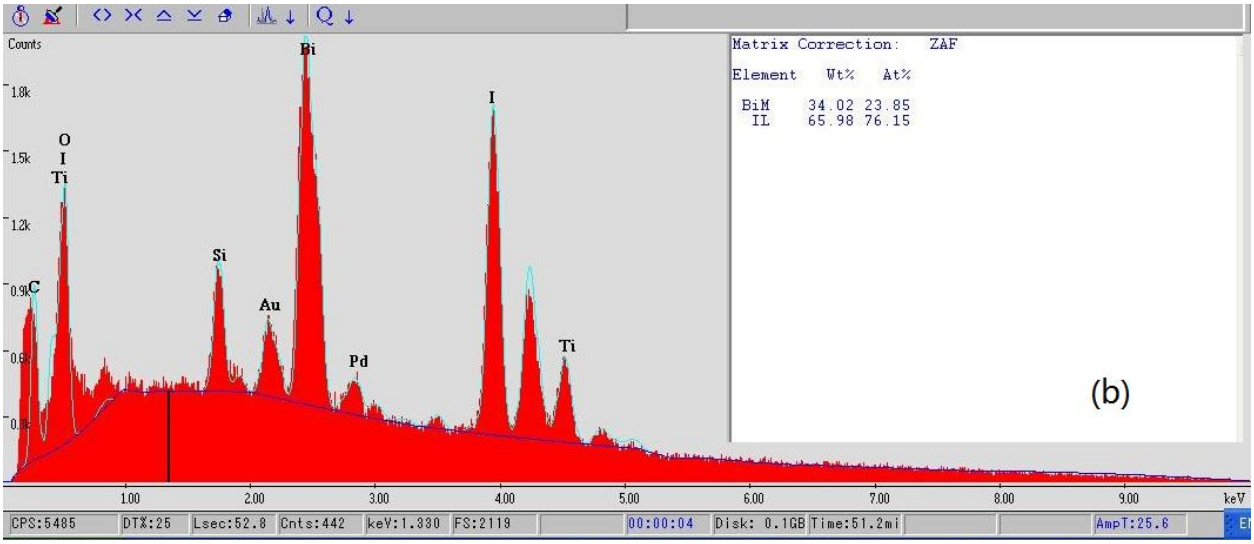

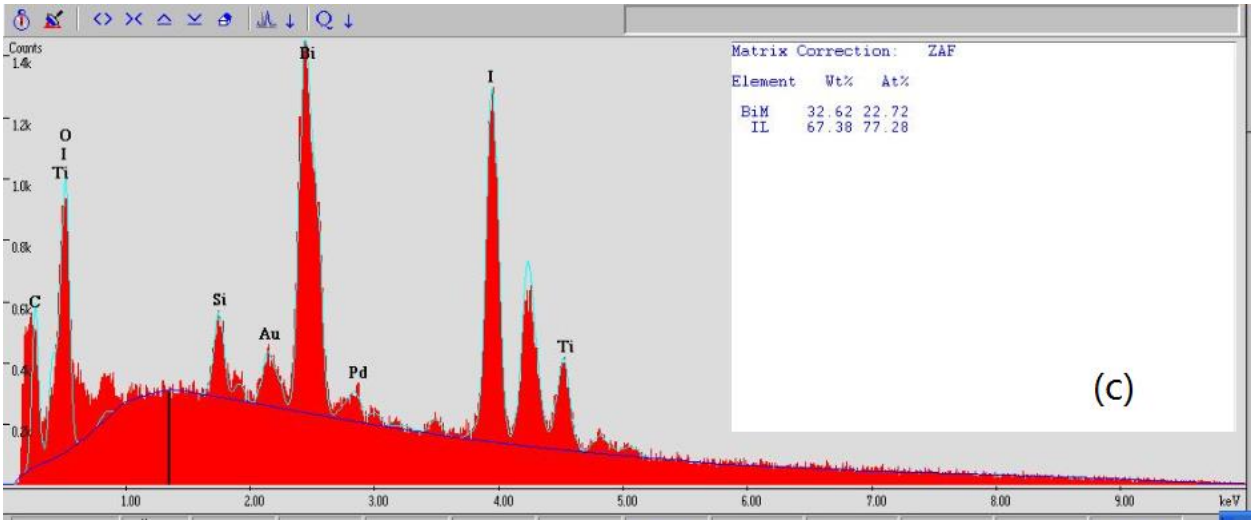
Counts
O
I
Ti
C
Si
Au
Bi
Pd
I
Ti
Matrix Correction: ZAF
Element Wt% At%
BiM 32.62 22.72
IL 67.38 77.28
(c)
1.00
2.00
3.00
4.00
5.00
6.00
7.00
8.00
9.00
keV

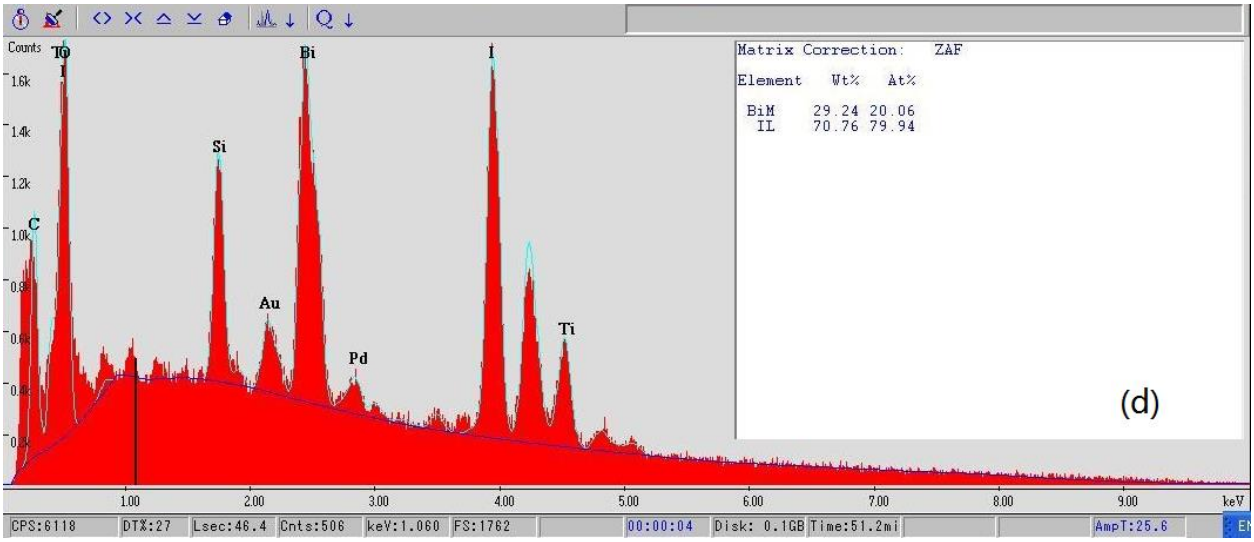
Counts
O
I
C
Si
Au
Bi
Pd
I
Ti
Matrix Correction: ZAF
Element Wt% At%
BiM 29.24 20.06
IL 70.76 79.94
(d)
1.00
2.00
3.00
4.00
5.00
6.00
7.00
8.00
9.00
keV
CPS:6118 DT%:27 Lsec:46.4 Cnts:506 keV:1.080 FS:1762 00:00:04 Disk: 0.1GB Time:51.2mi AmpT:25.6

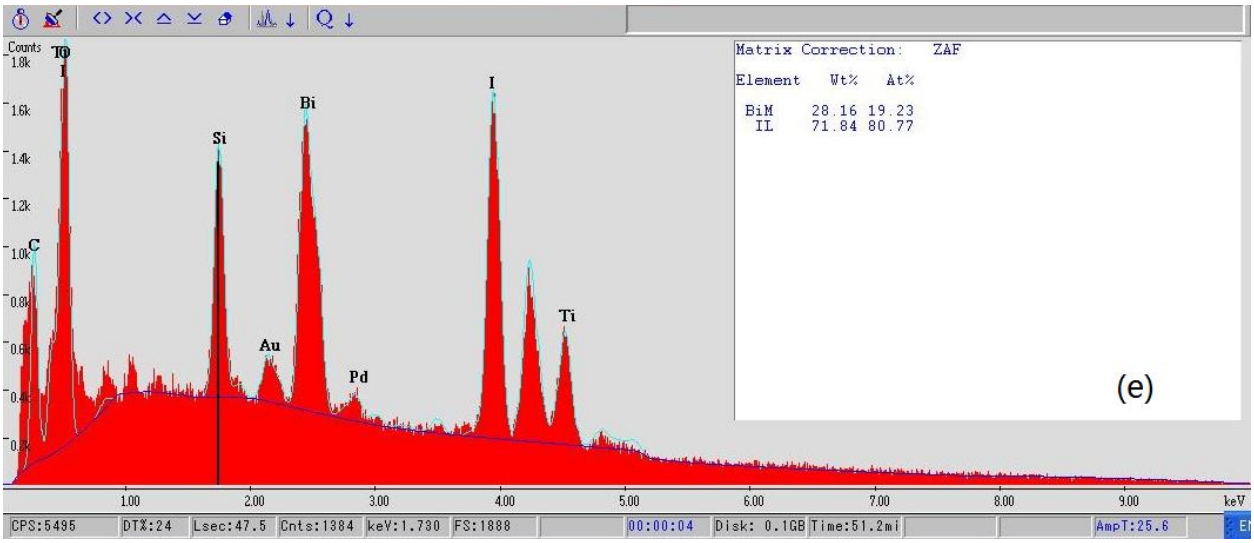
Counts
O
I
C
Si
Au
Bi
Pd
I
Ti
Matrix Correction: ZAF
Element Wt% At%
BiM 28.16 19.23
IL 71.84 80.77
(e)
1.00
2.00
3.00
4.00
5.00
6.00
7.00
8.00
9.00
keV
CPS:5495 DT%:24 Lsec:47.5 Cnts:1384 keV:1.730 FS:1888 00:00:04 Disk: 0.1GB Time:51.2mi AmpT:25.6

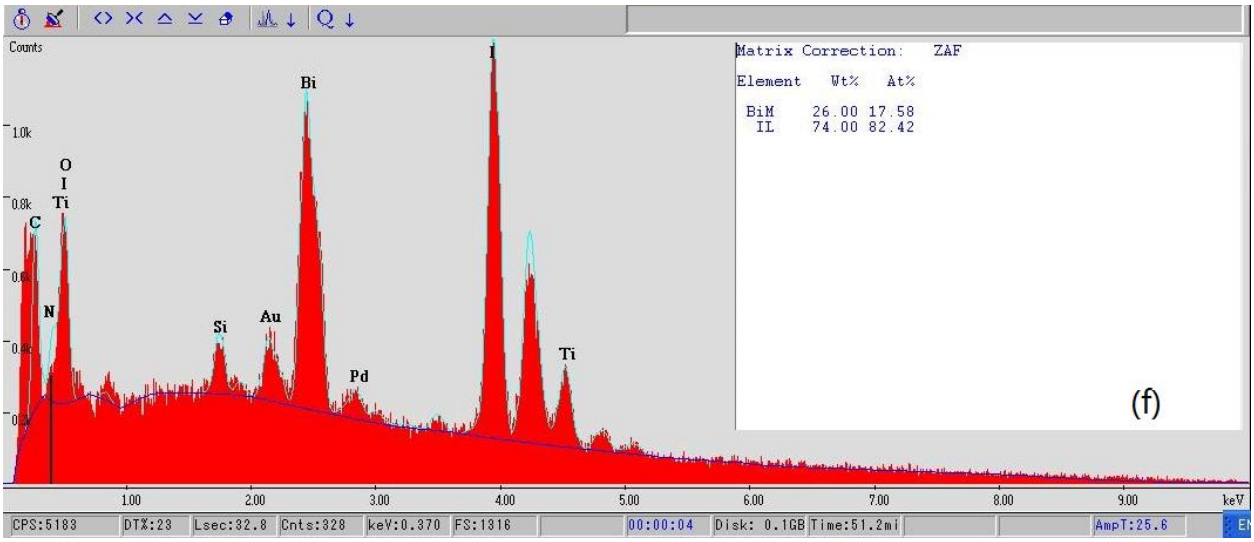

Fig. S1. EDX results of the $(BiI_3)_{1-x}(MBI)_x$ films. a) x = 0, b) x = 0.10, c) x = 0.20, d) x =0.50, e) x = 0.75, f) x = 1.0.

PYS results for the valence band measurement of the films

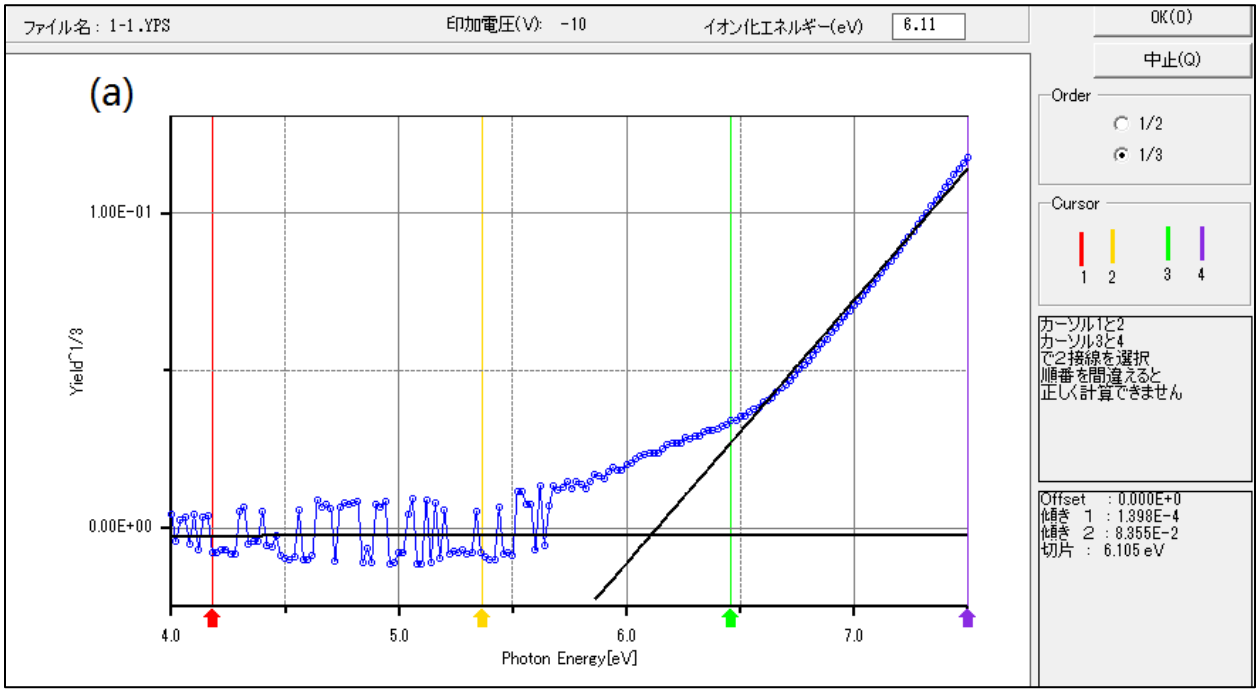

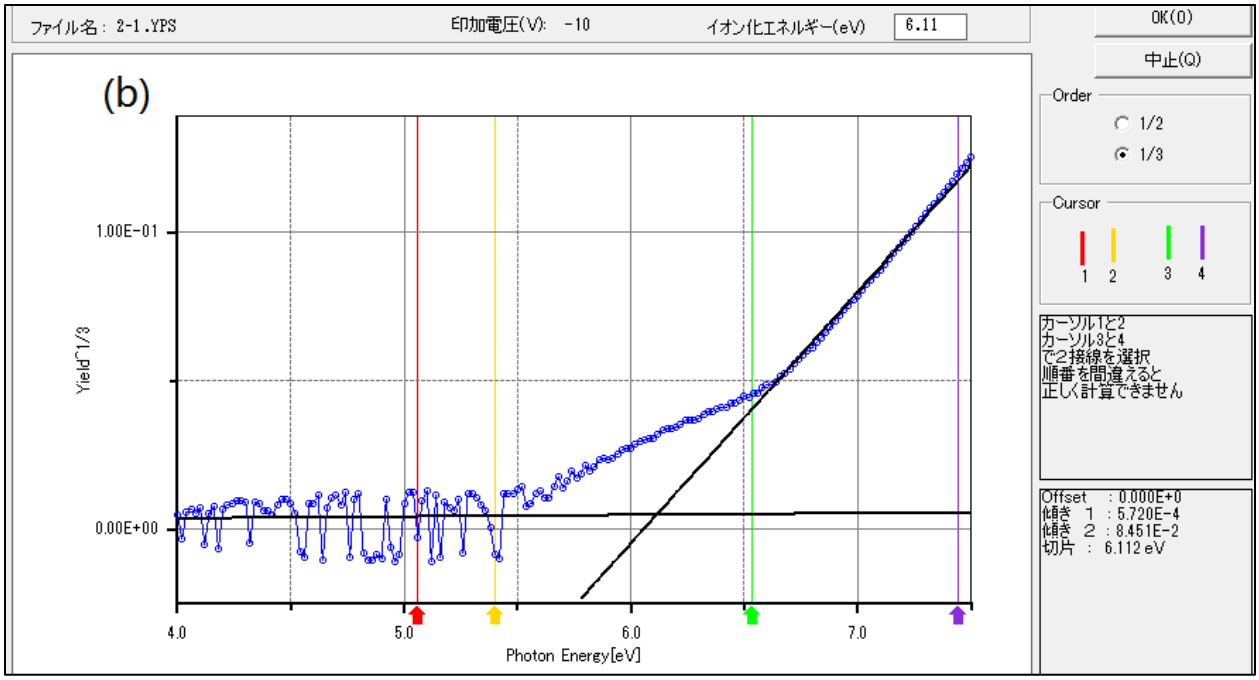
ファイル名： 2-1.YPS
印加電圧(V): -10
イオン化エネルギー(eV) 6.11
OK(O)
中止(Q)
(b)
Order
1/2
1/3
Cursor
1 2 3 4
カーソル1と2
カーソル3と4
で2接線を選択
順番を間違えると
正しく計算できません
Offset : 0.000E+0
傾き 1 : 5.720E-4
傾き 2 : 8.451E-2
切片 : 6.112 eV
1.00E-01
0.00E+00
Yield^1/3
4.0
5.0
6.0
7.0
Photon Energy[eV]

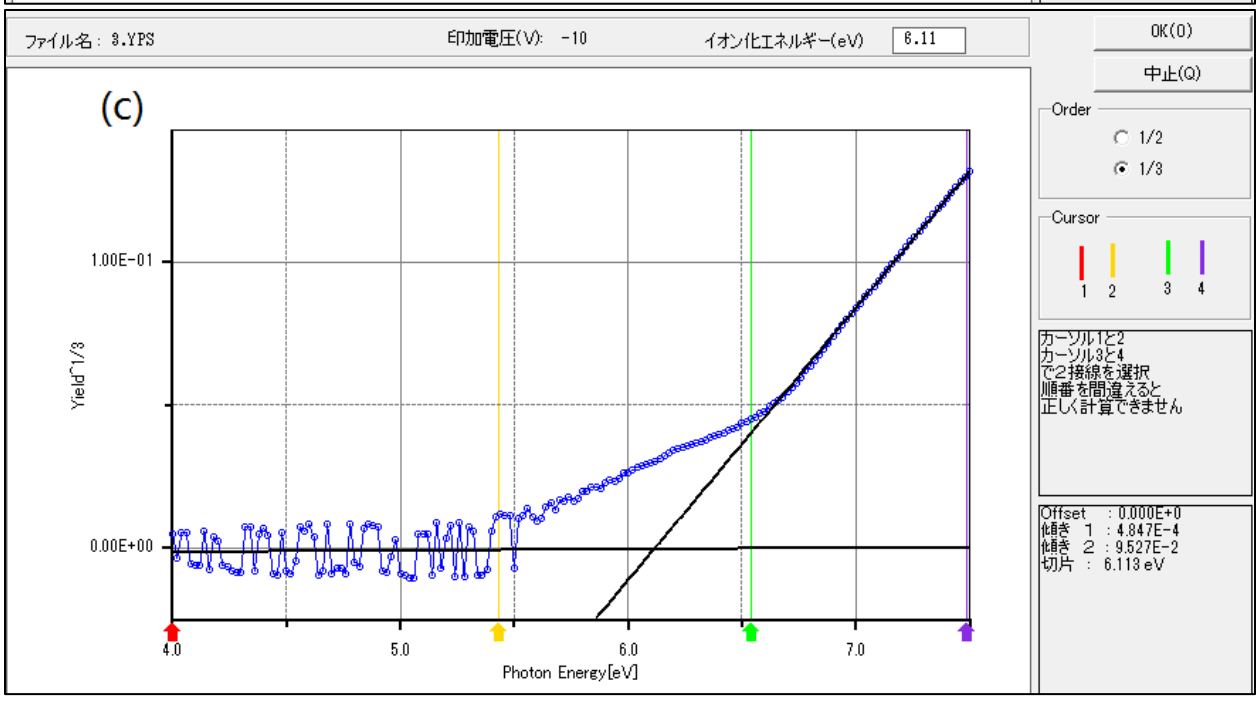
ファイル名： 3.YPS
印加電圧(V): -10
イオン化エネルギー(eV) 6.11
OK(O)
中止(Q)
(c)
Order
1/2
1/3
Cursor
1 2 3 4
カーソル1と2
カーソル3と4
で2接線を選択
順番を間違えると
正しく計算できません
Offset : 0.000E+0
傾き 1 : 4.847E-4
傾き 2 : 9.527E-2
切片 : 6.113 eV
1.00E-01
0.00E+00
Yield^1/3
4.0
5.0
6.0
7.0
Photon Energy[eV]

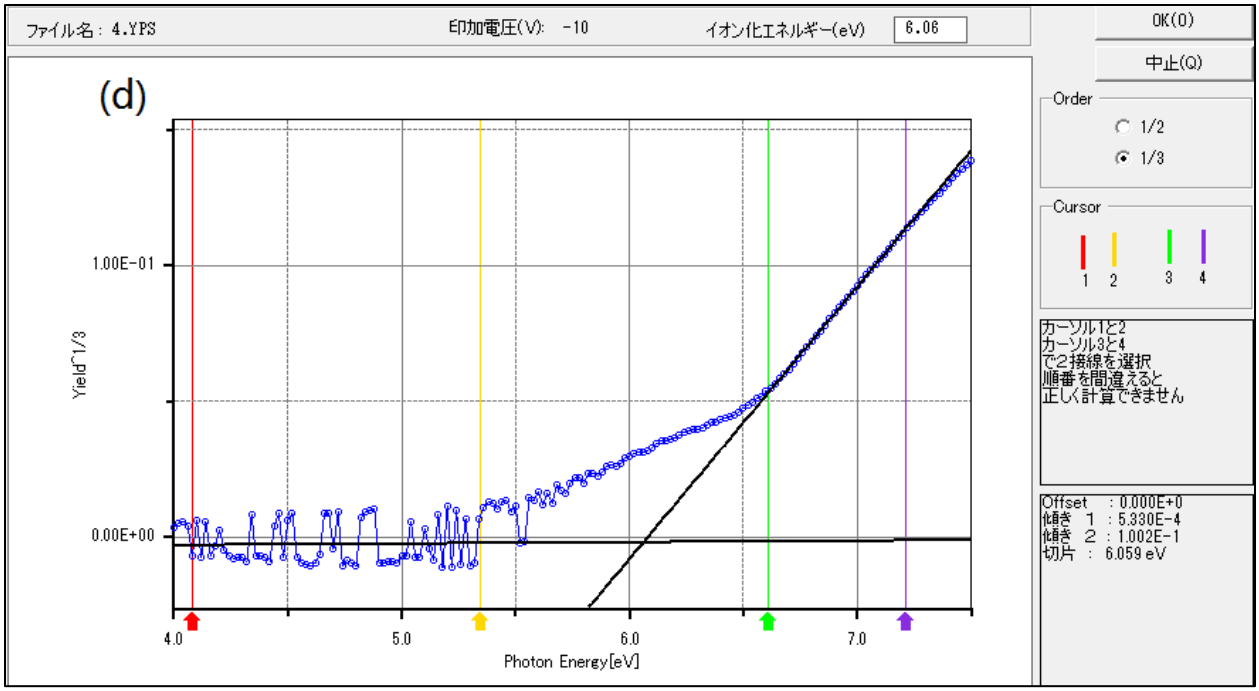
ファイル名：4.YPS
印加電圧(V): -10
イオン化エネルギー(eV)
6.06
OK(O)
中止(Q)
(d)
Order
1/2
1/3
Cursor
1 2 3 4
カーソル1と2
カーソル3と4
で2接線を選択
順番を間違えると
正しく計算できません
Offset : 0.000E+0
傾き 1 : 5.330E-4
傾き 2 : 1.002E-1
切片 : 6.059 eV
1.00E-01
0.00E+00
Yield^1/3
4.0
5.0
6.0
7.0
Photon Energy[eV]

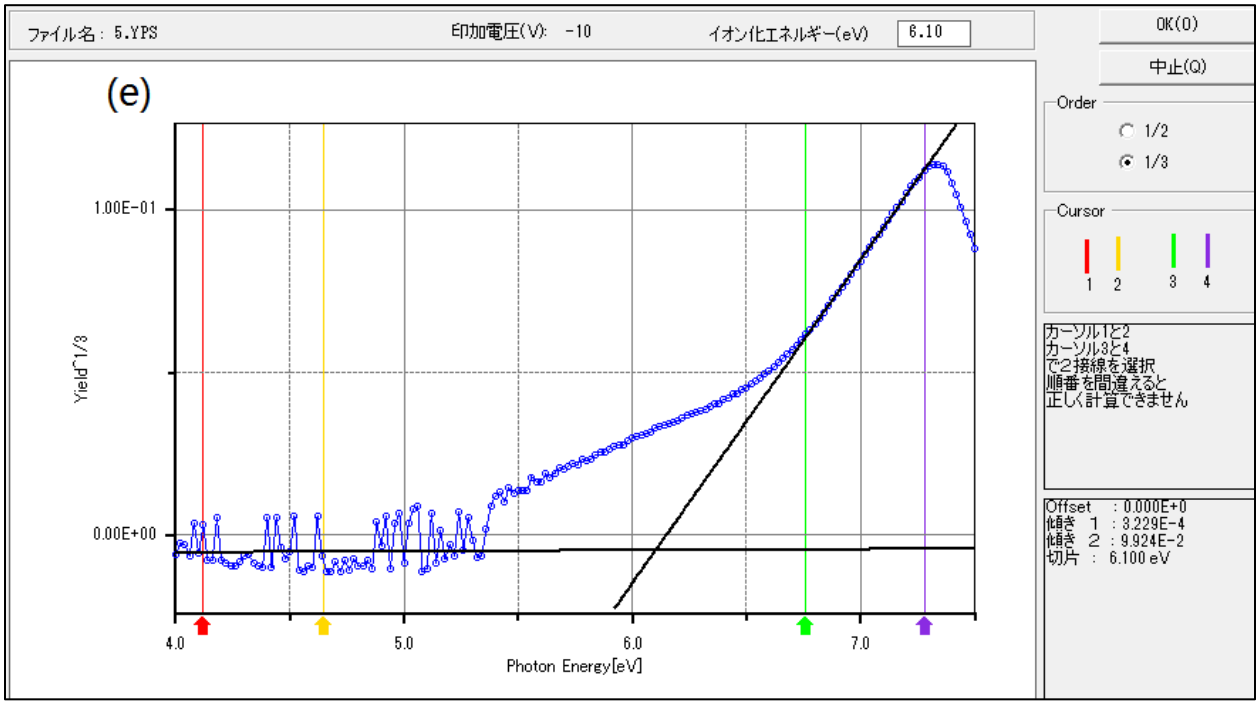
ファイル名：5.YPS
印加電圧(V): -10
イオン化エネルギー(eV)
6.10
OK(O)
中止(Q)
(e)
Order
1/2
1/3
Cursor
1 2 3 4
カーソル1と2
カーソル3と4
で2接線を選択
順番を間違えると
正しく計算できません
Offset : 0.000E+0
傾き 1 : 3.229E-4
傾き 2 : 9.924E-2
切片 : 6.100 eV
1.00E-01
0.00E+00
Yield^1/3
4.0
5.0
6.0
7.0
Photon Energy[eV]

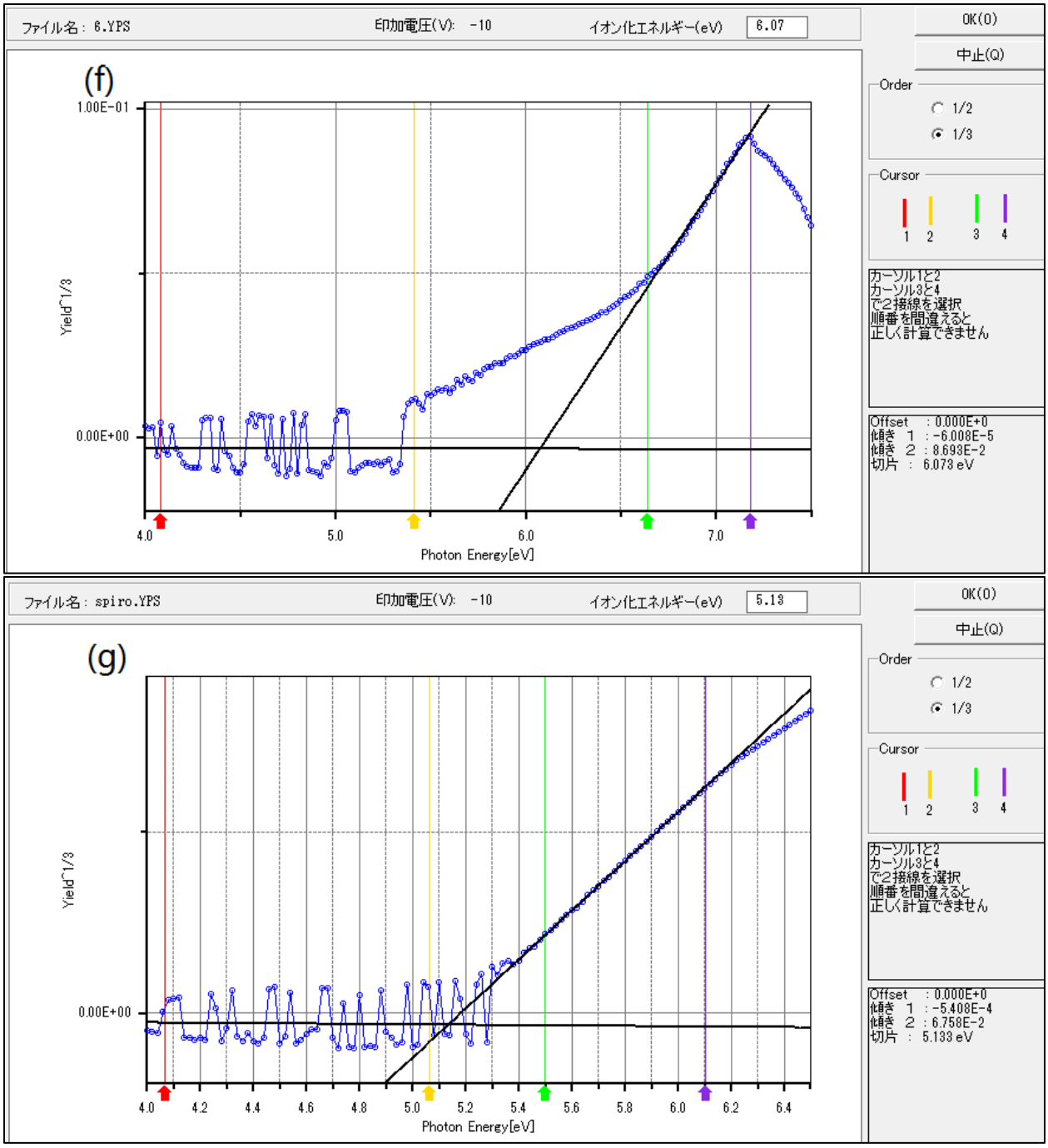

Fig. S2 PYS results of the $(BiI_3)_{1-x}(MBI)_x$ films and the Spiro film. a) x = 0, b) x = 0.10, c) x = 0.20, d) x = 0.50, e) x = 0.75, f) x = 1.0, g) the Spiro film.

I-V characteristic of the $(BiI_3)_{1-x}(MBI)_x$ solar cells

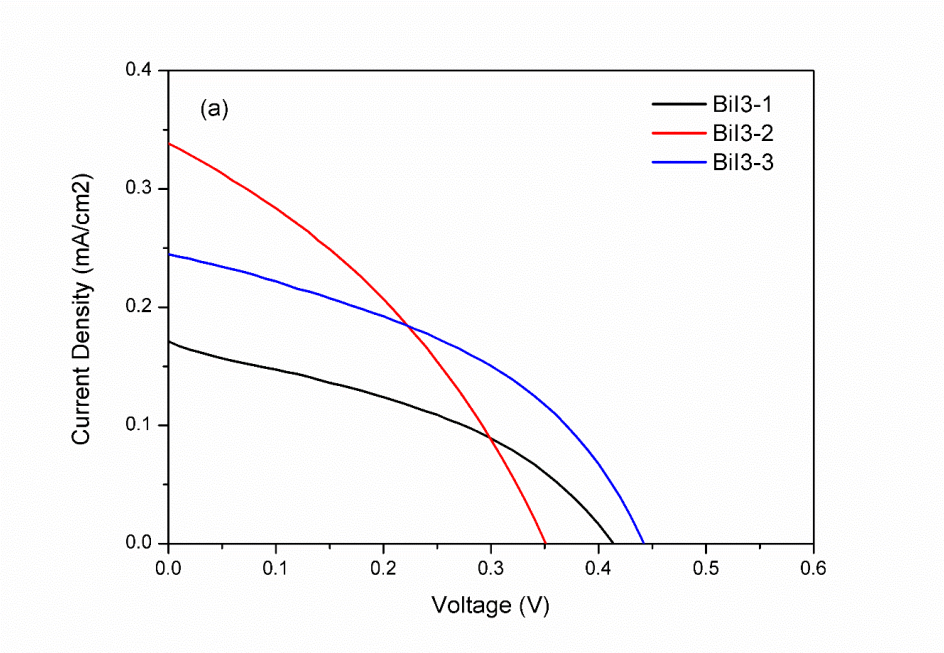

Fig. S3(a). *I-V* characteristics of the BiI_3 solar cells.

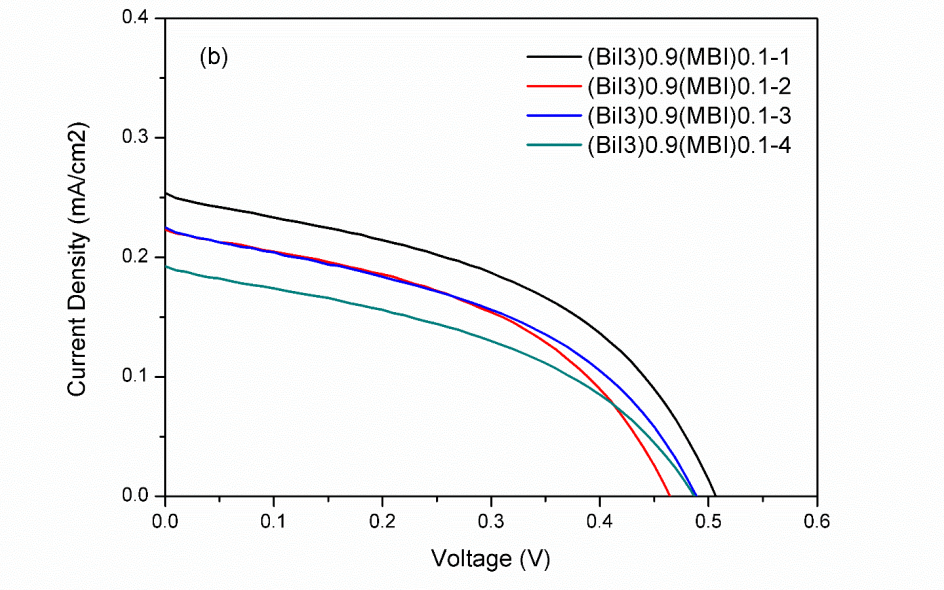

Fig. S3(b). *I-V* characteristics of the $(BiI_3)_{0.9}(MBI)_{0.1}$ solar cells.

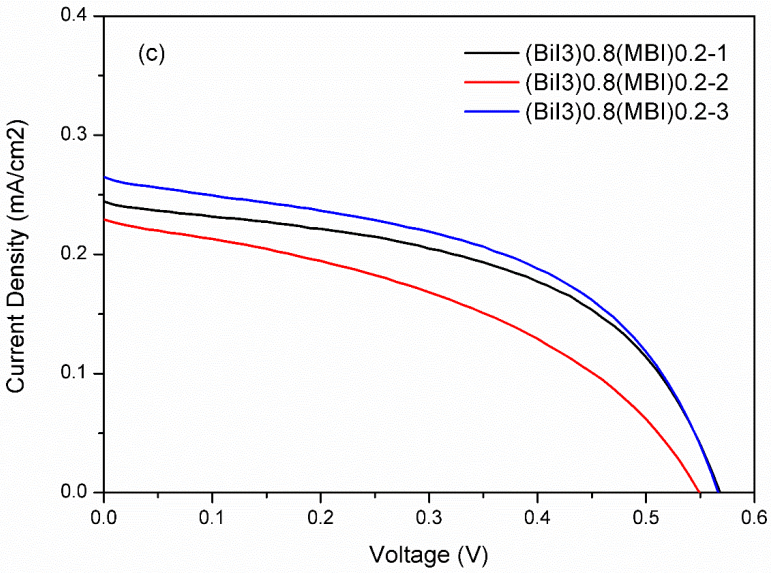

Fig. S3(c). *I-V* characteristics of the $(BiI_3)_{0.8}(MBI)_{0.2}$ solar cells.

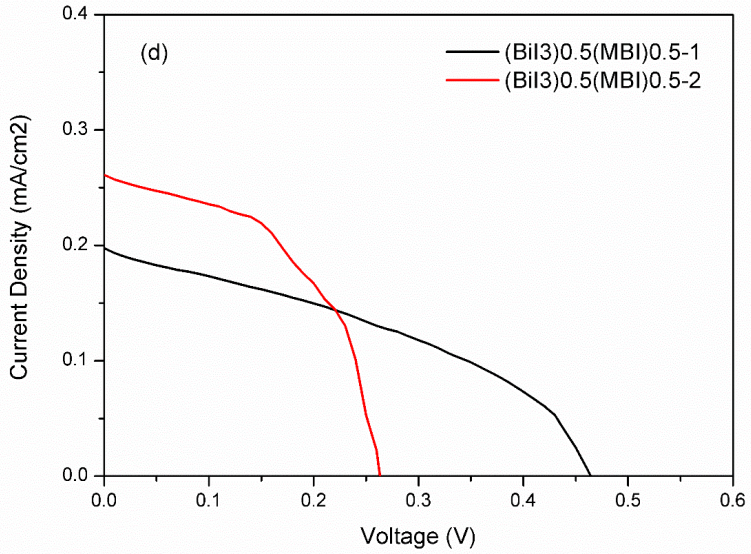

Fig. S3(d). *I-V* characteristics of the $(BiI_3)_{0.5}(MBI)_{0.5}$ solar cells.

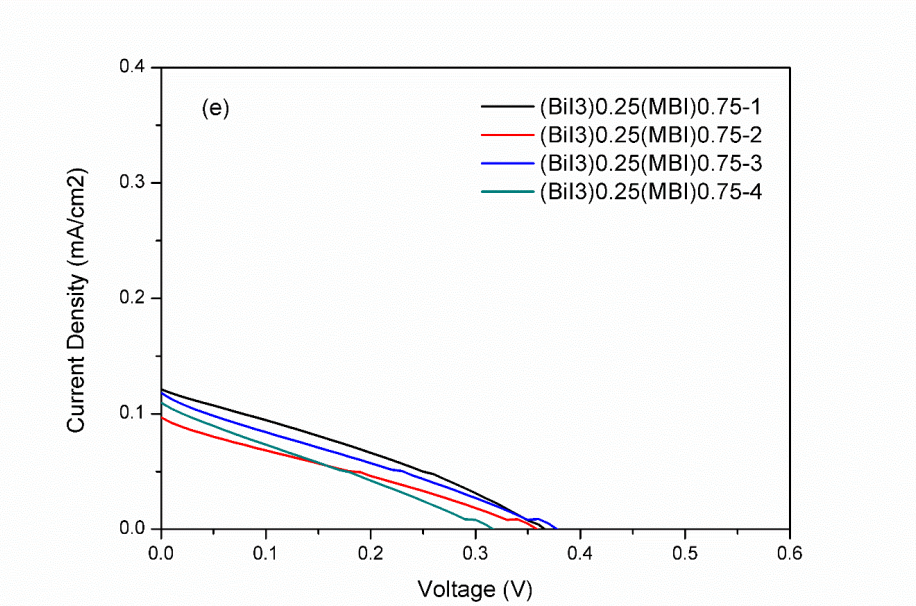

Fig. S3(e). *I-V* characteristics of the $(BiI_3)_{0.25}(MBI)_{0.75}$ solar cells.

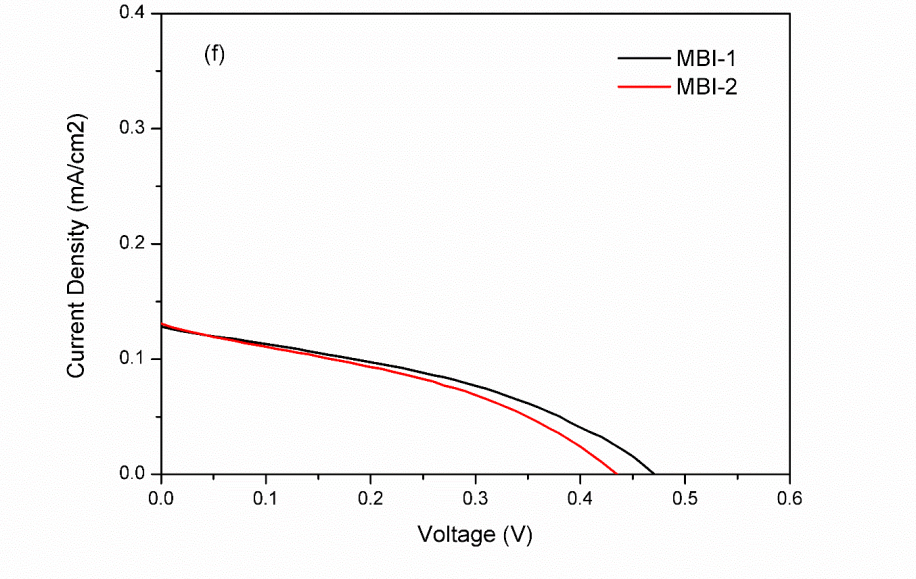

Fig. S3(f). *I-V* characteristic of the $(BiI_3)_{1-x}(MBI)_x$ solar cells.

Table S1. The list of the *I-V* characteristic of each group (measured by the forward scanning).

	Jsc (mA/cm^2)	V_{oc} (V)	FF	PCE (%)	Series resisitance(Ω)	Shut Resistance(Ω)
BiI_3-1	0.17	0.41	0.39	0.027	6454.18	34901.79

BiI_3-2	0.34	0.35	0.35	0.041	3892.95	15257.20
BiI_3-3	0.24	0.44	0.42	0.045	3952.75	36938.30
$(BiI_3)_{0.9}(MBI)_{0.1}$-1	0.25	0.51	0.45	0.058	3974.87	43781.80
$(BiI_3)_{0.9}(MBI)_{0.1}$-2	0.22	0.46	0.45	0.047	4255.23	47002.94
$(BiI_3)_{0.9}(MBI)_{0.1}$-3	0.22	0.49	0.43	0.048	4609.54	41020.10
$(BiI_3)_{0.9}(MBI)_{0.1}$-4	0.19	0.49	0.42	0.039	5709.27	5709.27
$(BiI_3)_{0.8}(MBI)_{0.2}$-1	0.24	0.57	0.51	0.071	3335.20	70945.88
$(BiI_3)_{0.8}(MBI)_{0.2}$-2	0.23	0.55	0.42	0.053	5241.01	52315.55
$(BiI_3)_{0.8}(MBI)_{0.2}$-3	0.26	0.57	0.50	0.076	3074.57	56962.07
$(BiI_3)_{0.5}(MBI)_{0.5}$-1	0.20	0.26	0.39	0.035	2983.52	35790.42
$(BiI_3)_{0.5}(MBI)_{0.5}$-2	0.47	0.26	0.49	0.034	1658.91	34318.22
$(BiI_3)_{0.25}(MBI)_{0.75}$-1	0.12	0.37	0.3	0.013	9428.7	18776.96
$(BiI_3)_{0.25}(MBI)_{0.75}$-2	0.1	0.36	0.27	0.009	12994.67	17504
$(BiI_3)_{0.25}(MBI)_{0.75}$-3	0.12	0.38	0.26	0.012	12331.8	14643.7
$(BiI_3)_{0.25}(MBI)_{0.75}$-4	0.11	0.32	0.26	0.009	11270	13645.4
MBI-1	0.13	0.46	0.39	0.023	1092.87	56841.57
MBI-2	0.13	0.44	0.37	0.021	1090.58	41871.72